Modelling Silver Thin Film Growth on Zinc Oxide

by

Adam L. Lloyd

A Doctoral Thesis
Submitted in partial fulfilment of the requirements for the award of
Doctor of Philosophy at Loughborough University

May 2, 2017

Abstract

Ag thin film growth on ZnO substrates has been investigated theoretically using multi-timescale simulation methods. The models are based on an atomistic approach where the interactions between atoms are treated classically using a mixture of fixed and variable charge potential energy functions. After some preliminary tests it was found that existing fixed charge potential functions were unreliable for surface growth simulations. This resulted in the development of a ReaxFF variable charge potential fitted to Ag/ZnO surface interactions. *Ab initio* models of simple crystal structures and surface configurations were used for potential fitting and testing.

The dynamic interaction of the Ag atoms with the ZnO surface was first investigated using single point depositions, via molecular dynamics, whereby the Ag impacted various points on an irreducible symmetry zone of the ZnO surface at a range of energies. This enabled the determination of the relative numbers of atoms that could penetrate, reflect or bond to the surface as a function of incident energy. The results showed that at an energy of up to 10 eV, most atoms deposited adsorbed on top of the surface layer.

The second part of the dynamic interaction involved a multi-timescale technique whereby molecular dynamics (MD) was used in the initial stages followed by an adaptive kinetic Monte Carlo (AKMC) approach to model the diffusion over the surface between impacts. An impact energy of 3 eV was chosen for this investigation. Ag was grown on various ZnO surfaces including perfect polar, O-deficient and surfaces with step edges. Initial growth suggests that Ag prefers to be spread out across a perfect surface until large clusters are forced to form. After further first layer growth, subsequent Ag atoms begin to deposit on the existing Ag clusters and are unlikely to join the first layer. Ag island formation (as mentioned within the literature) can then occur via this growth mechanism. O-deficient regions of ZnO surfaces result in unfavourable Ag adsorption sites and cause cluster formation to occur away from O-vacancies. In contrast, ZnO step edges attract deposited Ag atoms and result in the migration of surface

Ag atoms to under-coordinated O atoms in the step edge.

Various improvements have been made to the existing methodology in which transitions are determined. A new method for determining defects within a system, by considering the coordination number of atoms, is shown to increase the number of transitions found during single ended search methods such as the relaxation and translation (RAT) algorithm. A "super-basin" approach based on the mean rate method is also introduced as a method of accelerating a simulation when small energy barriers dominate. This method effectively combines states connected by small energy barriers into a single large basin and calculates the mean time to escape such basin.

To accelerate growth simulations further and allow larger systems to be considered, a lattice based adaptive kinetic Monte Carlo (LatAKMC) method is developed. As off-lattice AKMC and MD results suggest Ag resides in highly symmetric adsorption sites and that low energy deposition events lead to no penetrating Ag atoms or surface deformation, the on-lattice based approach is used to grow Ag on larger perfect polar ZnO surfaces. Results from the LatAKMC approach agree with off-lattice AKMC findings and predict Ag island formation.

Critical island sizes of Ag on ZnO are also approximated using a mean rate approach. Single Ag atoms are placed above an existing Ag cluster and all transition states are treated as belonging to a single large "super-basin". Results indicate that small Ag clusters on the perfect ZnO surface grow in the surface plane until a critical island size of around 500 atoms is reached. Once a critical island size is reached, multiple Ag ad-atoms will deposit on the island before existing Ag atoms join the cluster layer and hence islands will grow upwards. A marked difference is seen for second layer critical island sizes; second layer Ag islands are predicted to be two orders of magnitude smaller (< 7 atoms). This analysis suggests that Ag on ZnO $(000\bar{1})$ may exhibit Stranski-Krastanov (layer plus island) growth.

Acknowledgements

Firstly, I would like to thank Loughborough University and HPC Midlands for all the resources and computing facilities I have used throughout this research project. I also appreciate the support given from EPRSC and AGC Europe for funding this work. I would particularly like to thank my supervisors Professor Roger Smith and Professor Steven Kenny for their invaluable support and guidance throughout the project. I would also like to express my gratitude to my colleagues, past and present, in the materials modelling group for their contribution in developing and maintaining the LBOMD and LAKMC software packages used at Loughborough. A special thank you goes to Chris Scott, Tomas Lazauskas, Miao Yu and Mark Wootton for helping me settle into my research role and their continued support throughout my time working towards a PhD.

Thanks are also given to collaborators David Cornil, Jerome Cornil and David Beljonee at the University of Mons for useful discussions and work regarding DFT calculations for surface structures. Also to Adri van Duin and Diana van Duin at Penn. State University for their help fitting the new ReaxFF type potential. Many useful discussions were also had with Benoit Lecomte, Wiame Hugues and Mercier Virginie.

Contents

List of Figures

List of Tables

Chapter 1

Introduction and Background

1.1 Low-E Window Coatings

Optical coatings are often applied to glass to help block, filter or reflect certain wavelengths of the electromagnetic spectrum [1]. Other coatings can also be applied to obtain various properties such as self cleaning, antireflective or scratch resistant coatings. Low-Emissivity (Low-E) coatings are used to prevent heat loss (or gain) through windows via reflection. These coatings are designed to keep heat inside (or outside) a building. Ideal Low-E windows have to transmit visible light and reflect selected wavelengths of infra red light whilst maintaining a neutral appearance.

Low-E coatings are made by applying several layers of materials onto a glass substrate. The principle structure of a Low-E coating is a reflective (usually silver) layer sandwiched between two dielectric layers [2] (Fig. 1.1). Other materials may be applied to improve appearance or growth (seeding layer), along with tough protecting layers. A seeding layer is often used to encourage improved silver growth. This seeding layer is usually ZnO or TiO_2 based. This interface however is known as one the weakest in the multilayer. This is assumed to be due to low adhesion and lattice mismatch.

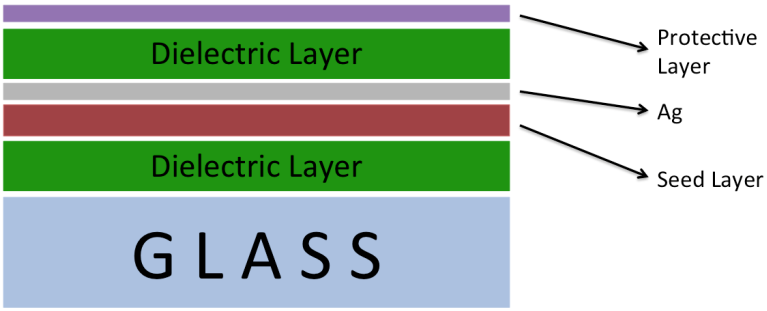

Figure 1.1 – A diagram showing the principle structure of a Low-Emissivity coating on glass. A silver thin film applied to a seeding layer and sandwiched between two dielectric layers. This is applied to a glass substrate. A tough outer coating is also often applied for protection.

Silver is the material of choice in Low-E coatings due to being one of the best optical reflectors (beaten only by aluminium in the visual light spectrum) [3]. Even though silver is a relatively expensive material, it has the highest electrical and thermal conductivity of all metals and, due to these properties, it is often used ahead of aluminium in Low-E window production. This thesis solely considers the growth and performance of silver on an existing substrate.

1.2 Ag/ZnO Interface

Energy efficient windows are made by applying several thin layers of different materials (usually by magnetron sputtering or evaporation techniques) onto a glass substrate. The reflective Ag and ZnO layers are the most important components in producing energy efficiency in these windows. The structure of the Ag and ZnO layers, along with the interface, are key for producing maximum efficiency. This investigation considers a coating of Ag(111) on top of an oxygen-terminated polar ZnO($000\bar{1}$) substrate. This arrangement produces a lattice mismatch between the ZnO layer and the Ag of around +11% [4]. ZnO has two common crystal forms: wurtzite and zincblende (Fig. 1.2) [5]. For this work, only the more stable wurtzite crystal structure is considered.

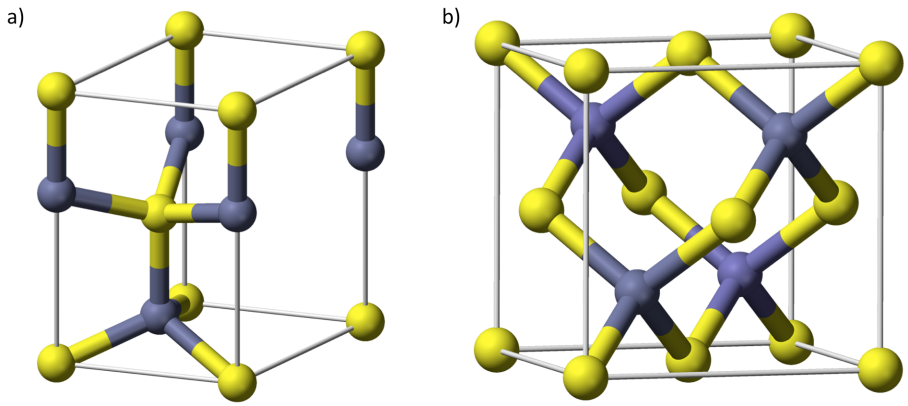

Figure 1.2 – Schematic diagram of the two main ZnO crystal structures: a) - the wurtzite structure and b) - the zincblende (sphalerite) structure. Images taken from [6].

There are two different oxygen-terminations of ZnO in the wurtzite form; the one used for the majority of this research is the lower interface which terminates with oxygen atoms that have three first neighbour zinc atoms. The upper (less energetically favourable) interface terminates in dangling oxygen atoms with only one first neighbour zinc atom. The most stable form of bulk Ag is the face-centred cubic (FCC) crystal structure. Fig. 1.3 shows an example interface between an Ag monolayer (ML) and a ZnO substrate in the O-terminated wurtzite form.

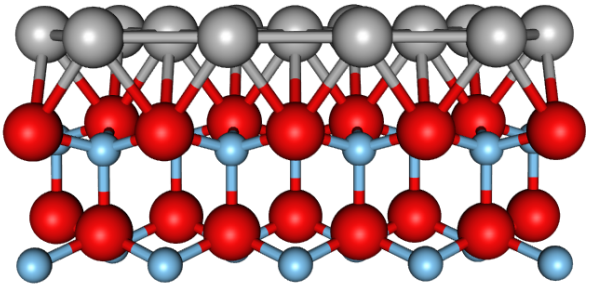

Figure 1.3 – Schematic diagram showing the lower interface between Ag (111) and ZnO $(000\bar{1})$. In all diagrams (unless otherwise stated) the large silver spheres represent silver atoms, the large red spheres represent oxygen atoms whilst the smaller blue spheres represent zinc atoms.

Throughout this work, the stacking positions of Ag on the polar ZnO are used whilst analysing growth results. For Ag on the polar ZnO surface, there are 3 principle, highly symmetric stacking sites that Ag ad-atoms have a tendency to reside in (Fig. 1.4). The notation used to

describe the stacking of atoms are capital letters for the ZnO substrate and lower case for Ag atoms. The 3 stacking sites considered in the work are:

- **ABa** - "**A**" denotes the position of Zn atoms, "**B**" the position of the O atoms and the Ag atom directly above an "**A**" stacked Zn atom is labeled as "**a**".
- **ABb** - The same ZnO positions as above but the Ag atom instead resides directly above a surface, "**B**" stacked, O atom and this is labelled as a "**b**" stacking site.
- **ABc** - The same ZnO positions as above but the Ag atom instead resides in a symmetric hollow site between surface O and Zn atoms. This is labelled as a "**c**" stacking site.

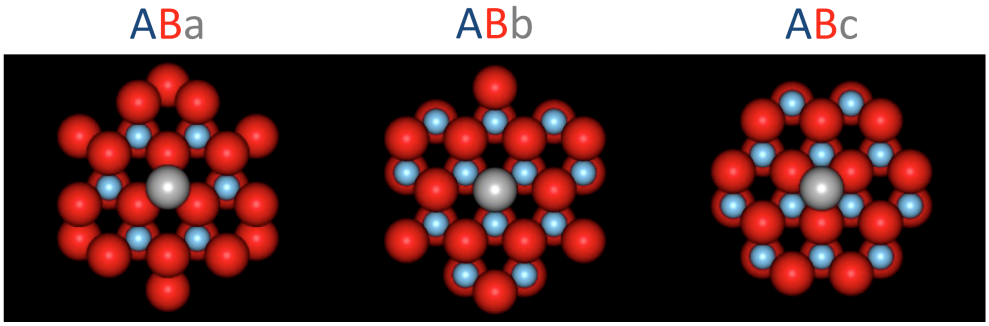

Figure 1.4 – Schematic diagram showing the three principle stacking sites of Ag ad-atoms on polar $(000\bar{1})$ ZnO surfaces.

Investigations have been made into improving the lattice mismatch and adhesion at the interface by introducing hydrogen at the surface and using an aluminium-doped ZnO (AZO) substrate. However, Lin and Bristowe [7] show that although the lattice mismatch may be reduced in some cases, AZO and ZnO with added H atoms at the surface dramatically reduce the work of separation at the Ag interface.

1.3 Deposition Methods

There are many techniques for the deposition of thin films [8]. These techniques can be split into two main classes: liquid phase deposition and vapour phase deposition. The liquid phase strand

can be split into two main categories also: chemical solution deposition or electro-chemical deposition methods. In the vapour phase strand, another two categories emerge: either physical vapour deposition (PVD) or chemical vapour deposition (CVD). The method that is modelled within this report is a PVD method and is known as magnetron sputtering [9].

Sputtering is extensively used in industry to deposit various thin films. It uses low substrate temperatures and is ideal for depositing contact metals. Atoms are sputtered from a target by argon ions and then flow through a plasma towards a substrate (Fig. 1.5). For the coating process to work, a low vacuum must be employed. This then allows a controlled flow of argon or other inert gas to be introduced. Sometimes oxygen or nitrogen are introduced into the system to fabricate oxide or nitride films: this is know as reactive sputtering. Magnets are positioned behind the target creating a magnetic field whilst high voltage is applied to the target to ionise the argon gas. This forms a plasma along the electrical field and argon atoms within the plasma become positively charged. These argon ions subsequently impact the negatively charged target causing sputtering of the target material. These sputtered atoms can then accelerate towards a substrate if a bias voltage is applied. Typical deposition energies for sputtered silver atoms are a few eV (1 to 20 eV) at a rate of 5 to 40 monolayers per second (ml/s) [10].

1.4 Simulation Techniques

Modelling the behaviour of materials via computer simulation has gained popularity within the last half a century due to the vast increase in computing power and the development of more advanced techniques. These techniques span across a wide range of time and length scales (Fig.1.6). The simulation technique used depends on the system that is modelled.

Ab initio (meaning "from the beginning") [11] techniques come from first principles quantum mechanics and are used to investigate the electronic structure in many-body system. Density

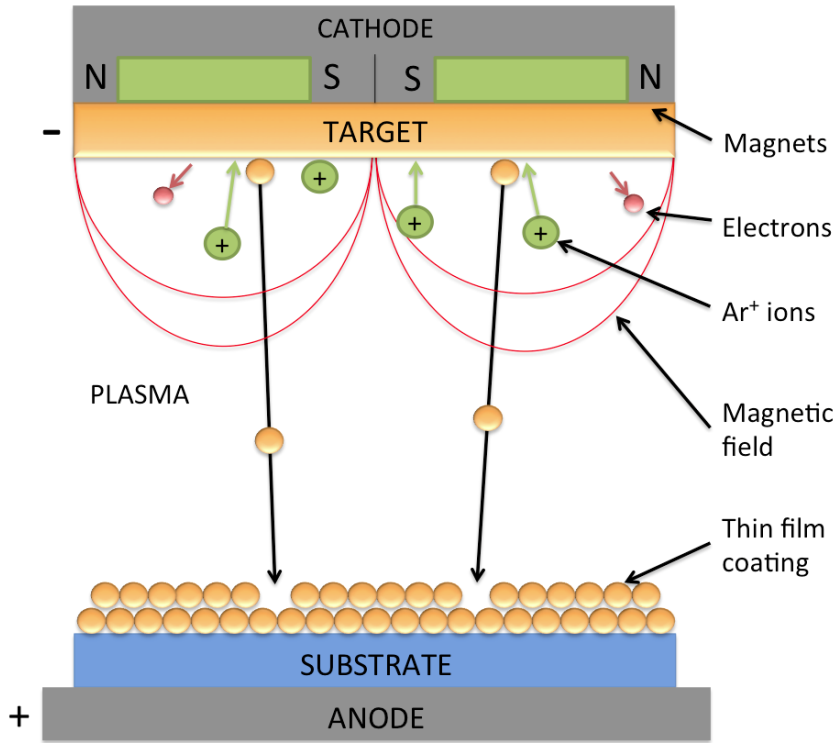

Figure 1.5 – Diagram showing the magnetron sputtering process. The device is situated within a vacuum chamber. A DC, pulsed DC, AC or RF power supply is applied depending on the target material. Positive argon ions bombard the target material and sputtered atoms head towards the substrate creating a thin film coating.

functional theory (DFT) is usually the *ab initio* method of choice due to its ability to accurately reproduce experimental data for many systems. One of the many uses for DFT simulation is for the parametrisation of interatomic potentials for use within MD simulations. In this thesis, DFT is used to model simple surfaces and crystal structures for the fitting of a many-body ReaxFF potential [12].

Molecular Dynamics (MD) methods are based on interatomic potential functions. From these functions, MD simulates the trajectories of atoms by solving Newton's equations of motion for a given system. The time increment between steps is usually of the order of 1 femtosecond to include even the highest frequency of molecular vibration. Due to this, MD is commonly used to simulate deposition or collision events [13, 14, 15]. MD is used here to simulate deposition events of Ag atoms on ZnO surfaces.

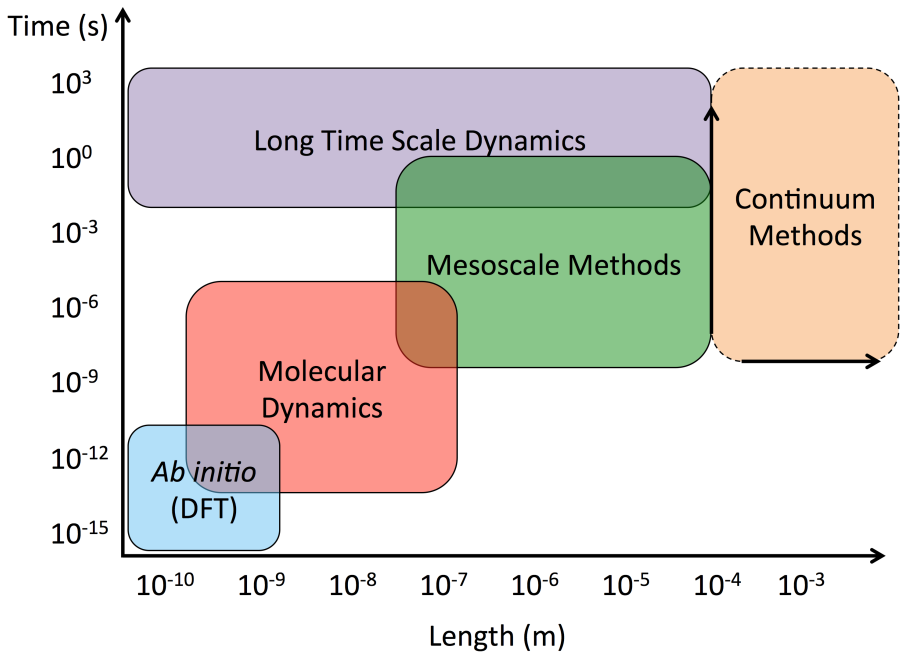

Figure 1.6 – An insight into how different simulation methods compare to each other in regards to length and time scales. Notice that many methods actually overlap in this diagram.

Mesoscale methods consider larger molecules or collections of atoms as single point particles instead of each individual atom in MD. These methods are popular for simulating large clusters of atoms and polymers [16] and so are not considered in this work.

Methods that access longer time scale than those accessible by MD include: temperature accelerated dynamics (TAD)[17], parallel replica dynamics (PRD) [18], kinetic Monte Carlo (KMC)[19] and Adaptive KMC [20]. Whilst TAD and PRD can efficiently accelerate MD simulations, they can be less efficient than AKMC methods for many systems. AKMC methods have been shown to simulate systems of several hundred atoms for millisecond-second timescales [21]. Because of this, AKMC based methods are used in thesis and are further discussed in chapter 3.

1.5 Previous Work

The interaction between Ag and ZnO surfaces has been investigated experimentally by Duriau *et. al.* [22], where ZnO $(000\bar{1})$ substrates were grown using plasma enhanced molecular beam epitaxy (MBE) and annealed at 973 K. Ag was then deposited using low energy evaporation techniques at a slow rate of 8×10^{-4} nm/s. Scanning tunneling microscopy (STM) was then used to analyse the growth patterns. Results suggest that a high density of islands form at early stages of growth and 30% of the ZnO surface is left uncovered throughout Ag growth (Fig. 1.7).

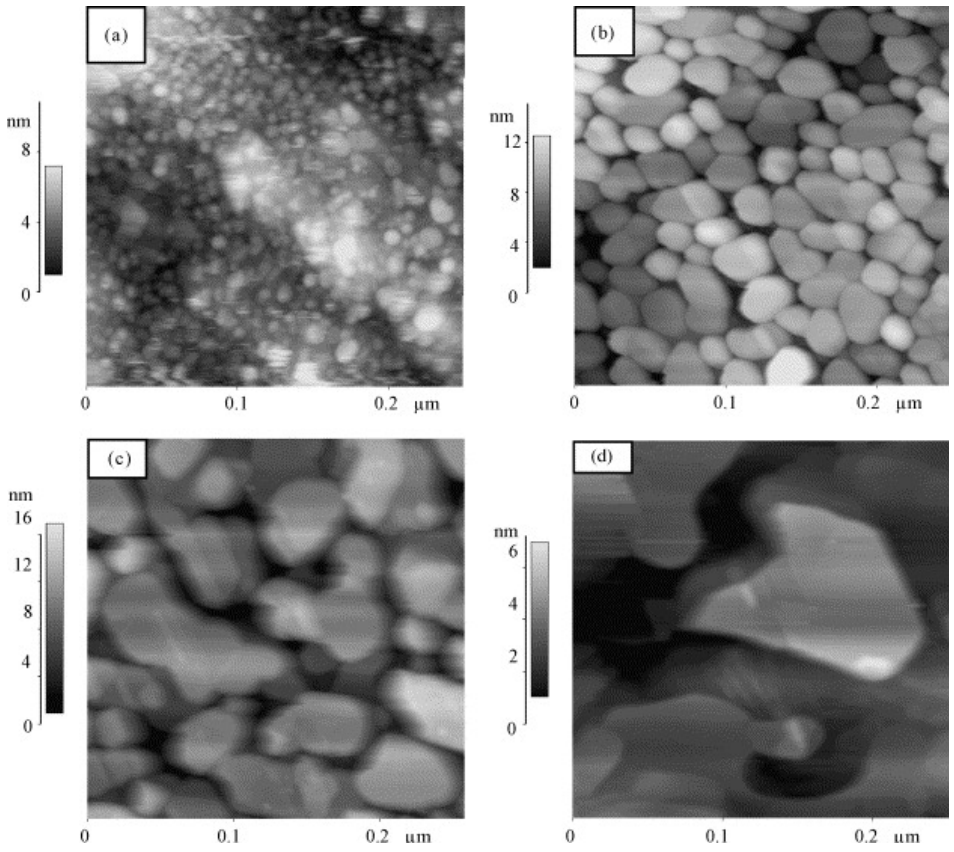

Figure 1.7 – STM images of Ag on ZnO$(000\bar{1})$ at various stages of growth: (a) - 8ML, (b) - 16ML, (c) - 32ML and (d) 64ML. Image taken from [22]

Lin and Bristowe [4] also considered a system of Ag and ZnO using *ab initio* methods. Their work investigated the effect of different lattice matched Ag(111)/ZnO(0001) interfaces and a selection of pyramidal Ag clusters on ZnO(0001). Three different sized Ag clusters were

examined in flat monolayer (ML) and pyramidal structures. For all cases, Ag in pyramidal structures on the ZnO surface were energetically more favourable configurations. Other results from this work suggest that Ag bonds more strongly onto the oxygen terminated ZnO interface.

Both studies indicate that Ag initially grows in islands on ZnO surfaces. However both the fundamental experimental and *ab initio* methods may not model exact real systems. With the experimental work, the roughness of the ZnO surfaces is known but specific surface defects are not. The large amounts of uncovered surface may be influenced by certain ZnO surface defects. The *ab initio* investigations generally only consider small and perfect ZnO surfaces. In chapter 6, larger surfaces than those typically used in DFT and various surface defects are considered using MD and KMC methods.

Research into the growth of various thin films have been conducted using MD and AKMC methods by Blackwell [21, 15, 23] and Yu [13, 24]. The work of Blackwell concentrates on the growth of Ag on Ag, ZnO on ZnO and TiO_2 on existing TiO_2 substrates. A similar growth methodology is used here when initial growth of Ag on ZnO surfaces is investigated. Previous work [21] has indicated that after annealing, O atoms can move and restructure the ZnO surface such that phase boundaries can appear (Fig. 1.8). Growth on this type of structure and structures including step edges and single O-vacancies is considered in chapter 6.

1.6 Research Aims

The modelling of atomic processes has become increasingly useful in many industries. By investigating simulations instead of experimenting on the real components, research costs and time can be reduced. Simulation allows the possibility to change many different parameters that may not be so easily varied in experiments. Window coatings are a good example of where modelling can help improve certain properties. Atomic scale observations are not

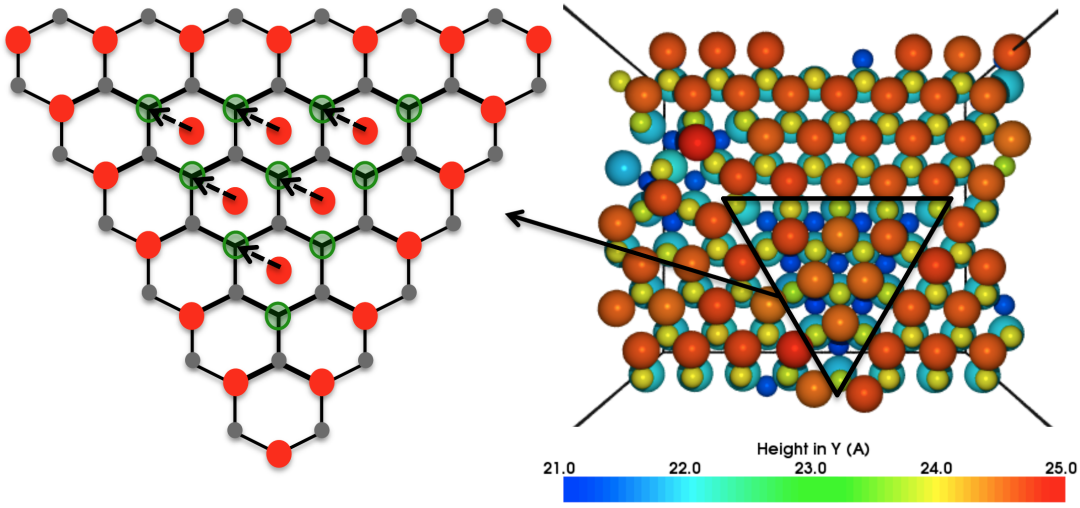

Figure 1.8 – Example configuration of a ZnO surface after annealing at 920 K. Within the triangular region on the wurtzite structure, a zinc blende phase appears when O vacancies (green circles) occur during growth. Arrows indicate where O atoms would be if there was no reordering of the surface to a zinc blende structure. Image taken from [21].

usually feasible for this industry and so simulation processes are often used to determine the characteristics of different interfaces and how materials grow on each other.

The overall aim of this project is to analyse atomic scale processes with the intention of improving the quality of the Ag layer in Low-E window coatings. By simulating the magnetron sputtering growth process of silver, we can see if adjusting certain parameters can affect the quality of the thin film. Key improvements would be in optical performance, structure of the Ag thin film and the adhesion to a substrate leading to a reduced quantity of silver needed and consequently a lower cost of production.

1.7 Thesis Layout

Chapters 2 and 3 discuss some of the main ideas and methodology used. Chapter 2 gives an overview of molecular dynamics (MD) simulation techniques and introduces several types of

potential functions used for modelling the Ag/Zn/O system including the simple pair potentials and many-body ReaxFF type potentials. Chapter 3 concentrates on theory behind kinetic Monte Carlo simulation methods and the implementation of the code used to model initial growth phases. Single and double ended search algorithms are introduced as well as methods to increase efficiency.

The next four chapters examine the results of Ag growth on ZnO via various simulation techniques. Chapter 4 examines an existing model, fitted to works of separation, for Ag/Zn/O interactions. Single point deposition of Ag on ZnO results and initial growth phases are investigated via MD and KMC. Chapter 5 explains the development of an improved potential to model growth. In this chapter, DFT calculations are used to fit a new ReaxFF potential which is then compared against experimental, *ab initio* and other models. The two subsequent chapters discuss growth results using the newly developed potential introduced in chapter 5. In chapter 6 we use off-lattice adaptive KMC (AKMC) to model Ag growth on various ZnO surfaces, including oxygen deficient surfaces and surfaces with step edges, and in chapter 7 a lattice based AKMC (LatAKMC) method is introduced. The methodology behind LatAKMC is described along with multiple layer growth results for Ag on ZnO and critical island size analysis. Chapter 8 then concludes this research and results found as well as mentioning possible directions for future work on this topic.

Chapter 2

Methods I: Molecular Dynamics

One popular method of modelling the interaction of atoms is Molecular Dynamics (MD). This technique is particularly useful for simulating the dynamics of a system containing large numbers of atoms. In classical MD, atoms are modelled by point particles, with the interactions between the different particles defined by an interatomic potential energy function, V. These functions can come in a variety of forms including 2, 3 and many body potentials. The subsequent force function, $\mathbf{F}_i$, on each atom, i, is then given by the negative gradient of the potential:

$$-\nabla_{\mathbf{r}_i} V(\mathbf{r}_1, \mathbf{r}_2, ..., \mathbf{r}_N) = \mathbf{F}_i, \tag{2.1}$$

where $\mathbf{r}_i$ represents the atomic positions. By using Newton's equation of motion, we can then obtain a relation between the force and acceleration

$$\mathbf{F}_i = m_i \mathbf{a}_i = m_i \frac{d^2 \mathbf{r}_i}{dt^2} \tag{2.2}$$

for each atom i. Here $m_i, \mathbf{a}_i$ and t represent the mass and acceleration of atom i and time respectively. Integration of Newton's second law gives a trajectory. From the trajectory, the position, velocity and acceleration of particles can be found at various times in a simulation. The standard procedure for a classical MD simulation is as follows:

- **Step 1** - Set initial atom positions $\mathbf{r}^{(0)}$, $t = 0$ and choose small Δt
- **Step 2** - Calculate forces, $\mathbf{F}^{(t)} = -\nabla_{\mathbf{r}} V(\mathbf{r}^{(t)})$, and find $\mathbf{a}^{(t)} = \mathbf{F}^{(t)}/m$
- **Step 3** - Find new atom positions: $\mathbf{r}^{(t+\Delta t)}$
- **Step 4** - Increase time, $t = t + \Delta t$, and return to step 2.

2.1 Time Integration

To evolve the system in time, the Loughborough MD package (LBOMD) [25] uses a velocity Verlet algorithm [26]. The trajectory is advanced by a fixed time step Δt and the position, $\mathbf{r}$, and velocity, $\mathbf{v}$, of each atom, i, is estimated by a combination of Newton's second law of motion and Taylor expansions. The displacement, velocity and acceleration functions can be approximated by:

$$\begin{aligned} \mathbf{r}_i^{(t+\Delta t)} &\approx \mathbf{r}_i^{(t)} + \mathbf{v}_i^{(t)}\Delta t + \tfrac{1}{2}\mathbf{a}_i^{(t)}\Delta t^2, \\ \mathbf{v}_i^{(t+\Delta t)} &\approx \mathbf{v}_i^{(t)} + \mathbf{a}_i^{(t)}\Delta t + \tfrac{1}{2}\dot{\mathbf{a}}_i^{(t)}\Delta t^2, \\ \mathbf{a}_i^{(t+\Delta t)} &\approx \mathbf{a}_i^{(t)} + \dot{\mathbf{a}}_i^{(t)}\Delta t. \end{aligned} \tag{2.3}$$

By rearranging the approximation for $\mathbf{a}_i^{(t+\Delta t)}$ and substituting this into the equation for $\mathbf{v}_i^{(t+\Delta t)}$ we obtain:

$$\mathbf{v}_i^{(t+\Delta t)} \approx \mathbf{v}_i^{(t)} + \frac{\mathbf{a}_i^{(t+\Delta t)} + \mathbf{a}_i^{(t)}}{2}\Delta t. \tag{2.4}$$

Using Newton's second law of motion, we then derive the time integration equations (Eq. 2.5 and 2.6):

$$\mathbf{r}_i^{(t+\Delta t)} = \mathbf{r}_i^{(t)} + \mathbf{v}_i^{(t)}\Delta t + \frac{\mathbf{F}_i^{(t)}\Delta t^2}{2m_i}. \tag{2.5}$$

Once the forces are updated with the new positions, the velocity can then be updated:

$$\mathbf{v}_i^{(t+\Delta t)} = \mathbf{v}_i^{(t)} + \frac{\mathbf{F}_i^{(t)} + \mathbf{F}_i^{(t+\Delta t)}}{2m_i}\Delta t. \tag{2.6}$$

Despite the advances in computer power, a typical MD simulation can only describe a system over picosecond to nanosecond timescales. However, this depends on the number of atoms simulated and the interatomic potential used. For example, many-body potential functions are far more computationally expensive than simple pair potentials. MD is ideal for simulating short time scale events and accurately modelling the dynamics of such an event. Because of the time scale limitation of MD however, by itself it is unfeasible to simulate full multilayer growth. In this work MD, is used in conjunction with a long time scale simulation technique.

2.2 Interatomic Potential Functions

There are many formulae for estimating interatomic potentials, each with varying complexity. The simplest forms are two-body functions which depend on the distance from one atom to another. In this case, the total potential energy in a system is simply the sum of all the pair interactions. Thus, the total energy of a system is then described as

$$V_{system} = \frac{1}{2}\sum_{i}\sum_{j\neq i} V_{ij}. \tag{2.7}$$

However, in many cases, a simple pair potential is not adequate at modelling the system. This is where more complicated many-body potentials, for example a bond order potential, are used.

2.2.1 Morse Potential

The Morse Potential [27] is a two-body function which in its modified form is:

$$V_{ij} = \frac{D_0}{S-1}\left(e^{-\beta\sqrt{2S}(r_{ij}-r_0)} - Se^{-\beta\sqrt{2/S}(r_{ij}-r_0)}\right). \tag{2.8}$$

Here, the dimer bond energy, D_0, dimer bond distance, r_{ij}, and the free parameter, β, are fitted to bulk properties of the material. S can be used as an extra parameter when fitting to material properties but is given as 2 in the original, unmodified, Morse potential. The Morse

Table 2.1 – Morse potential parameters for Ag-O interaction on the ZnO($000\bar{1}$) surface.

Parameter	Value
D_0 (eV)	0.333
r_0 (Å)	2.590
S	1.057
β	1.618

potential is a simple pair potential and with only 4 parameters and is relatively simple to fit to specific data. Gheewala [28] fitted the Morse potential to Ag-O works of separation of Ag from ZnO for his work on nano-indentation. This model is used in chapter 4 for Ag-O surface interactions. The parameters used are included in Table 2.1.

2.2.2 Ziegler-Biersack-Littmark Potential

The Ziegler-Biersack-Littmark (ZBL) potential [29] is another pairwise potential, a screened Coulomb interaction, that is used mainly for simulating the short range repulsion that occurs when the distance between two atoms is small. At these distances, there is a strong repulsive force between atomic nuclei. This potential therefore is purely repulsive. The potential is given by:

$$V_{ij} = \frac{1}{4\pi\epsilon_0}\frac{Z_i Z_j}{r_{ij}}\phi(x). \tag{2.9}$$

with $\phi(x) < 1$ when $r > 0$ (purely repulsive). The charge of the nuclei of atoms i and j are given by Z_i and Z_j, r_{ij} is the atomic distance and ϵ_0 is the electrical permittivity of free space. Here

$$\phi(x) = 0.1818e^{-3.2x} + 0.5099e^{-0.9423x} + 0.2802e^{-0.4029x} + 0.02817e^{-0.2016x}, \tag{2.10}$$

is a general screening function and $x = r_{ij}/a_u$. Where,

$$a_u = \frac{0.8854a_0}{Z_i^{0.23} + Z_j^{0.23}}, \tag{2.11}$$

with $a_0 = 0.529$Å, the Bohr radius. The ZBL potential is used to model the interaction between Ag and Zn when Ag is deposited on the ZnO $(000\bar{1})$ surface in chapter 4. The Morse potential for Ag-O interaction was fitted along side the purely repulsive Ag-Zn potential to accurately reproduce works of separation at the surface interface.

2.2.3 Embedded Atom Method

If a wide range of material properties are to be reproduced accurately then a simple pair potential becomes inadequate. The embedded atom method (EAM) defines the potential energy function as the sum of a pair potential and an embedding term. It is generally used to describe the behaviour of metals. The energy of an atom i and the whole system are given by Eq. 2.12 and Eq. 2.13 respectively.

$$V_i = \frac{1}{2}\sum_{j\neq i} V_{ij} - f(\rho_i). \tag{2.12}$$

$$V_{system} = \sum_i V_i. \tag{2.13}$$

Here V_{ij} is the pair potential and $f(\rho_i)$ is the embedding function. ρ_i is given by

$$\rho_i = \sum_j \phi(r_{ij}), \tag{2.14}$$

where $\phi(r_{ij})$ is another pair potential. The Ackland potential [30] is a form of an EAM which has been developed to model noble metals, e.g. silver. It uses the pair potential and embedding functions below

$$V_{ij} = \sum_{k=1}^{6} a_k(r_k - r_{ij})^3 H(r_k - r_{ij}), \tag{2.15}$$

$$f(\rho_i) = \sqrt{\rho_i} - c_2\rho_i^2 - c_4\rho_i^4, \tag{2.16}$$

$$\phi(r_{ij}) = \sum_{k=1}^{2} A_k(R_k - r_{ij})^3 H(R_k - r_{ij}). \tag{2.17}$$

Table 2.2 – Values for a_k and r_k parameters in the Ackland potential for Ag-Ag interaction.

k	1	2	3	4	5	6
a_k (eV/Å^{-3})	20.368404	-102.36075	94.31277	-6.220051	31.080887	175.56047
r_k (Å)	1.2247449	1.1547054	1.1180065	1.000000	0.8660254	0.7071068

Table 2.3 – Values for A_k and R_k parameters in the Ackland potential for Ag-Ag interaction.

k	1	2
A_k (eV/Å^{-3})	1.4587610	42.946555
R_k (Å)	1.2247449	1.0000000

The function H is the Heaviside step function. The parameters r_k and R_k are fitted to the pair potential and the electron density term respectively. A_k and a_k are fitted to the lattice parameters, cohesive energy, elastic constants, vacancy formation energy, stacking fault energy and pressure-volume relationship. The Ackland EAM potential is used to model Ag-Ag interactions in chapter 4. The potential parameters for Ag-Ag interactions are given in Tables 2.2 and 2.3.

2.2.4 Reactive Force Field Potential

The Reactive Force Field (ReaxFF) potential, developed by van Duin *et al.* [31], depends on the bond order of atoms in a system. This potential has proven to be highly transferable, with an ability to describe both covalent, ceramic and metallic materials and their interfaces. The total energy of the system is expressed as a sum of bond order dependent and non-bonded energy terms:

$$\begin{aligned} E_{system} = \quad & E_{bond} + E_{vdWaals} + E_{Coulomb} + E_{val} + E_{lp} \\ & + E_{tors} + E_{pen} + E_{conj} + E_{over} + E_{under}. \end{aligned} \tag{2.18}$$

E_{bond} represents the bond energy between atoms i and j. The potential can also take into account the valence angle terms (E_{val}), torsion angles (E_{tors}), energy contributions associated with lone pairs, (E_{lp}), under and over coordination (E_{under} and E_{over}), additional energy penalties (E_{pen}) and possibly terms are included to account for conjugation effects. All these

terms depend on bond order which in turn is determined via interatomic distances from the equation:

$$BO'_{ij} = BO^{\sigma}_{ij} + BO^{\pi}_{ij} + BO^{\pi\pi}_{ij}, \tag{2.19}$$

where there are distinct differences between contributions from σ, π and double π bonds,

$$\begin{aligned} BO^{\sigma}_{ij} &= \exp\left[P_{bo1}\left(\frac{r_{ij}}{r^{\sigma}_{o}}\right)^{P_{bo2}}\right], \\ BO^{\pi}_{ij} &= \exp\left[P_{bo3}\left(\frac{r_{ij}}{r^{\pi}_{o}}\right)^{P_{bo4}}\right], \\ BO^{\pi\pi}_{ij} &= \exp\left[P_{bo5}\left(\frac{r_{ij}}{r^{\pi\pi}_{o}}\right)^{P_{bo6}}\right]. \end{aligned} \tag{2.20}$$

Here BO_{ij} and r_{ij} represent the bond order and the interatomic distance between the ith and jth atom respectively. The r_o terms correspond to equilibrium bond lengths and P_{bo} terms are fitted bond parameters.

The van der Waals and Coulomb ($E_{vdWaals}$ and $E_{Coulomb}$) terms are included for all pairs of atoms and are independent of bond order. The Coulomb interaction is modelled by a shielded Coulomb potential where atomic charges are calculated via the Electronegativity Equalization Method (EEM) [32].

For most systems, when creating a new parameter set for a ReaxFF potential, not all terms in Eq. 2.18 are deemed necessary. Keeping the number of terms down to a minimum, whilst maintaining a reasonable model, can decrease the computational time needed to run reliable simulations. For the parameter sets describing Zn/O [33] interactions and the full Ag/Zn/O system [12], many terms were set to zero yielding the reduced energy expression:

$$E_{system} = E_{bond} + E_{vdWaals} + E_{Coulomb} + E_{val} + E_{lp} + E_{over} + E_{under}. \tag{2.21}$$

2.3 Optimising Potentials

For many potential functions, the interaction between particles is well described near equilibria but less well described at short ranges. To optimise potential functions for specific systems, cut-off functions are implemented to reduce the long range interactions, neighbour lists are implemented to reduce the number of calculations and a mixture of pair potentials can be splined together for short range interactions to better describe the potential energy when the distance between particles becomes small.

2.3.1 Potential Cut-Offs and Neighbour Lists

If the pair-potential functions have an infinite range of interaction a cut-off function is implemented. Having an infinite range of interaction can cause problems since the number of calculations required grows like N^2 (where N is the number of particles in a system). Having a sensible cut-off in place, with the use of neighbour lists, reduces computation to an $\mathcal{O}(N)$ problem. A cosine function function is often used to smoothly take a potential function to zero between two points: r_{cut} and $r_{cut-off}$:

$$V_{cut-off}(r_{ij}) = \frac{1 + \cos(\pi \cdot C(r_{ij}))}{2} \cdot V_{Pot.}(r_{ij}), \tag{2.22}$$

where $V_{Pot.}$ represents the potential function used and $C(r_{ij})$ is a linear function that goes from 0 at r_{cut} and 1 at $r_{cut-off}$.

When using potential cut-off functions, neighbour lists are used. As potential energy decreases to zero for all long range interactions, calculating the potential energy between particles that are far apart is unnecessary. To reduce the number of calculations, a list of neighbours within the cut-off radius, $r_{cut-off}$, around a particle is considered. Verlet [26] then takes a larger sphere, of radius r_l, around the given particle such that no atom could travel through it within a single time step. All particles within the larger sphere are then included in the neighbour

lists and used to calculate potential energies. The neighbour list then remains the same until the magnitude of the largest displacement exceeds the skin is, $r_l - r_{cut-off}$.

The LBOMD code uses neighbour lists to speed up the simulation. Normally this is not suitable for Coulomb energy contributions in fixed charge models, however ReaxFF cuts off the Coulomb at 1 nm allowing neighbour lists to be used.

2.3.2 Spline Functions

As well as potential cut-offs, splining the potential function to a ZBL function is often used to better describe close range repulsion of atoms. This is particularly useful when considering high energy collision cascades. To ensure the potential function is continuous for its first and second derivatives, a sixth-order exponential function is used to spline between the potential function and a ZBL potential:

$$V_{Spline}(r_{ij}) = e^{C_0+C_1 r_{ij}+C_2 r_{ij}^2+C_3 r_{ij}^3+C_4 r_{ij}^4+C_5 r_{ij}^5}, \tag{2.23}$$

where C_0 to C_5 are spline coefficients obtained by solving a system of linear equations:

$$\begin{aligned}
C_0 + C_1 A + C_2 A^2 + C_3 A^3 + C_4 A^4 + C_5 A^5 &= \ln V_1(r_a) \\
C_0 + C_1 B + C_2 B^2 + C_3 B^3 + C_4 B^4 + C_5 B^5 &= \ln V_2(r_b) \\
C_1 + 2C_2 A + 3C_3 A^2 + 4C_4 A^3 + 5C_5 A^4 &= \tfrac{F_1(r_a)}{V_1(r_a)} \\
C_1 + 2C_2 B + 3C_3 B^2 + 4C_4 B^3 + 5C_5 B^4 &= \tfrac{F_2(r_b)}{V_1(r_b)} \\
2C_2 + 6C_3 A + 12C_4 A^2 + 20C_5 A^3 &= \tfrac{G_1(r_a)}{V_a(r_a)} - \left(\tfrac{F_1(r_a)}{V_1(r_a)}\right)^2 \\
2C_2 + 6C_3 B + 12C_4 B^2 + 20C_5 B^3 &= \tfrac{G_2(r_b)}{V_b(r_2)} - \left(\tfrac{F_2(r_b)}{V_2(r_b)}\right)^2 .
\end{aligned} \tag{2.24}$$

Here, r_a and r_b are the points where the splining function meets the potential functions V_1 and V_2 respectively. At these points, the splining function is also smooth and continuous for first (F_1 and F_2) and second derivatives (G_1 and G_2). The values for r_a and r_b are manually

chosen to ensure the functions are as smooth as possible. An example of a splining function for the simplified Morse model, whose parameters are given in Table 2.1, and a ZBL potentials is shown in Fig 2.1.

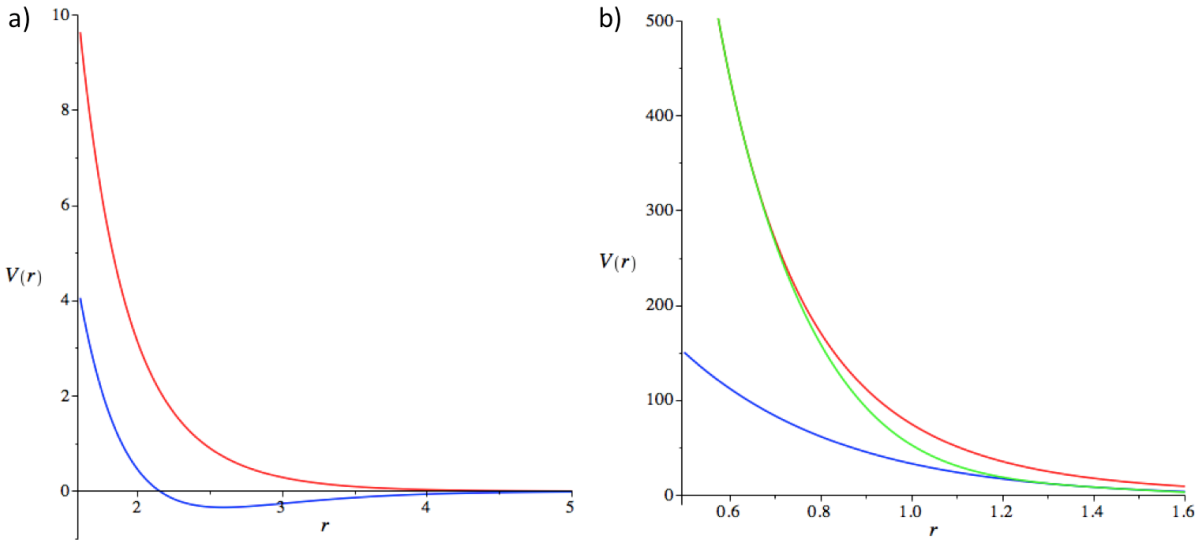

Figure 2.1 – Plots of potential functions for Ag-O interaction. Plot a) - shows the Morse (blue) and ZBL (red) potentials. Plot b) - shows the splining function (green) between the two potentials at r_a and r_b.

The typical form of a pair potential is then given by:

$$V(r_{ij}) = \begin{cases} V_{ZBL}(r_{ij}) & r_{ij} < r_a, \\ V_{Spline}(r_{ij}) & r_a \leq r_{ij} \leq r_b, \\ V_{Pot.}(r_{ij}) & r_b < r_{ij} < r_{cut}, \\ V_{Cut-off}(r_{ij}) & r_{cut} \leq r_{ij} \leq r_{cut-off}, \\ 0 & r_{ij} > r_{cut-off}. \end{cases} \tag{2.25}$$

For Ag-O and Ag-Zn interactions, the splining interval values used for cut-off and splining functions are given in Table 2.4. The coefficients for the splining functions are given in Table 2.5. For the Ag-Zn interaction in the first potential Ag-ZnO parameterisation, a ZBL pair potential is used. In this case, instead of splining at short range, the potential is splined directly to zero

Table 2.4 – Values for splining intervals for Ag-O and Ag-Zn interactions.

Interaction	r_a	r_b	r_{cut}	$r_{cut-off}$
Ag - O	0.6	1.4	6.0	6.2
Ag - Zn	0.6	1.4	-	-

Table 2.5 – Splining function coefficients for Ag-O interaction and Ag-Zn interaction

Interaction	C_0	C_1	C_2	C_3	C_4	C_5
Ag - O	18.4122	-59.5822	123.9420	-135.6367	71.0914	-14.2560
Ag - Zn	16.2893	-48.9340	99.6955	-108.9421	58.2591	-11.9266

at distances of 1.4 Å. This means that the purely repulsive potential comes into affect for short range interactions only.

For many body potential functions, such as ReaxFF and EAM, the van der Waals energy contribution or the repulsive pair potential part function is splined to a ZBL potential function at short ranges. However, for low energy deposition events, the splining and ZBL functions are rarely sampled. For the simulation of Ag growth on ZnO, typical deposition energies are around 3 eV which is less than the potential energy of the Ag-ZnO potential in the splining region.

2.4 Boundary Conditions

Fixed boundaries are applied by fixing the outer layer(s) of atoms in a system and can be used when simulating low energy impacts on a surface. When performing cumulative deposition simulations it is useful to fix the bottom layer of a lattice otherwise the substrate will drift downwards due to the conservation of momentum.

For many materials modelling techniques, the system modelled is a smaller system than the real material used in experiments, since computer simulations requires a finite system to be

modelled. This finite system region needs to behave as if it is part of a larger system and so must be surrounded by other atoms within the potential cut-off. To give the effect of simulating a much bigger system, periodic boundary conditions are used (Fig. 2.2).

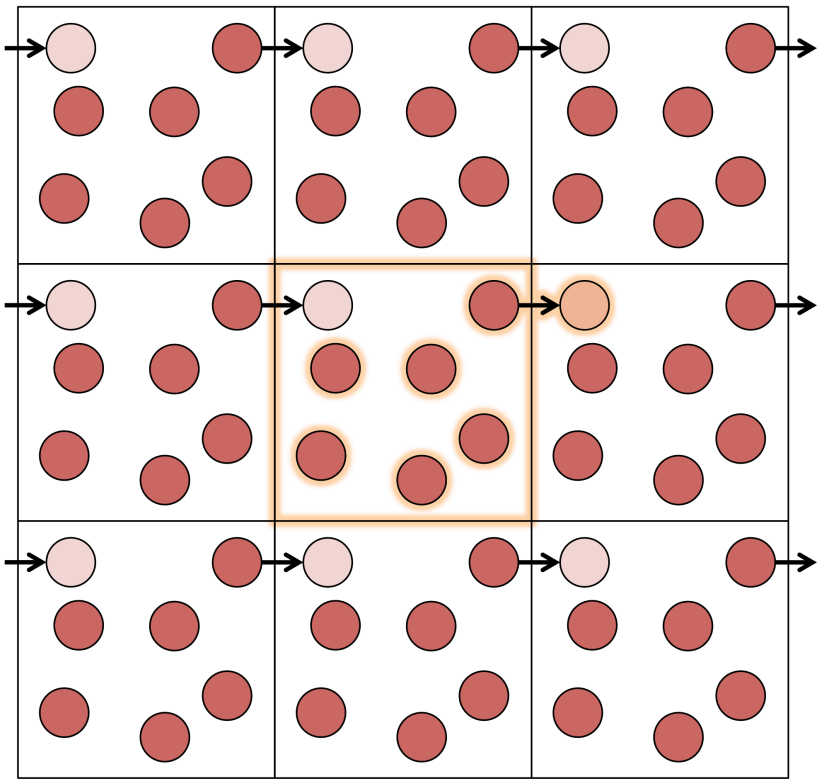

Figure 2.2 – A schematic of how periodic boundary conditions function on a 2D system. The centre cell contains the simulated system whilst the surrounding cells are used replicate the bulk system effect. If a particle exits the simulation cell in one direction, it will be inserted on the opposite side.

2.5 Finite Temperature Control

When running MD simulations, the temperature of the system is important. The kinetic energy in a system is controlled by the temperature of the heat bath. Temperature control is implemented into MD by initially heating the whole system to a chosen temperature; this means velocities of the atoms are scaled according to thermalisation algorithm that is employed.

Temperature is maintained by keeping some atoms connected to a thermal bath. Thermalisation algorithms used within the LBOMD package are the Berendsen thermostat [34] and the Nosé-Hoover thermostat [35].

Berendsen [34] describes a thermostat algorithm that controls the temperature of a system by scaling the velocity vector of thermal atoms at each time step. All the velocities are scaled by a factor λ defined by

$$\lambda = \left[1 + \frac{\Delta t}{\tau_T}\left(\frac{T_0}{T} - 1\right)\right]^{\frac{1}{2}}. \tag{2.26}$$

Here $T, T_0, \Delta t$ and τ_T represent the current temperature, required temperature, the time step and the coupling parameter between thermal atoms and the rest of the system respectively. The current temperature of the system is proportional to the average kinetic energy:

$$T = \frac{2U_{KE}}{3k_B N}, \tag{2.27}$$

and the required temperature is that of the thermal bath. The coupling parameter determines the rate at which the system is brought to a required temperature. This method is the chosen thermostat in our simulations due to it reaching a desired temperature smoothly, with minimal fluctuations. It generally reaches equilibrium faster than the Nosé-Hoover model.

The Nosé-Hoover thermostat is theoretically an improvement on the Berendsen thermostat but is susceptible to large temperature fluctuations as it oscillates around a required temperature making it more time consuming for modelling some systems. The thermostat was first developed by Nosé [36] and later improved by Hoover [35]. It controls the temperature of a system by altering the equation of motion such that

$$m_i \frac{d^2 \boldsymbol{r}_i}{dt^2} = \boldsymbol{F}_i - \zeta \frac{d\boldsymbol{r}_i}{dt}, \tag{2.28}$$

with ζ described in the rate of change equation

$$\frac{d\zeta}{dt} = \frac{1}{Q}\left(\sum_{i}^{N} v_i^2 - 3Nk_BT_0\right). \tag{2.29}$$

Here, Q is the coupling parameter, N is the number of atoms in the system, k_B is Boltzman's constant and T_0 is the required temperature of the system.

One of the main uses of a thermostat is to dissipate impact energy out of a small system during collision cascades or growth simulations. When impacts on a surface occur on a large system the impact energy would eventually dissipate away from the impact area. Because of computational constraints, growth simulations often use a small lattice to model the entire surface by implementing fixed and periodic boundary conditions which conserve energy within the system. Thermal layers are thus included in the system to extract excess heat after impacts. Another function of the thermal layers is to gradually increase the temperature of a system before impact simulations are carried out.

2.6 Energy Minimisation Techniques

Minimising a configuration of atoms such that all atoms relax into their minimum energy sites is necessary. Before and after successive atomic impacts, techniques are used to ensure the lattice is in its minimum energy state and relaxed. The minimisation techniques principally used are the steepest decent method and a conjugate gradient method [37]. The first is a simple and robust method that takes steps proportional to the negative gradient of the function at each point but can have slow convergence to a minimum.

Steepest Decent

If the function, $F(\boldsymbol{x})$, is differentiable in a neighbourhood of point $\boldsymbol{x}_n$, then it is known that the function decreases fastest in the direction of negative gradient of the function, $-\nabla F(\boldsymbol{x}_n)$.

It then follows that a sequence of points heading toward the minimum can be given by:

$$\boldsymbol{x}_{n+1} = \boldsymbol{x}_n - \alpha_n \nabla F(\boldsymbol{x}_n), \quad \text{For } n \geq 0, \tag{2.30}$$

where α_n is the distance along the negative gradient direction taken at step n. The values of α_n can be determined used a line search algorithm. Here, Brent's method [38] is used for the line search.

Conjugate Gradient

The idea of the conjugate gradient (CG) method is that for any quadratic function $f(x)$ of n arguments, the minima will be found in exactly n CG steps. However, as our potential functions are not quadratic, the CG method is a multi-step procedure with a test for convergence. The algorithm follows:

- **Step 1** - Calculate the value of of the negative gradient of the function:

$$G(\boldsymbol{x}_0) = -\nabla F(\boldsymbol{x_0}). \tag{2.31}$$

- **Step 2** - Find a new point: $\boldsymbol{x}_{n+1} = \boldsymbol{x}_n + \alpha_n \boldsymbol{s}_n$. For the first step, simply take $\boldsymbol{s}_0 = G(\boldsymbol{x}_0)$. The line search parameter, α_n, can be determined using Brent's method to find the minimum in the search direction.

- **Step 3** - Calculate $F(\boldsymbol{x}_{n+1})$ and $G(\boldsymbol{x}_{n+1})$, along with the new direction $\boldsymbol{s}_{n+1}$:

$$\boldsymbol{s}_{n+1} = G(\boldsymbol{x}_{n+1}) + \gamma_n \boldsymbol{s}_n \tag{2.32}$$

  where γ_n is found via the Polak-Ribière method [39]:

$$\gamma_n = \frac{||G(\boldsymbol{x}_{n+1})||^2 - G(\boldsymbol{x}_{n+1})^T G(\boldsymbol{x}_n)}{||G(\boldsymbol{x}_n)||^2} \tag{2.33}$$

- **Step 4** - Determine if the force is less than the specified tolerance, ϵ.

$$G(\boldsymbol{x}_{n+1}) \leq \epsilon. \tag{2.34}$$

If so, the minimum has been reached, else, increase n by 1 and return to step 2.

2.7 Visualisation

The ability to visualise the positions of atoms at discrete points in time during simulations is extremely useful. Data visualisation is a great advantage when analysing results. During MD simulations, multiple data files are created containing the positions of each atom at a particular point in time. These files can be visualised using the specialised visualisation software. For example: Atoman - analysis and visualisation of atomistic simulations [40] (Fig. 2.3) software developed by C.D.J. Scott. Each system of atoms can then be manipulated to show 360 degree views. With the addition of filters and colouring options, analysis can be made much simpler. These options include colouring a system by height or atomic species, visualising point defects and labelling atoms with coordination numbers. The evolution of a system over time during an MD simulation can also be made into a video clip such that the trajectories of atoms can be clearly seen. Atoman is also used to capture thousands of AKMC steps, creating video clips and still images.

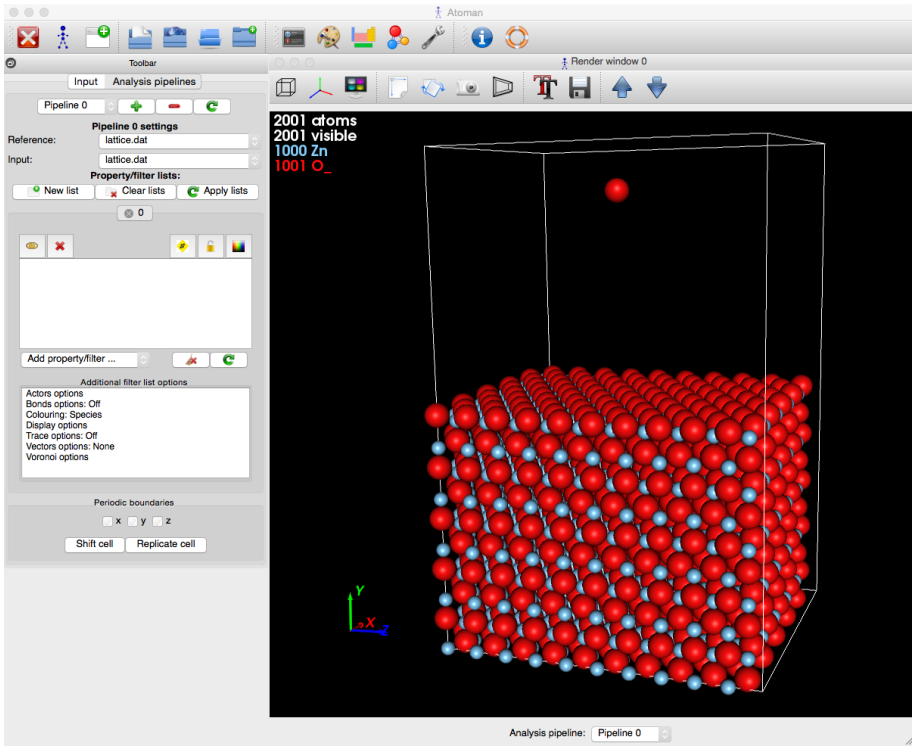

Figure 2.3 – The user interface of the Atoman suite. An example ZnO substrate is shown including a single O atom being deposited from above the surface.

Chapter 3

Methods II: Long Time Scale Dynamics

Using MD alone to model atomic systems over time scales greater than nanoseconds can be computationally unfeasible. Atomic processes that have high transition barriers are unlikely to have enough localised energy to take place within standard MD timescales but still need to be accounted for in many practical applications. Long time scale dynamics (LTSD) allows large systems to be modelled over extended timescales. Therefore, these techniques are useful when simulating surface growth. For this project, adaptive kinetic Monte Carlo (AKMC) [20] has been chosen due to the simplicity to apply the method in parallel. Transition searches can be performed on a number of processors. A lattice based AKMC method is also introduced in chapter 7 which allows larger systems to be modelled.

3.1 Search Methods

When the initial and the final states of a transition are known, within a KMC simulation, minimum energy pathways and the height of the energy barrier, can be calculated by using a double ended search method. Examples of double-ended search methods include the simple-string method [41] and the nudged elastic band (NEB) [42] method. Sometimes however, single-ended search methods with low accuracy can be more efficient when used in conjunction with a double-ended search method. Single-ended search methods include the Dimer [43], Activation

Relaxation technique (ART) [44] and the Relaxation and Translation (RAT) [45] methods, all of which are implemented into the Loughborough KMC (LKMC) package. They are used when only the initial state of a system is known.

The main search methods used in this thesis are the NEB, dimer and RAT methods which are described in the following sections.

3.1.1 Nudged Elastic Band Method

NEB is a double-ended search method developed by Henkelman and Jónsson [42] that is used for transition testing and refining transition barrier heights. It is used to find the minimum energy pathway between an initial and final state of a transition. Given the two endpoints, $\boldsymbol{R}_0$ and $\boldsymbol{R}_N$, first an estimate of the minimum energy pathway (MEP) is needed (often linear) consisting of $N+1$ images. At each image i, the real force vector, $\mathbf{F}_i$, can be split into parallel and perpendicular force components with respect to the tangent vector $\boldsymbol{\tau}_i$. The tangent vector at image i is dependent on the potential energy of the image relative to its neighbouring images.

For efficient implementation of the method, the tangent vector needs to be determined. If the image i, with potential V_i, where V_i is not a minimum or maximum along the band, then $\boldsymbol{\tau}_i$ is approximated by:

$$\boldsymbol{\tau}_i = \begin{cases} \boldsymbol{R}_{i+1} - \boldsymbol{R}_i & \text{if } V_{i-1} < V_i < V_{i+1}, \\ \boldsymbol{R}_i - \boldsymbol{R}_{i-1} & \text{if } V_{i-1} > V_i > V_{i+1}, \end{cases} \tag{3.1}$$

where $\boldsymbol{R}_i$ represents the position of image i. However, if the image i is a minimum or maximum i.e. $V_{i-1} > V_i < V_{i+1}$ or $V_{i-1} < V_i > V_{i+1}$, then,

$$\boldsymbol{\tau}_i = \begin{cases} (\boldsymbol{R}_{i+1} - \boldsymbol{R}_i)\Delta V_i^{max} + (\boldsymbol{R}_i - \boldsymbol{R}_{i-1})\Delta V_i^{min} & \text{if } V_{i-1} < V_{i+1}, \\ (\boldsymbol{R}_{i+1} - \boldsymbol{R}_i)\Delta V_i^{min} + (\boldsymbol{R}_i - \boldsymbol{R}_{i-1})\Delta V_i^{max} & \text{if } V_{i-1} > V_{i+1}. \end{cases} \tag{3.2}$$

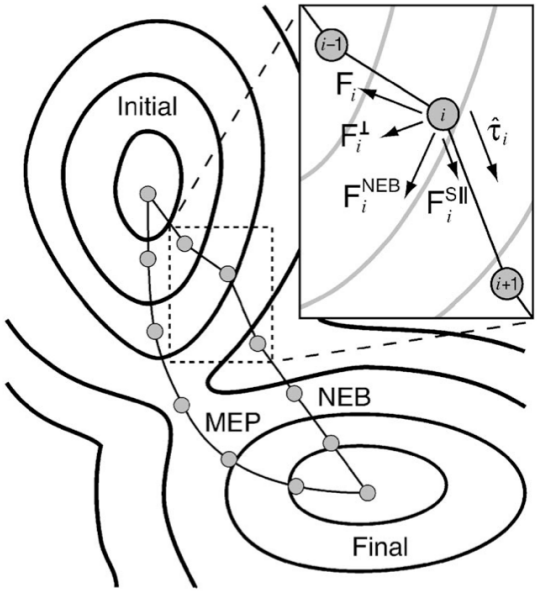

Figure 3.1 – Diagram showing an example of a minimum energy pathway (MEP) and the nudged elastic band (NEB) between two minima. The NEB is made up of several images, each with corresponding tangential and perpendicular forces. The images are then relaxed to the MEP. Image taken from [46].

Here ΔV_i^{min} and ΔV_i^{max} are the minimum and maximum absolute energy differences between V_{i-1}, V_i and V_{i+1} respectively. The perpendicular component of the force vector, $\boldsymbol{F}_i^{\perp}$, is then found by subtracting the tangential force from the real force vector, $\boldsymbol{F}_i$.

An artificial spring force, with spring constant K (determined empirically), is given by

$$\boldsymbol{F}_i^{S\parallel} = K(|\boldsymbol{R}_{i+1} - \boldsymbol{R}_i| - |\boldsymbol{R}_i - \boldsymbol{R}_{i-1}|)\hat{\boldsymbol{\tau}}_i, \tag{3.3}$$

where $\hat{\boldsymbol{\tau}}_i$ is the normalised tangential force vector, $\boldsymbol{\tau}$, found at the ith image. The pathway is then relaxed towards the minimum energy pathway by relaxing in the $\boldsymbol{F}_i^{NEB}$ direction which is the sum of the perpendicular force vector and the spring force:

$$\boldsymbol{F}_i^{NEB} = \boldsymbol{F}_i^{\perp} + \boldsymbol{F}_i^{S\parallel}. \tag{3.4}$$

The NEB is relaxed using a conjugate gradient minimiser. The perpendicular component of the force, $\boldsymbol{F}_i^{\perp}$, allows the images to relax downhill whilst the spring force retains equal spacing of images along the minimum energy pathway.

This search method is used to refine transitions found via the RAT method and to calculate barriers within a lattice based KMC simulation. In our off-lattice KMC simulations, NEB is one of the most computationally expensive components. Because of this, an attempt to improve the efficiency was considered by using an initial guess of the MEP closer to the actual MEP in the hope it will take less iterations to minimise.

To this end, a different initial MEP guess method was implemented into the NEB code. The image dependent pair potential (IDPP) method [47] is found to vastly improve the efficiency of transition searches where a linear approximation yields an unfavourable path. The initial interpolation works by creating a simple pair potential that only considers the distance between atoms in a system at various images. The interpolated distance between two atoms, i and j is given as

$$d_{ij}^{k} = d_{ij}^{\alpha} + k(d_{ij}^{\beta} - d_{ij}^{\alpha})/p, \tag{3.5}$$

where d_{ij} is the Euclidean distance between the i-th and j-th atoms. Here, α and β represent the initial and final states respectively, k denotes the image number and p the total number of images. A potential energy function for each image is then given by:

$$V_k^{IDPP}(r) = \sum_{i}^{N}\sum_{j>i}^{N} \omega(d_{ij}) \left(d_{ij}^{k} - \sqrt{\sum_{\sigma}(r_{i\sigma} - r_{j\sigma})^2} \right)^2 . \tag{3.6}$$

In Eq. 3.6, ω is a weighting function (taken as $\omega(d) = 1/d^4$) and $\sigma = x, y$ and z. NEB is then used to find the optimal path on the V^{IDPP} energy surface with an initial linear interpolation. The differences between linear interpolation and IDPP are shown in Fig 3.2.

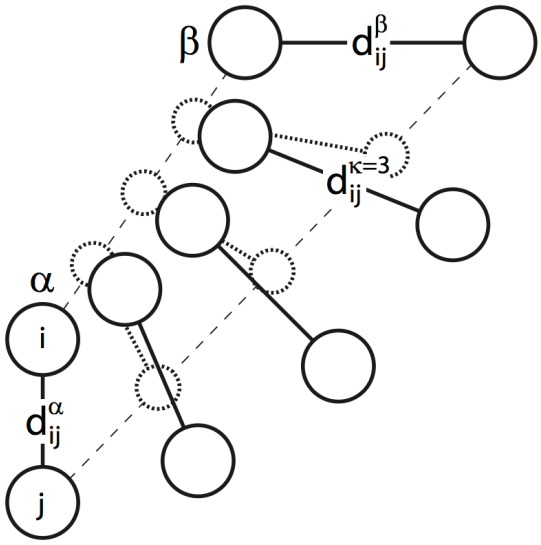

Figure 3.2 – Schematic diagram of paths generated by linear (dashed line) and IDPP (solid line) interpolation. Image taken from [47].

The result from the IDPP method is that all atoms that move in the transition keep a similar distance away from each other. This reduces the likelihood of the initial interpolation including atoms that are extremely close or intersect which may cause a highly unfavourable path.

To improve the efficiency of the method, two radii of atoms surrounding atoms that have moved during the image interpolation are used in energy calculations. The first radius of atoms (typically > second nearest neighbour, 2NN, distance) contains all atoms that are allowed to move during the interpolation minimisation whilst the second, larger radius (typically 2-3 Å larger than the first radius) contains all atoms that contribute to the IDPP potential energy and forces. All forces on atoms in the effective skin between the two radii are set to zero and and thus do not move during minimisation.

Despite the implementation of the IDPP interpolation method for NEB, the method does not increases the efficiency for all cases. For the majority of transitions during a typical simulation of Ag growth on ZnO surfaces, the IDPP method is equal to or less efficient than the linear interpolation method. The reason for this is that most diffusion events found in this system do

not follow highly unfavourable paths when a linear approximation is made to initialise NEB. A linear approximation in many cases is sufficient and only requires one NEB minimisation.

An example transition of a single Ag ad-atoms moving from an ABa to an ABc stacking site is shown in Fig. 3.3. Here, the IDPP and linear interpolations of NEB are compared using the model described in chapter 6. For the comparison, 9 images are used along the pathway and the combined forces on all the images is minimised to a tolerance of 0.1 eV/Å using the CG minimiser. The total time for the NEB method with the IDPP interpolation (on a single processor) to find the MEP is 23 seconds with 57 force evaluations. Whereas the linear interpolation is faster for this example; linear interpolation takes 21 seconds with a total of 51 force evaluations.

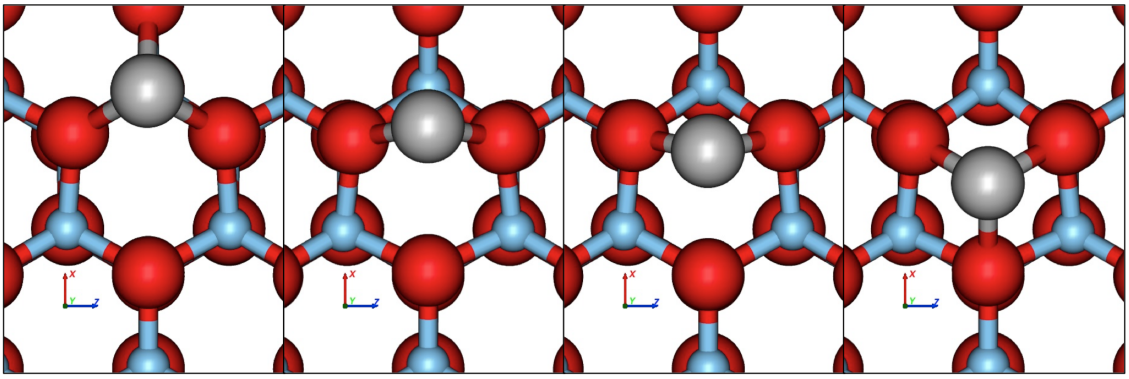

Figure 3.3 – An example transition (from left to right) of a single Ag ad-atom changing stacking sites from ABa to ABc used to compare NEB interpolation methods. The figures show 4 images along the MEP obtained via NEB using a linear interpolation.

3.1.2 Relaxation and Translation Method

The Relaxation and Translation (RAT) [45] method is a variation of the popular single-ended Activation Relaxation Technique (ART) [44]. Both methods rely on breaking up forces into parallel and perpendicular components using a tether point. The RAT method differs by having no bias towards linear transitions. This variation stems from how the lateral forces are minimised.

Force Minimisation

For the force minimisation, the point $\boldsymbol{R}$ is allowed to move along the plane bound by the span of the perpendicular vectors to the tether vector, $\boldsymbol{N}$ (Fig. 3.4). Throughout minimisations of the force components, the tether vector is kept constant. The relaxation step may actually move the point $\boldsymbol{R}$ a large distance from its original placement. As large movements are likely to occur, it is important to alter the size of each step along the perpendicular plane dynamically and efficiently. By empirical testing, a simple (and relatively crude) algorithm was produced to alter the step size α:

$$\alpha_{i+1} = \begin{cases} 1.2 \cdot \alpha_i & \text{if } (\boldsymbol{F}_i^{\perp} - \boldsymbol{F}_{i-1}^{\perp})/\boldsymbol{F}_i^{\perp} < 0.2 \\ 0.5 \cdot \alpha_i & \text{if } (\boldsymbol{F}_i^{\perp} - \boldsymbol{F}_{i-1}^{\perp})/\boldsymbol{F}_i^{\perp} \geq 0.2. \end{cases} \tag{3.7}$$

Here, $\boldsymbol{F}_i^{\perp}$ denotes the force perpendicular to the tether vector at the i-th minimisation step. The initial value for the step size for this work is $\alpha_0 = 0.02$ Å. This method forces the step size to increase if the change in force is too small or decrease otherwise. Whereas this is a relatively crude method, it is shown to have better efficiency than other methods including a 'regula falsi' method.

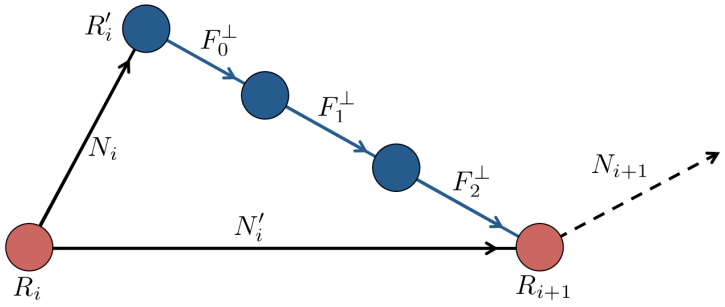

Figure 3.4 – Schematic diagram of the force minimisation process in the RAT method. Blue arrows indicate the direction of relaxation perpendicular to the tether vector $\boldsymbol{N}_i$. After minimisation, the new vector $\boldsymbol{N}_i'$ is created linking $\boldsymbol{R}_0$ to $\boldsymbol{R}'$. The normalised sum of the two vectors $\boldsymbol{N}_i$ and $\boldsymbol{N}_i'$ create the new tether vector $\boldsymbol{N}_{i+1}$.

Translation

The RAT method also differs from the ART method by the fact it uses previously calculated displacement vectors. After each relaxation step, a pair of vectors, $\boldsymbol{N}_i$ and $\boldsymbol{N}_i'$, are produced that describe the initial displacement and the final displacement from the tether point respectively. A new translation vector is then given by the normalised sum of the vectors:

$$\boldsymbol{N}_{i+1} = \frac{\boldsymbol{N}_i + \boldsymbol{N}_i'}{|\boldsymbol{N}_i + \boldsymbol{N}_i'|}. \tag{3.8}$$

The relaxation and translation steps are then repeated until the dot product of the parallel force component and displacement vector turns positive. This then indicates that a saddle is found.

3.1.3 Dimer Method

The Dimer method is a single-ended search method developed by Henkelman and Jónsson [43]. The method involves two copies of the system atoms closely separated representing two offset points which are then rotated and translated towards a saddle point. Firstly, a point $\boldsymbol{R}$ is chosen along a random displacement vector $\hat{\boldsymbol{N}}$ away from the initial state. Two images, $\boldsymbol{R}_1$ and $\boldsymbol{R}_2$ are then separated from the midpoint $\boldsymbol{R}$ by a distance ΔR along the vector $\hat{\boldsymbol{N}}$ such that:

$$\boldsymbol{R}_1 = \boldsymbol{R} + \Delta R\hat{\boldsymbol{N}}, \tag{3.9}$$

$$\boldsymbol{R}_2 = \boldsymbol{R} - \Delta R\hat{\boldsymbol{N}}. \tag{3.10}$$

Here, ΔR is chosen dependent on the system considered. The method is then split into two parts: dimer rotation and dimer translation. Rotating the dimer is used to find the minimum curvature orientation. The force acting on each image is composed of parallel and perpendicular components. The perpendicular component for the ith image, $\boldsymbol{F}_i^{\perp}$, is found by subtracting the

parallel component from the real force vector acting on an image $\boldsymbol{F}_i$, i.e.

$$\boldsymbol{F}_i^{\perp} = \boldsymbol{F}_i - (\boldsymbol{F}_i \cdot \hat{\boldsymbol{N}})\hat{\boldsymbol{N}}. \tag{3.11}$$

The global rotational force, $\boldsymbol{F}^{\perp}$ and curvature, C, are then given by:

$$\boldsymbol{F}^{\perp} = \boldsymbol{F}_1^{\perp} - \boldsymbol{F}_2^{\perp}, \tag{3.12}$$

$$C = \frac{(\boldsymbol{F}_2 - \boldsymbol{F}_1) \cdot \hat{\boldsymbol{N}}}{2\Delta R}. \tag{3.13}$$

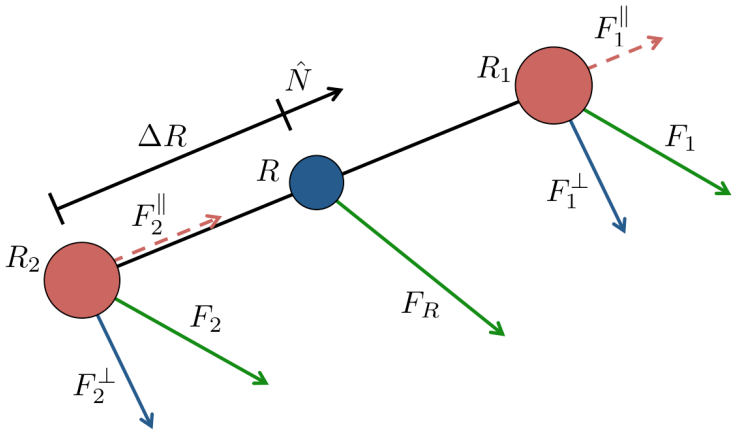

Figure 3.5 – Illustration of a dimer described by two points, $\boldsymbol{R}_1$ and $\boldsymbol{R}_2$, with corresponding real forces, $\boldsymbol{F}_1$ and $\boldsymbol{F}_2$, split into parallel and perpendicular components. The dimer is rotated and translated along the line of minimum curvature, C, described by a relation between forces and displacement vector, $\hat{\boldsymbol{N}}$.

The dimer is then minimised to a line of lowest curvature by the minimisation of $\boldsymbol{F}^{\perp}$ involving a conjugate gradient step and a rotational equivalent minimiser to reduce rotational force acting on the dimer. Numerous minimisation methods can be used, a selection of such have been tested by Henkelman and Jónsson [43].

Dimer translation is then considered. A first order saddle point is a maximum along the lowest curvature mode and minimum along all other modes. Near a minimum, C will be positive and

as the dimer moves closer towards a saddle, C will become negative. Due to this, the dimer is translated using a modified force $\boldsymbol{F}^m$ depending on the curvature:

$$\boldsymbol{F}^m = \begin{cases} -\boldsymbol{F}^{\parallel} & \text{if } C > 0, \\ \boldsymbol{F}_R - 2\boldsymbol{F}^{\parallel} & \text{if } C < 0. \end{cases} \tag{3.14}$$

Here, the net real force acting on the dimer is given by $\boldsymbol{F}_R$ and the parallel component is given by $\boldsymbol{F}^{\parallel}$. By translating the dimer along the modified force direction and rotating as mentioned above, the method will find a saddle point.

The dimer method is a computationally efficient method for finding saddle points but for the Ag/ZnO surface interactions considered in this work the RAT method results in more successful transitions being found. Hence, the RAT method is the single ended search method used for this research. It is also combined with the NEB method to determine saddle heights more accurately.

3.2 Defining Defects

One of the challenges with many long time scale dynamics methods is selecting which atoms are allowed to move. In our AKMC, if a crystal structure is considered, only defects or atoms surrounding defects are allowed to diffuse. The assumption is made that all other atoms are in stable sites and require a large amount of energy to move from those sites. For our simulations, a radius (equal to the fourth nearest neighbour) of atoms surrounding a defect are considered when conducting search algorithms. This region is called a 'defect volume' (DV). Whilst calculating which atoms around a defect are allowed move is trivial, defining what classes as a defect is less so.

Typically in bulk simulations, to find defects, a system is compared to a reference system.

This reference system is often a perfect crystalline structure of the material used. Defects are then defined by any atoms that have displaced from a lattice site or any new atoms that have appeared. However, this simple method has inherent problems with it. During collision cascade simulations, a whole section of the system can shift in one direction whilst maintaining the majority of the crystal structure. If this is then compared to a reference lattice, every atom within the section that shifted would be considered a defect despite many of them being in perfect crystalline structures relative to neighbouring atoms. This method also falls down when surface growth is simulated. If all deposited atoms are considered as defects, irrespective of their local environment, the total calculations become increasingly long and more transition searches are conducted on a system than would necessarily need to be done as deposited atoms can also sit in stable crystalline sites. In the implementation of this method, defects within a close radius of each other are combined to form a single defect volume (Fig. 3.6). This whole defect volume is then used when conducting transitions searches.

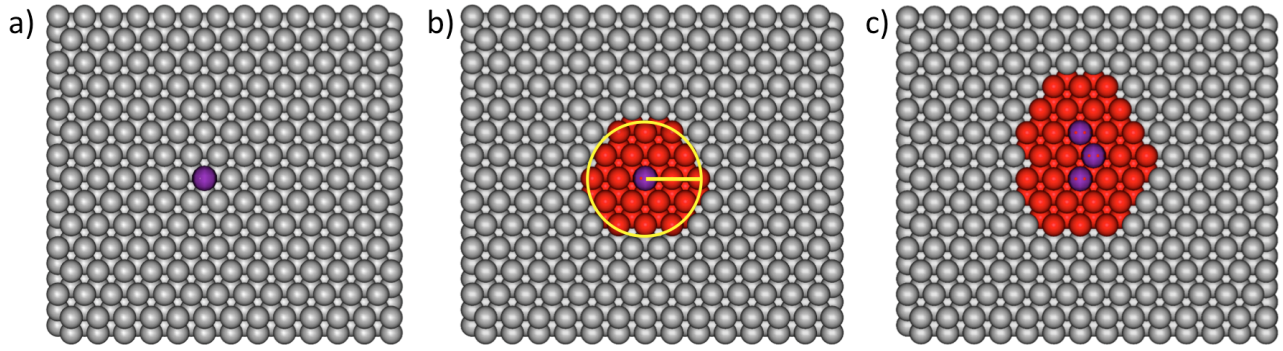

Figure 3.6 – Schematic showing how defect volumes are constructed from an initial defect (a) and combined with all atoms within a radius of the defect (b). If multiple defects are found within this radius (c), the defect volumes are combined into one single defect volume. Here grey spheres represent a defect free surface, purple spheres represent defects and red spheres indicate atoms included in the defect volume surrounding a defect.

Another commonly used defect finding method uses the coordination number of each atom to decide whether it is a defect or not. The coordination number of an atom is the number of its nearest neighbours. For FCC and BCC structures the coordination numbers are 12 and 8 respectively. If an atom has less nearest neighbours than expected (under-coordinated), it is

then considered a defect. This method of identifying defects is more computationally expensive but defines defects on a local level rather than considering a global comparison. To compute the coordination of an atom, a radius around that atom is created. All atoms within such radius are counted and then a coordination number is given. When considering systems with surfaces, all atoms at the surface would be considered under-coordinated if a minimum coordination number to be accepted as a non-defect was that of an atom in bulk. However, atoms within a lot of surfaces are still very stable and are very unlikely to move during a long time scale dynamics simulation. This means the minimum coordination number may be reduced to that of surface atoms in a perfect crystalline structure for the purposes of searching for local transitions. For this defect definition method, neighbouring defects are not combined into single defect volumes.

3.3 Atom Lists and Volumes

When running long time scale dynamics on large systems, many of the computationally expensive elements are conducted on subsystems to improve efficiency. These subsystems, or volumes, come in various sizes depending on their role within the method. These lists of atoms are created by including all atoms within a radius around a defect. The volumes used in this work are described below in ascending order of size.

- **Initial Search Volume**: is used to create a list of atoms that are randomly displaced when conducting single-ended search methods like the RAT method. The volume typically consists of all 2NN atoms. This volume includes red and yellow coloured atoms in Fig. 3.7.

- **Graph Volume**: is commonly referred to as the "**defect volume**" (DV) throughout this work. It is used when matching defects and surrounding atoms for the purpose of reusing previously found transitions. It is also used for determining combined volumes. Combined volumes can exist when multiple defects are within the graph radius of each other. When multiple defects are this close together, a combined volume is created as

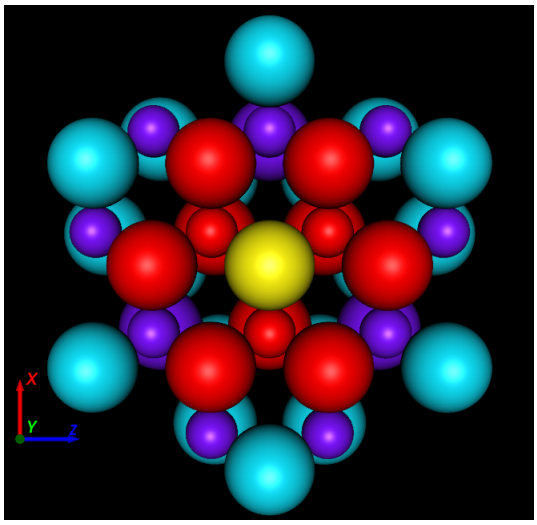

Figure 3.7 – Schematic showing included atoms in various volumes for the ZnO system. Here yellow is the given defect. The red and yellow atoms belong to the initial search volume. The graph volume is a union of the purple atoms and the initial search volume whereas the search move volume also includes the blue atoms.

a union of the individual graph volumes. This volume is typically constructed of atoms within the 4NN distance of a defect. This volume includes purple, red and yellow coloured atoms in Fig. 3.7.

- **Search Move Volume**: controls the number of atoms that are included when searching for saddle points using a single-ended search method. This volume typically includes atoms within 5/6NN distances. This volume includes blue, purple, red and yellow coloured atoms in Fig. 3.7.

The values used for each radius are encouraged to be small for computational efficiency but must be large enough for search algorithms to find all feasible transition events. For our system, only atoms in a close neighbourhood (within 2NN distance) of defects are likely to move significantly enough to be considered a transition. During a transition, atoms outside of the graph radius should not move and as such the graph volume is used within the reuse algorithm described in Section 3.5. For our system, the 4NN distance is large enough to incorporate all moving atoms. The search move radius is chosen to be large enough such atoms outside the volume have a negligible effect (< 0.01 eV) on transition barriers within the initial search volume.

3.4 Transition Search Algorithm

By using single and double ended search algorithms (introduced in section 3.1), a set of transitions can be produced for a given state of a system. Transition searches are conducted on defect volumes to find surrounding saddle points and unique transitions. For each defect volume, the algorithm used in this work to find a list of possible transitions is as follows:

- **Step 1: Initial displacement** - For a given defect volumes, randomly displace atoms included in the Initial Search Volume.
- **Step 2: Saddle search** - Use the RAT method (introduced in section 3.1.2) to approximate surrounding saddle point positions .
- **Step 3: Construct the final state** - Push atoms in the saddle in the direction of the displacement vector between the initial state and saddle. Then relax the resulting system to a minimum.
- **Step 4: Check uniqueness** - Determine if the final state is unique by calculating the separation of atoms in the DV to previously found final states in this step. If the separation is less than a given tolerance, discard the transition as a duplicate.
- **Step 5: Saddle refinement** - Use NEB (introduced in section 3.1.1) to refine the saddle point position and corresponding barrier height.
- **Step 6: Calculate the rate** - Calculate the rate value for the transition based on the obtained transition barrier height and the Arrhenius equation (Eq. 3.22).

This algorithm is typically repeated 100s of times for each defect volume to maximise the proportion of possible transitions found. Transition searches are split between multiple processors as a simple method of running a LTSD simulation in parallel. If any of the steps fail in algorithm, the transition search in considered a failure. Failure can be caused by poor initial displacement directions or slow convergence.

3.5 Reuse of Transitions

One method to increase efficiency within a LTSD simulation is to reuse transitions that have already been calculated. Transition searches are usually the most computationally expensive parts of a LTSD model. By reusing transitions, the computation time to find a set of transitions reduces. However, transitions can only be reused for similar states in a system. To determine what classes as a similar state, each state is given a label (or hash key) associated with the connectivity of atoms in a defect volume.

3.5.1 Nauty

During our LTSD simulations, "Nauty" (No AUTomorphisms, Yes?) [48] is used for computing automorphism groups of graphs with the ability to produce canonical labelling in the form of a hex number (or hash key). "Nauty" is used for two main purposes: to determine if two graphs (two defect volumes) are identical and if so, to produce the isomorphism between them.

The first task can be dealt with simply by "Nauty" procedures. Each graph is labelled by a hash key depending on the graph's isomorphism group. If two graphs share the same hash key, they are deemed isomorphic. For our work, defect volumes are treated as graphs of atoms and hash keys are calculated for each volume. If two defect volumes share the same hash key, they are considered as similar and transitions can be reused.

The isomorphism determination is also done simply within "Nauty". Given two graphs, provided they are isomorphic, a sequence of pairs, $[a_i, b_i]$, are returned where a_i is the index of a vertex in the first graph and b_i is the corresponding vertex in the second graph. The types of defect structure are classified by means of a hash key.

Lazauskas provides a detailed example of how a hash key is determined for an example defect

volume [14]. In this example, a defect volume is provided with a single vacancy in the centre. The system is made up of Fe atoms. A connectivity graph is produced in relation to all atoms in the volume. Atoms are considered connected if the separation between them is less than the graph radius. A unique hash key is then produced for all configurations that share the same connectivity graph. This is shown in Fig. 3.8.

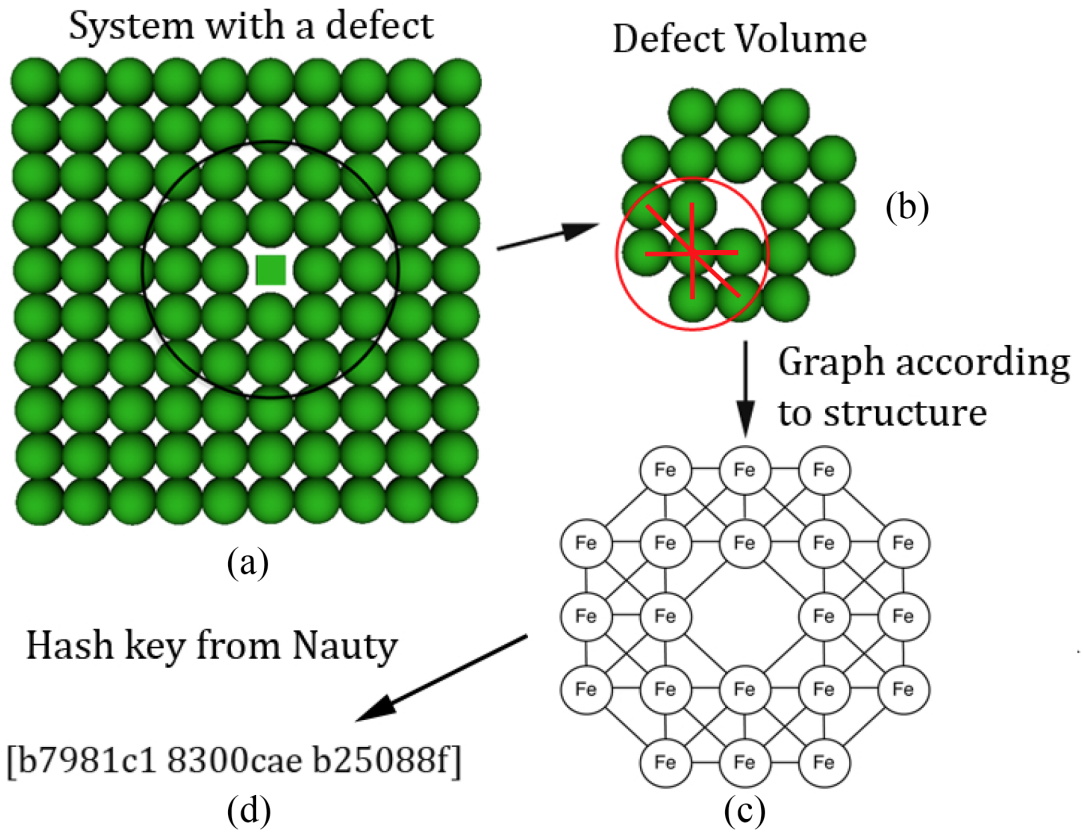

Figure 3.8 – Schematic describing the procedure for determining the connectivity graph and hash key for a defect volume. Here (a) - describes finding atoms in the defect volumes, (b) - the connectivity between atoms, (c) - creating a graph relating to the a connectivity of atoms and (d) - generating a hash key for the graph. Image is taken from [14].

3.5.2 Transformation Matrix

Once an isomorphism is found between two defect volumes, a transformation is needed to alternate between the two states. For this, a transformation matrix is approximated. Transformation matrices can incorporate multiple manipulations on a shape including stretching, rotation, translation and reflection. A transformation matrix, $\boldsymbol{A}$, is defined such that

$$\boldsymbol{AX} = \boldsymbol{X'}, \tag{3.15}$$

where, $\boldsymbol{X}$ is a vector representing the position of an atom in the primary defect volume and $\boldsymbol{X'}$ is the vector representing the corresponding atom found via "Nauty" in the other defect volume. The transformation matrix then gives information on how to map one defect volume to another. To find the transformation matrix, $\boldsymbol{A}$, an overdetermined linear system of equations is produced using all the atoms from both defect volumes. The overdetermined system is to help fit a transformation matrix to all the atoms in the system whereas a completely determined linear system is unlikely to be a good representation of the transformation for all atoms. To best fit the transformation matrix, the method of least squares is used. There are three sets of overdetermined linear systems of equations derived from Eq. 4.3:

$$\begin{pmatrix} x_{11} & x_{12} & x_{13} \\ x_{21} & x_{22} & x_{23} \\ \cdots & \cdots & \cdots \\ x_{n1} & x_{n2} & x_{n3} \end{pmatrix} \begin{pmatrix} a_{i1} \\ a_{i2} \\ a_{i3} \end{pmatrix} = \begin{pmatrix} x'_{1i} \\ x'_{2i} \\ \cdots \\ x'_{ni} \end{pmatrix} \quad \text{For} \quad i = 1, 2 \text{ and } 3. \tag{3.16}$$

Here, n represents the number of atoms in the defect volumes and i denotes the coordinate number by which each overdetermined linear system is created. Also, the triplets (x_{j1}, x_{j2}, x_{j3}) represent the 3 coordinates of the j-th atom in the first defect volume, x'_{ji} represents the i-th coordinate of the j-th atoms in the second defect volume and the values a_{ij} determine the coordinates of the transformation matrix, $\boldsymbol{A}$. In this system of equations, the isomorphism

between volumes must be taken into account so that x_j corresponds to x'_j. To eliminate the need for the transformation matrix to describe translation, all atom positions for a defect volume are first centred to the origin about the centre of mass.

3.5.3 Centre of Mass with Periodic Boundaries

When comparing defect volumes and calculating transformation matrices, the centre of mass (COM) of a defect volume is used. Without periodic boundary conditions, all positions of atoms in a defect volumes are added together and an average position (or centre of mass) is calculated. As two neighbouring atoms can be opposites sides of the simulation box when periodic boundaries conditions are used, a simple centre of mass calculation is not sufficient for many cases. To correctly include the periodic boundaries into the COM calculation, each coordinate is mapped to an angle of a circle [49]. For each atom i, an angle in the σ direction can be obtained via:

$$\theta_i = 2\pi \frac{\sigma_i}{\sigma_{max}}, \tag{3.17}$$

where σ_{max} corresponds to the simulation box length in the σ direction. Thus, $\sigma_i \in [0, \sigma_{max})$. The angle can then be mapped to two points:

$$\begin{aligned} \xi_i &= \cos(\theta_i), \\ \zeta_i &= \sin(\theta_i). \end{aligned} \tag{3.18}$$

After summing for all atoms, i, the average points $\bar{\xi}$ and $\bar{\zeta}$ can be determined. These values can then give a new angle $\bar{\theta}$ and which is then mapped to a coordinate of the centre of mass, σ_{COM}:

$$\bar{\theta} = \text{atan2}(-\bar{\zeta}, -\bar{\xi}) + \pi, \tag{3.19}$$

where atan2 is defined in terms of the standard arctan function as:

$$\text{atan2}(y,x) = \begin{cases} \arctan(\frac{y}{x}) & \text{if } x > 0, \\ \arctan(\frac{y}{x}) + \pi & \text{if } x < 0 \text{ and } y \geq 0, \\ \arctan(\frac{y}{x}) - \pi & \text{if } x < 0 \text{ and } y < 0, \\ \frac{\pi}{2} & \text{if } x = 0 \text{ and } y > 0, \\ -\frac{\pi}{2} & \text{if } x = 0 \text{ and } y > 0, \\ \text{undefined} & \text{if } x = 0 \text{ and } y = 0 \end{cases} \tag{3.20}$$

This then gives the coordinate of the centre of mass:

$$\sigma_{COM} = \sigma_{max}\frac{\bar{\theta}}{2\pi}. \tag{3.21}$$

This can be repeated for all directions in which periodic boundary conditions are used to obtain the COM of a defect volume.

3.5.4 Reuse Algorithm

Every time a new set of searches are conducted on a defect volume, the initial atom positions are saved along with all successfully found transitions' saddles and final positions. This information is then stored in a file named after the hash key given to the volume. If another occurrence of this hash key appears during a LTSD simulation, the previously found results can be utilised making the need to do computationally expensive transitions searches unnecessary. The algorithm for doing this is split into 5 steps:

- **Step 1** - Find the transformation matrix between the two defect volumes.
- **Step 2** - Reuse the final state. Apply the transformation matrix to the final atom positions of each transition to obtain a new final state approximation.
- **Step 3** - Reuse the saddle state. Apply the transformation matrix to the atoms positions

at the saddle to obtain a new saddle state approximation.

- **Step 4** - Relax the final state approximation to a local minimum.
- **Step 5** - Run a double ended search method (e.g NEB) through the saddle point to achieve a refined transition barrier height
- **Step 6** - Calculate the rate value for the transition based on the newly obtained transition barrier height and the Arrhenius equation (Eq. 3.22).

3.6 Kinetic Monte Carlo

KMC is a LTSD method that assigns atoms to lattice sites and predefines all possible transitions. To recreate stochastic behaviour, we use the Arrhenius equation:

$$\text{Escape Frequency} = v \cdot e^{-E_b/k_B T}, \tag{3.22}$$

where v, E_b and k_B are the transition prefactor, transition barrier and the Boltzmann constant respectively and T is the temperature in Kelvin. The transition prefactor, v, can be calculated using the Vineyard method [50] but is often taken to be 10^{13} per second for surfaces [45] to reduce calculation time. Once the search methods have found all possible transitions, energy barriers and attempt frequencies, for a given configuration, the relative probability of each transition being chosen can be found. To implement a KMC simulation we follow the following algorithm:

- **Step 1** - Set time, t, to zero.
- **Step 2** - Produce a list of all possible events for the given configuration.
- **Step 3** - Use the Arrhenius equation to calculate transition rates for all given transition barriers along with the sum of all the rates R.

- **Step 4** - Generate a random number P between 0 and R.
- **Step 5** - Go through every event cumulatively until P is passed to find an event to carry out.
- **Step 6** - Carry the event out and move forward to the next step.
- **Step 7** - Increase the time of the system by Δt. Here $\Delta t = -\log u/R$, where u is a random number generated between 0 and 1.
- **Step 8** - Return to step 2.

This method makes the assumptions that each state is in a local minimum, all possible transitions are found and that all transition events are uncorrelated. That is, the probability for a transition event to occur is independent of the previous transition. Note that the average value of $-\log u$ in the time step is equal to unity and is used to describe the stochastic nature of the Poisson process [51].

3.6.1 Adaptive Kinetic Monte Carlo

For the adaptive (on-the-fly) method [20], all defects must be defined in the system and then transition searches are only then considered in a search space consisting of defects and nearby atoms or "defect volume". Using search methods like NEB and RAT (discussed above), transitions and energy barriers are found. The possible transitions and external deposition or collision events are entered into a KMC roulette and an outcome is randomly selected (as in the KMC method) to evolve the system.

The Loughborough AKMC (LAKMC) package is used to run AKMC simulations. In the package, various parameters (such as volume radii, successful transition criteria and minimisation tolerances) can be fitted and can help improve efficiency for each individual system. Search results from each step can be stored and then reused later in a simulation if similar defects are

found in the system. Other methods to increase efficiency of the package are constantly being considered and implemented into the code. For all simulation methods requiring extensive computation, efficiency is of high interest. Parallelisation of MD and AKMC is necessary for more efficient long time scale growth simulations. AKMC is typically run in parallel where transition searches are conducted on each processor. If a transition search is successful or not then the corresponding processor begins a new search, provided the maximum number of searches has not been exceeded. All successful transition search results are collated and entered into a roulette along with the deposition event and a new event is chosen; either a transition or external event is chosen to evolve the system.

3.6.2 Lattice Adaptive Kinetic Monte Carlo

The lattice based version of AKMC relies on atoms sitting in perfect lattice sites. Its advantage over the method described above is that it is faster so that larger systems can be studied. However, it considers only single atom moves and misses out the MD step for deposition events during growth simulations. In the method developed here, it is assumed that all possible transitions are restricted to an atom moving from its lattice site to one of its nearest neighbouring lattice sites. In some lattice based AKMC methods, transitions barriers are determined according to a bond counting model that alters the rate of transitions according to the number of bonds a single atom has [52, 53]. With this simplified method of finding transitions rates, the lattice based AKMC simulation is extremely efficient. However, the bond counting model often only accounts for atoms within a second nearest neighbour distance away from the chosen atom.

In many systems, atom arrangements within a system outside of the 2NN distance can still have a large effect on transition rates. In the model used in this work, a large radius is considered surrounding a chosen atom, over 5NN distance (5.9 Å), and this can be increased or decreased as necessary for different systems. The radius is chosen such that atoms that move outside of

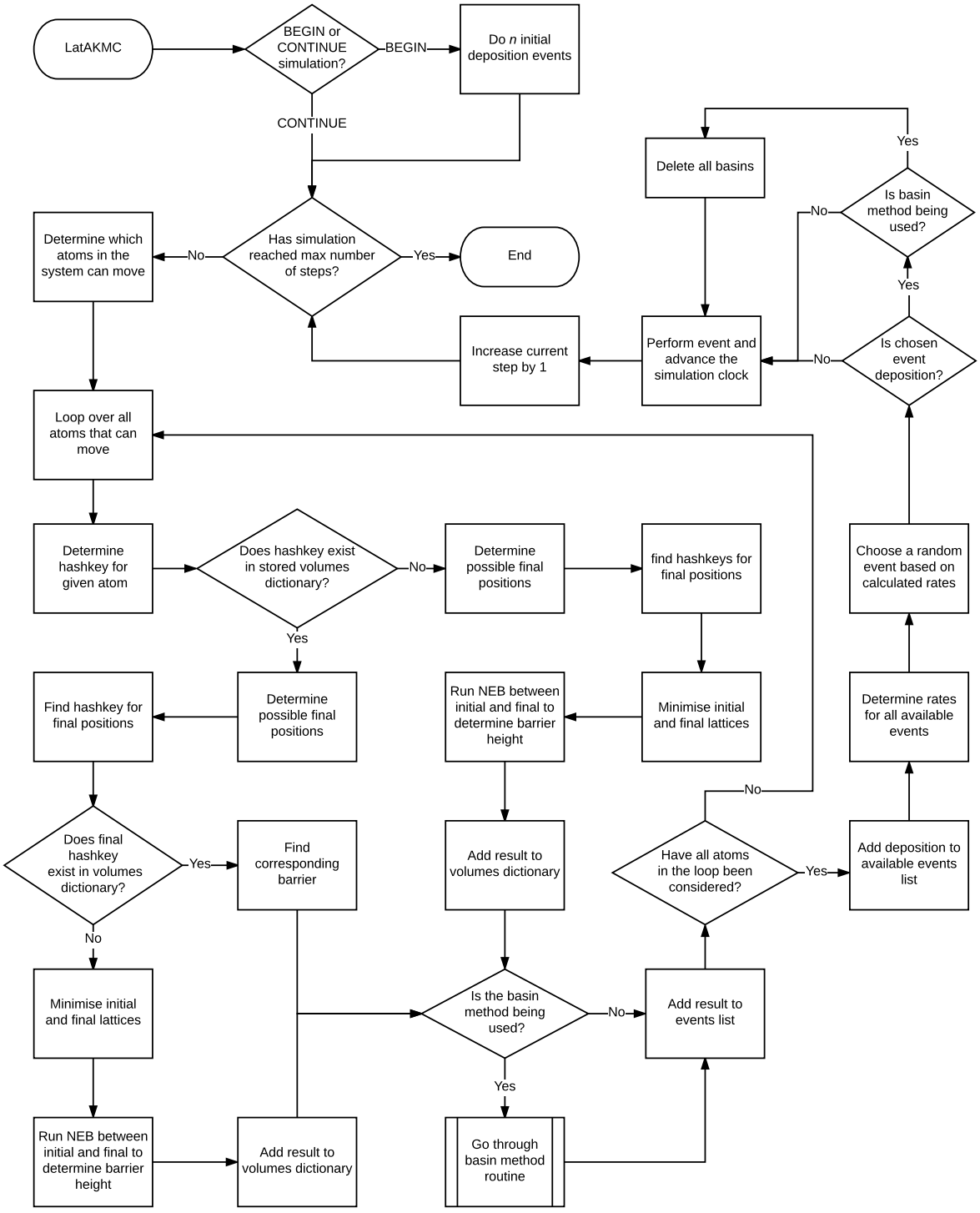

Figure 3.9 – Flowchart describing the process for a lattice AKMC simulation. The basin method routine is separate from the main code and this technique is described in the next section.

the radius have a negligible effect (< 0.01 eV) on barrier heights of the atom considered. The model also accounts for the connectivity surrounding a chosen atom and the type of elements in the local radius. Each atom is given a hash key that labels the local configuration (as in the off-lattice model). A double ended search method, typically NEB, is then used to calculate barrier heights between near lattice sites after relaxation. The final configuration is also given a hash key to identify its local environment. If the two hash keys occur within a simulation again, the transition can only then be reused. This method better predicts the diffusion energetics in a system than lattice based methods based on pre-defined event lists but at the cost of lower computational efficiency. However, this method is still more efficient than the off-lattice model.

The lattice based AKMC (LatAKMC) model used in this work was developed by harnessing and adapting some sections from the Loughborough AKMC program. The basic outline of how the code works is described in Fig. 3.9 and is further discussed in chapter 7 when applied to Ag growth on ZnO surfaces.

3.7 Basin Method

A problem that plagues many long time scale methods is the occurrence of small energy barrier transitions dominating a simulation with no substantial net diffusion. Examples of this can be seen in surface growth simulations; often ad-atoms can form dimers or small clusters that can rotate with small energy barriers [13]. During a standard KMC simulation, these small energy barrier transitions have a very large rate of occurrence and so are likely to be chosen in the roulette again and again before another transition is chosen. This essentially wastes computational time. To combat this problem, either set low barrier transitions are blocked or a basin method is used. The latter has been implemented for the lattice AKMC examples. Fig.3.10 describes how transitions are categorised and which states are included within a "super-basin". For the lattice based AKMC method, an implementation of the mean rate

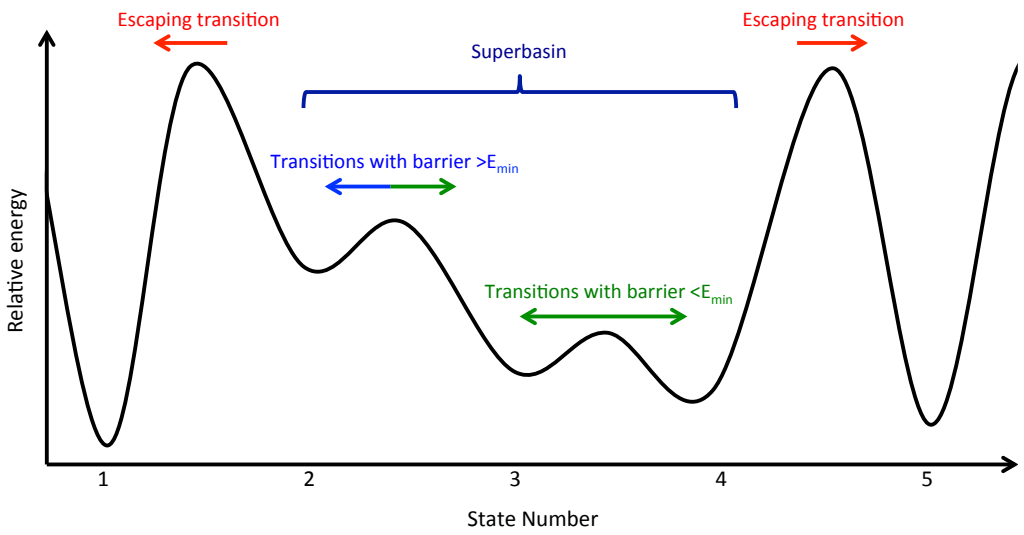

Figure 3.10 – A diagram describing an example 1D energy surface with a super-basin. Green arrows indicate transitions with energy barriers less than the basin tolerance E_{min}. States with transitions that have energy barriers less than the tolerance (states 2,3 and 4) are included within a basin. The blue arrow indicates a transition that is included in the basin but has a barrier $> E_{min}$. This state is included in the basin because the reverse barrier is $< E_{min}$. Red arrows indicate escaping transitions: that is transitions with energy barriers $> E_{min}$ leaving a basin (meaning the reverse barrier must also be larger than E_{min}. The transitions from states 2 to 1 and 4 to 5 are considered escaping transitions.

method (MRM) [54] is used to calculate the mean residence time of atoms in basins. This is added alongside code that will automatically recognise basins by considering the forward and reverse transition barrier heights. If transition barrier heights are beneath a threshold (given in the input file), the initial and final states are added to a basin. All previously explored states within the basin are blocked from being reentered and other transitions rates are modified according to the MRM until an escaping transition is chosen.

3.7.1 Mean Rate Method

The mean rate method (MRM) [54] is used to calculate the mean residence time in basin states before leaving the basin. To calculate the probability that an atom will exit the basin (or island), we first calculate the probability matrix $\underline{\mathbf{T}}$ (only including states within the basin),

with elements

$$\begin{aligned} T_{j,i} &= \frac{R_{i\to j}}{\sum_k R_{i\to k}} = \tau_i^1 R_{i\to j}, \\ \tau_i^1 &= \frac{1}{\sum_k R_{i\to k}}, \end{aligned} \tag{3.23}$$

where $R_{i\to j}$ is the rate to go from state i to state j within the basin. The summation $\sum_k$ is over all states within and out of the basin. The reciprocal of the sum τ_i^1 is the mean residence time in state i each time that state is visited. To find the probability that a state is occupied after in-basin move m, an occupation probability vector of all basin states is given by repeat application of $\underline{\mathbf{T}}$ to the initial occupation probability:

$$\begin{aligned} \mathbf{\Theta}(m) &= \underline{\mathbf{T}}^m \mathbf{\Theta}(0), \\ \mathbf{\Theta}_i(0) &= \begin{cases} 1 & \text{if state } i \text{ is the initial state} \\ 0 & \text{otherwise.} \end{cases} \end{aligned} \tag{3.24}$$

The mean residence time in basin state i before leaving the basin is then given by:

$$\tau_i = \tau_i^1 \mathbf{\Theta}_i^{sum}, \tag{3.25}$$

where,

$$\mathbf{\Theta}_i^{sum} = \sum_{m=0}^{\infty} \underline{\mathbf{T}} \mathbf{\Theta}(0) = (\mathbf{I} - \underline{\mathbf{T}})^{-1} \mathbf{\Theta}(0). \tag{3.26}$$

Thus, the mean time to escape the basin (or island) is then given as the sum of mean residence times within the basin.

3.7.2 Code Implementation

The development of the basin method implementation within the AKMC and LatAKMC code at Loughborough was one of the main tasks of the this research project. The basic outline of how the basin code is structured within AKMC is described within a flow chart (Fig. 3.11). New basins are created if forward or reverse transition energy barriers are smaller than a given

tolerance. Once a basin is created, transitions rates are adjusted according to the MRM.

In LatAKMC, the basin method is implemented using the same principle ideas. The main difference between the two methods comes from the way defects are stored. In AKMC, the whole of a defect volume is stored, including all the atom positions and elemental species. This is done so that two similar defect volumes can be compared because sometimes the hash keys assigned to them can be different. If these states are effectively the same, then reuse can be implemented. In LatAKMC, as atoms are restricted to lattice sites, actual positions are not needed for the basin code; only the hash key and the lattice site of the moving atom are required. The code structure for the basin method in LatAKMC is described in Fig. 3.12.

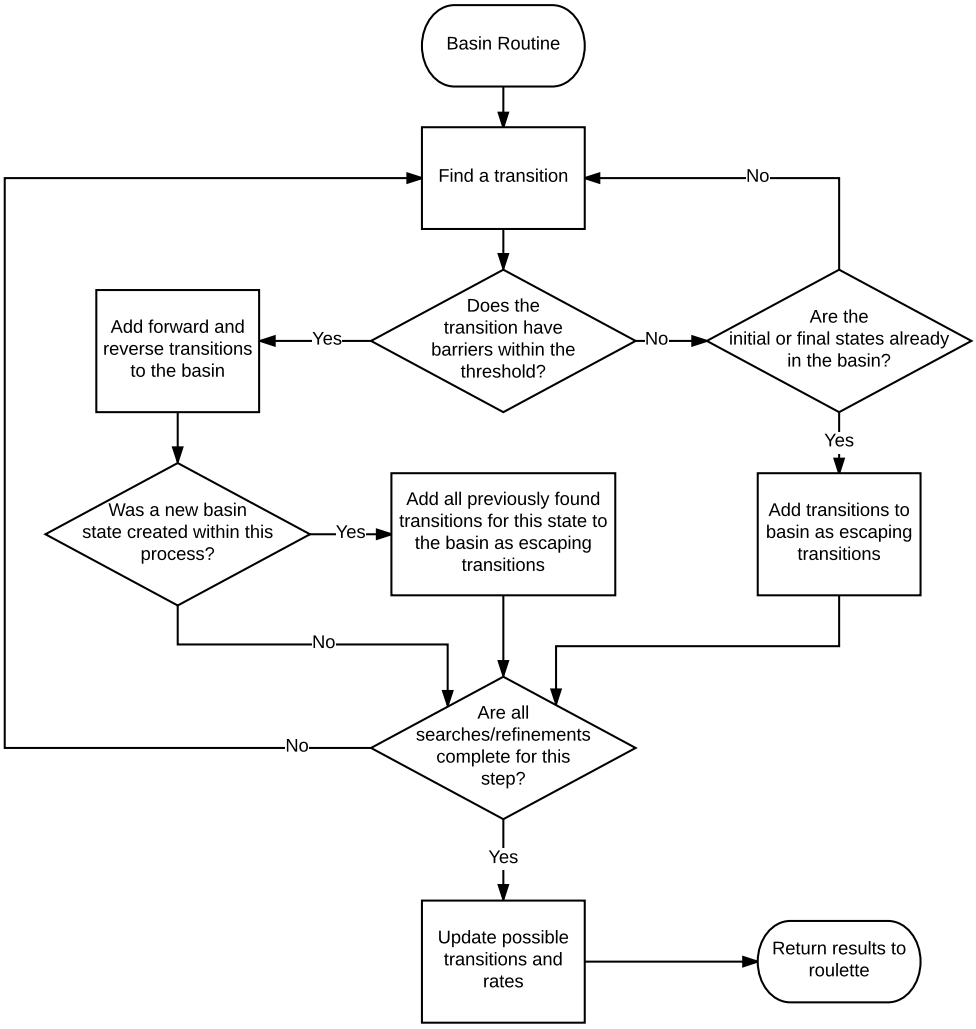

Figure 3.11 – A simplified flow chart representing how the basin method is implemented within the AKMC code.

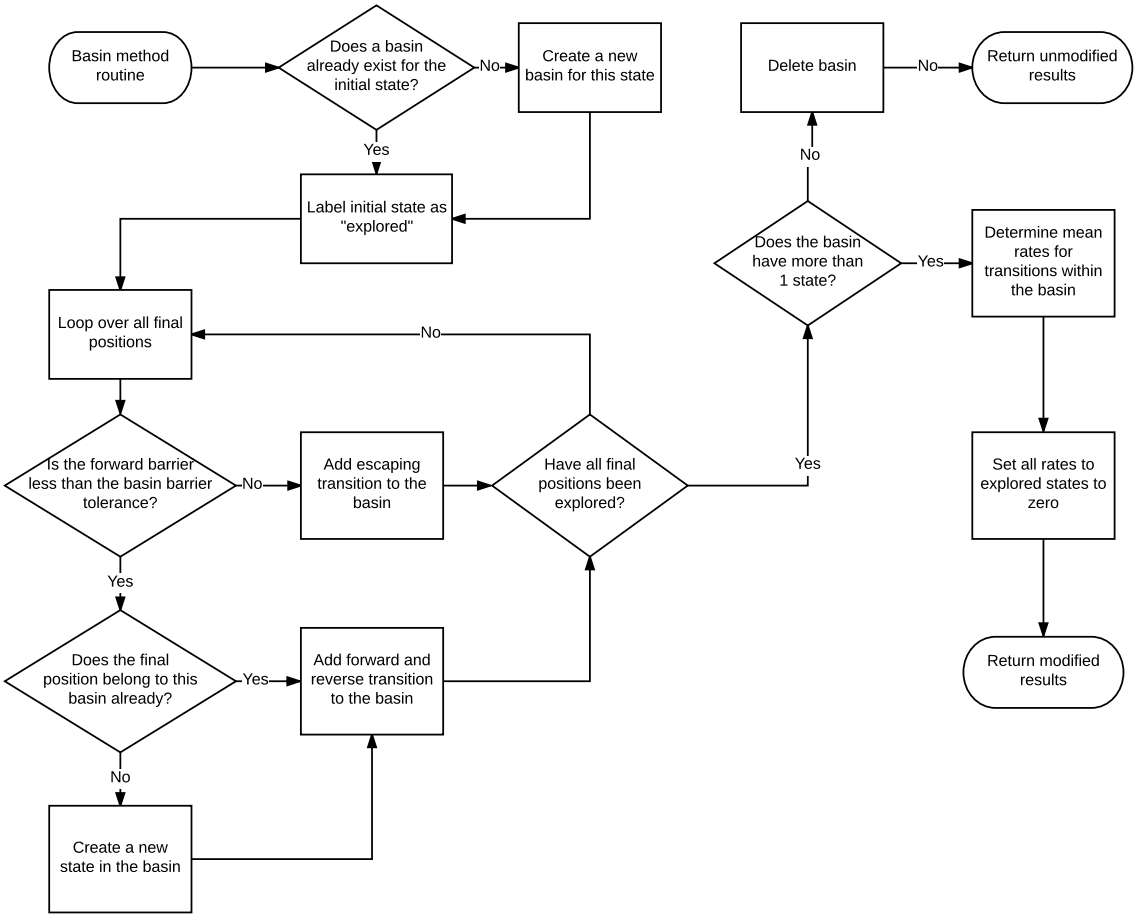

Figure 3.12 – Flowchart describing the process for the basin method within a lattice AKMC simulation.

Chapter 4

Growth Modelled Using Simplified Potentials

4.1 Methodology

To model the interaction between silver and zinc oxide using molecular dynamics simulation techniques, potential functions are required. For the Ag-O and Ag-Zn interactions, existing simple pair potentials were first used. The Ag-O interaction was modelled by the Morse potential and the Ag-Zn interaction modelled by a purely repulsive ZBL potential with parameters fitted to the Ag on ZnO work of separation [28]. The Ag-Ag interaction is modelled by the Ackland EAM type potential and the Zn-O interaction is modelled by the many-body, bond order potential: ReaxFF [55]. Both the Ag-Ag and Zn-O potentials were successfully used to model growth by Blackwell [21], for the individual systems.

The perfect ZnO $(000\bar{1})$ substrate was modelled by a cuboid of atoms, 8 layers deep (4 oxygen and 4 zinc) with 64 atoms per layer. Periodic boundary conditions were then applied in the x and z directions whilst deposition occurred normal to the $(000\bar{1})$ surface, in the y direction. Growth was simulated on the perfect O-terminated ZnO wurtzite surface by depositing single

Ag atoms and Ag dimers, with a certain kinetic energy, through running MD for 10 ps. Before each deposition event, the system is relaxed and heated to 300 K by the Berendsen thermostat acting on thermal layers. The bottom 2 layers of the lattice are fixed whilst the 4 layers above are attached to the Berendsen thermostat (Fig. 4.1).

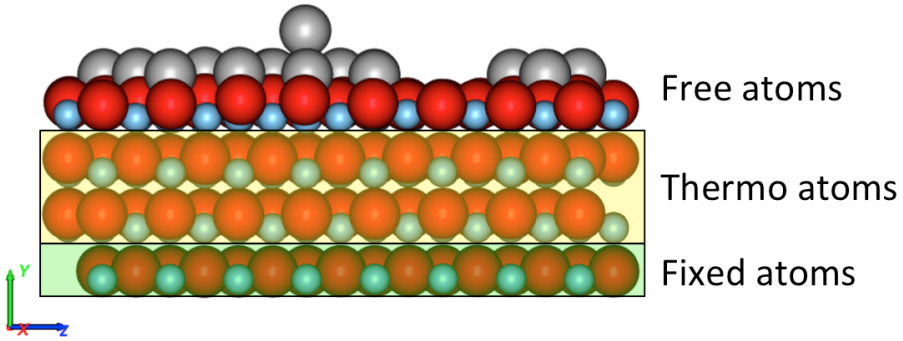

Figure 4.1 – Schematic Ag/Zn/O system depicting the distribution of fixed, "thermo" (attached to a thermostat) and free atoms.

4.2 Single Point Deposition

Prior to simulating full silver thin film growth, single point deposition simulations of Ag atoms on a ZnO surface were explored. These simulations were conducted to provide information on optimal deposition energies and were also used to help validate the potential functions used in the model. The single point depositions were simulated via Molecular Dynamics and a perfect surface was assumed before each particle interaction.

The single point deposition simulations conducted investigated two main cases: deposition of single Ag atoms and deposition of Ag dimers (both deposited normal to the ZnO surface). The depositions were simulated at room temperature ($\approx$ 300 K) and deposited at various selected points above the ZnO surface. Using the symmetry of the ZnO surface layer, a small rectangular region (that can be repeated to produce the whole surface) was examined and deposition events were simulated at 400 different (equally spaced) positions for each deposition energy. By running 400 simulations for each case, we obtain statistics on how Ag interacts with

the ZnO surface. By using this irreducible symmetry region on which to deposit Ag atoms, a good approximation of how deposited Ag atoms react over the whole ZnO surface is efficiently obtained. For the case where an Ag dimer deposition is simulated, the dimer is also randomly oriented with one atom being positioned at the same position above the surface as with the Ag monomer case.

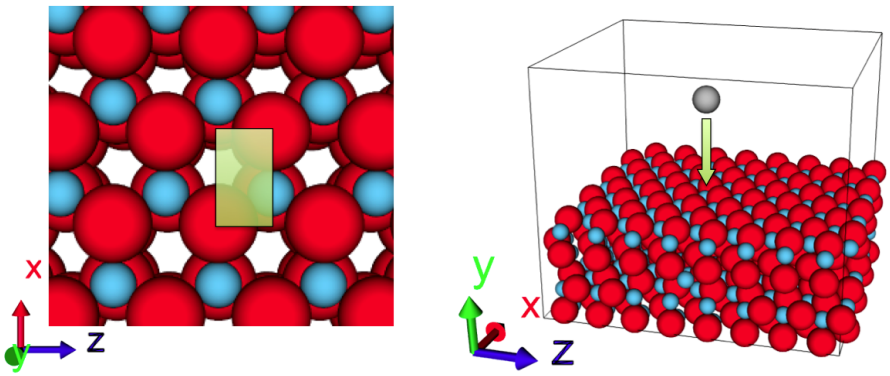

Figure 4.2 – View of the rectangular deposition region from above and a side view of an Ag monomer deposition event. Due to the periodic and symmetric properties of the ZnO surface, depositions on the rectangular region are substantial enough to predict results for the whole surface.

All depositions were simulated for 10 ps, at 400 different starting positions and at 4 different deposition energies. The deposition energies used were 0.1 eV, 1 eV, 3 eV and 10 eV. From these single deposition simulations, we were able to produce reliable statistics which can help predict optimal deposition energies for Ag growth. For low deposition energies on ZnO, single point depositions of Ag can be sufficiently categorised into four different outcomes (Fig. 4.3). For higher energy collisions, more categories may be needed to include surface deformation. The four main categories considered are:

1. **Rebound** - where deposited Ag atoms bounce off the surface and are ejected from the system.

2. **New Layer** - deposited Ag atom sits on top of the existing ZnO surface creating a new layer.

3. **Replace** - where a deposited Ag atom displaces an O atom from the surface layer and replaces it, becoming part of the surface layer. The displaced oxygen atom can be moved to another location on the ZnO slab or ejected from the system.

4. **Penetrate** - a deposited Ag atom passes through the first layer (or further) and becomes situated interstitially or replace another atom in the ZnO slab causing a deformation in the perfect crystalline structure.

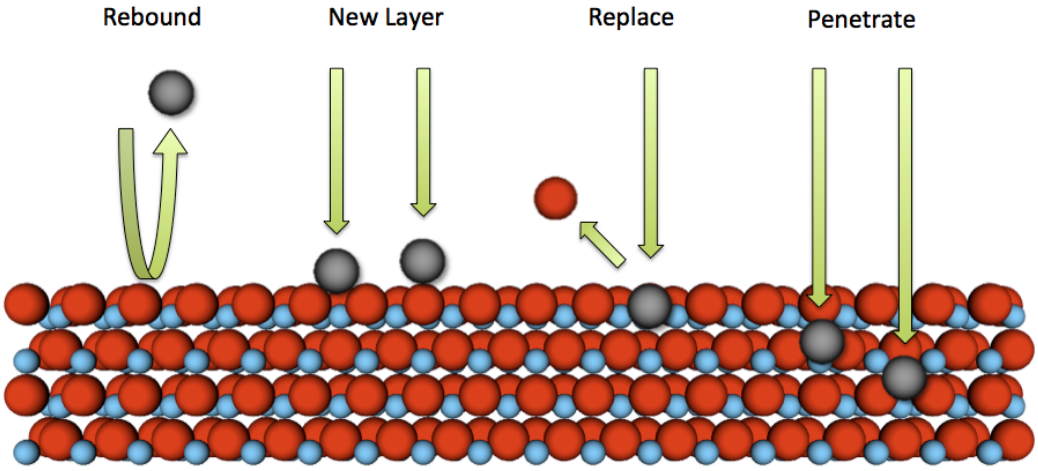

Figure 4.3 – Schematic diagram showing the 4 outcome categories when Ag is deposited on a ZnO $(000\bar{1})$ slab. Here the big grey spheres represent silver atoms, the big red spheres represent oxygen atoms whilst the smaller blue spheres represent zinc.

The results obtained by running 400 simulations for each of the 8 cases were collated (Table 4.1) and plotted (Fig. 4.4). For the single Ag atom depositions, a clear trend is visible: the higher the deposition energy, the higher the probability for the deposited atom to penetrate the surface layer. When the single silver atom is deposited with an energy of 0.1 eV, it is seen that 100% of atoms deposited form a new layer: no penetration or rebounding occurs. When the deposition energy is increased to 1 eV approximately 89% of atoms deposited form a new layer, the others penetrate. At 3 eV, 61% of deposited Ag atoms form a new layer. Again, with another increase in deposition energy, to 10 eV, we see that the majority of atoms penetrate with only 8% forming a new layer (about 0.5% replace).

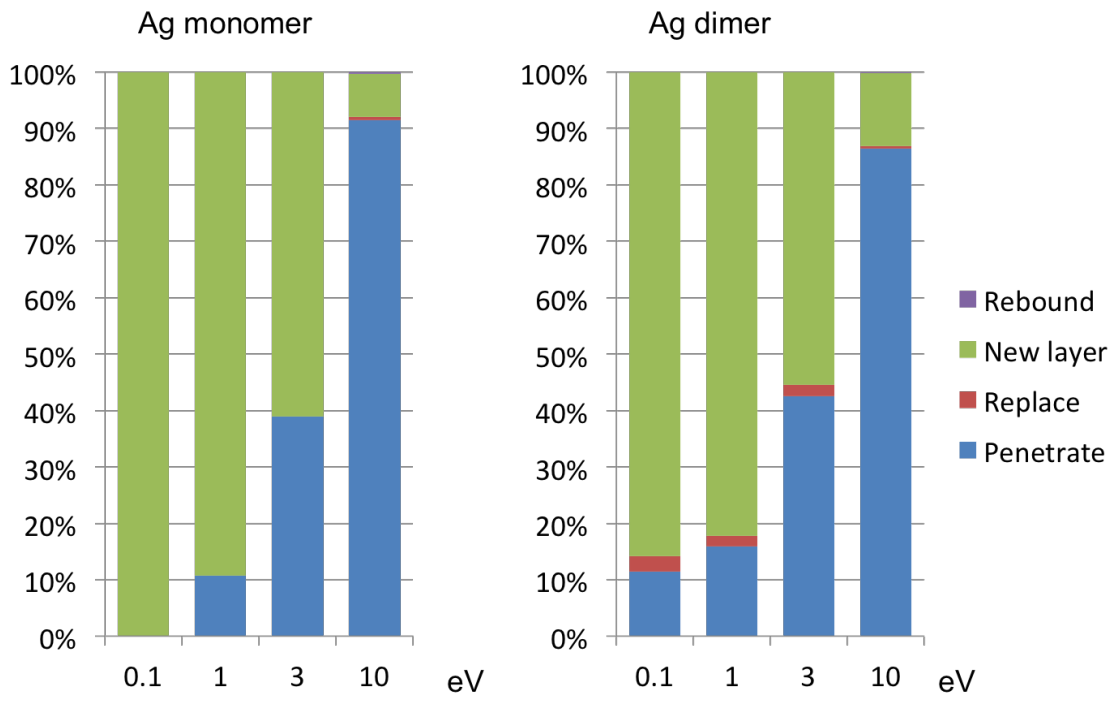

Figure 4.4 – The statistics found by running 3200 single deposition simulations. The first graph shows the results from the deposition of a single Ag atoms deposited at 4 different energies. Similarly, the second graph shows the results when Ag dimers were deposited at the same deposition energies.

For Ag dimer deposition, a similar trend of results to single Ag atom deposition at 10 eV and 3 eV is seen. Furthermore, when the deposition energy is reduced to 1 eV, we notice an increase in new layers being formed and less than 16 % of depositions resulting in penetration of the ZnO surface. Counterintuitive results occur when the deposition energy is reduced further to 0.1 eV. Here, unlike the single Ag case, around 12% of depositions result in penetration of the surface. The single Ag deposition at 0.1 eV gave 100% new layer outcomes, whereas for the Ag dimer case we see some penetration and replacing on the surface. This is because, the binding energy of Ag and oxygen is stronger than 0.1 eV. Thus, the kinetic energy of the Ag dimer increases as it approaches the surface and results in occurrences of penetration. For all deposition energies simulated, we see that rebounding does not occur for Ag dimer depositions and only happens once for the Ag monomer case (at 10 eV). For Ag atoms depositing directly onto ZnO normal to the surface, the rebound case can therefore be neglected. The replace outcome is also rare

for small deposition energies (< 1% of total simulations result in a replace outcome) but is consistently more common throughout the different simulations than the rebound (32 atoms in the simulations result in a replace outcome as opposed to only one Ag atom rebound).

Table 4.1 – Table showing results from single point Ag (monomer and dimer) depositions on the ZnO($000\bar{1}$) surface, including all 4 deposition energies investigated, with calculated standard errors for each outcome.

		Percentage (%)				Standard Error			
	Energy (eV)	0.1	1	3	10	0.1	1	3	10
Ag	Penetrate	0.00	10.75	39.00	91.50	0.00	1.55	2.44	1.40
	Replace	0.00	0.00	0.00	0.50	0.00	0.00	0.00	0.35
	New Layer	100.00	89.25	61.00	7.75	0.00	1.55	2.44	1.34
	Rebound	0.00	0.00	0.00	0.25	0.00	0.00	0.00	0.25
Ag_2	Penetrate	11.50	15.88	42.50	86.50	1.60	1.83	2.47	1.71
	Replace	2.75	1.88	2.00	0.38	0.82	0.68	0.70	0.31
	New Layer	85.75	82.25	55.50	13.00	1.75	1.91	2.49	1.68
	Rebound	0.00	0.00	0.00	0.13	0.00	0.00	0.00	0.18

The calculated standard errors indicate the reliability of the results. As 400 depositions were simulated for each case, the results have significant accuracy. The highest standard error is 2.49% (or approximately 10 out of 400) when an Ag dimer is deposited at 3 eV.

From these simulations, for best initial growth results on the ZnO surface, low deposition energies ($\leq$ 1eV) are needed. If the energy of deposited atoms is too great (i.e > 10 eV) then the probability of these atoms creating new layers on top of the surface becomes small. However, once a number of Ag atoms are on top of the ZnO and have started to form a new layer, new depositions may be less likely to penetrate and so higher energies may be considered. Growing Ag with higher energy deposition may result in a mixed ZnO/Ag structures rather than a clean interface between the two materials.

4.3 Long Time Scale Simulation

For these simulations, successive impacts are modelled followed by diffusion of atoms between impact events. After each deposition event, the system is relaxed again and transitions searches are conducted via RAT and NEB methods. Adaptive KMC dictates that at each step either a deposition or diffusion event is chosen according to their corresponding probabilities. The growth simulation then continues in this way until a set simulation time, number of steps or deposited atoms has been reached.

The adaptive KMC method relies on finding a set of possible transitions at each step. These transitions will have a range of relevant energy barriers, displacements and rates associated with them. These rates are then compared to the combined rate of all possible events to determine the probability of each single event occurring. The deposition rates considered are on average 12 monolayers per second. To put this in perspective, a transition barrier of 1 eV (on a system with temperature of 300 K) is roughly equivalent to a rate of once every 2 minutes. For growth simulations, a deposition energy of 3 eV is used.

4.3.1 Transition Testing

Before running an adaptive KMC growth simulation, certain transitions were examined. A selection of transition barriers heights (via the NEB method) and transition rates (using the Arrhenius equation) where calculated. First, testing was done with a single Ag atom on the ZnO surface. The Ag atom was locally minimised into position and hop transitions were considered. The Ag atom hops from an ABc stacking site to ABa (capital letters indicating ZnO atoms and lowercase Ag atoms) and vice versa (Fig. 4.5 (1)), with a tiny transition barrier height. A single hop transition like this takes less than a picosecond to occur at room temperature. Due to this, running whole growth simulations starting with a single Ag atom on the surface would be unfeasible using KMC. Therefore, the idea of “planting a seed” on the surface of multiple

Ag atoms before starting a simulation is considered. The seed consists of a small cluster of Ag atoms which moves only rarely. Atoms that are then deposited on the surface will eventually attach to the seed allowing the KMC simulation clock to advance without wasting a lot of computing time. The basin method could also be used to filter out small transition barriers. However, this method was only fully implemented after this work involving the simplified model was completed.

4.3.1.1 Rotation and Translation

When a single Ag atom is placed onto the ZnO surface, the atom can readily diffuse at room temperature. The smallest transition barriers (with highest rate of occurrence) calculated at each step are typically around 0.025eV (with rate $\approx 3.7 \times 10^{12}$ transitions per second) - Fig. 4.5 (1).

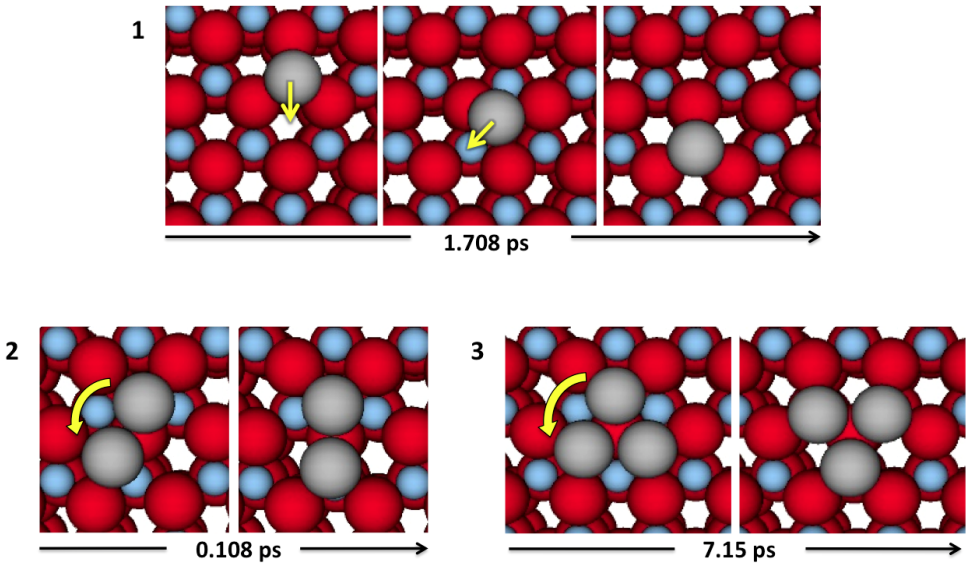

Figure 4.5 – ZnO surface (represented by large red and small blue spheres for oxygen and zinc respectively) with small silver clusters (large grey spheres) positioned above. The single Ag atom case (1) shows 2 diffusion events and the Ag atom moving readily across the surface. Case 2 and 3 depict an Ag dimer and trimer rotation transition respectively. Yellow arrows indicate direction of each transition.

When testing transitions with a silver dimer on the ZnO surface a different problem arises. The dimer rotates around an oxygen atom with even smaller energy barriers (as low as 4.5×10^{-5}eV

with corresponding rate $\approx 1 \times 10^{13}$ transitions per second) - Fig. 4.5 (2). Like with the single silver atom case, these small barriers slow the simulation down; in this case there is no net diffusion added. The Ag dimer does not diffuse as readily across the surface and so a filter could be included to cut out the unhelpful rotation transitions and only include displacements across the surface, as a way of overcoming this problem.

A similar effect is seen when considering a silver trimer (in an equilateral triangle configuration) on the surface - Fig. 4.5 (3). The trimer rotates about an oxygen atom but at a slower rate than in the dimer case. The transition barrier heights vary from 0.05 to 0.12 eV (with rotations occurring every 1-10 ps). When a trimer rotates in this way, the stacking order changes from ABc to ABa.

By running specific transition barrier height calculations using the NEB method (Fig. 4.6), it is seen that the Ag 4-mer on the ZnO can move on the surface and can change stacking order with transition barriers as little as 0.2 eV. Rotations about an oxygen atom have barrier heights of around 0.45 eV and thus are less common events. However, the cluster hop transition has a barrier height of around 0.21 eV (equivalent to 0.5 ns at 300 K).

For the growth of 12 monolayers per a second on our surface, deposition events occur on average every 0.8 ms which is equivalent to a transition barrier of height 0.6 eV. Thus, even Ag 4-mers on the ZnO are too mobile to initiate a full growth simulation. Thus, the 6-mer and 8-mer were investigated for feasible transitions and their corresponding barrier heights (Fig. 4.7).

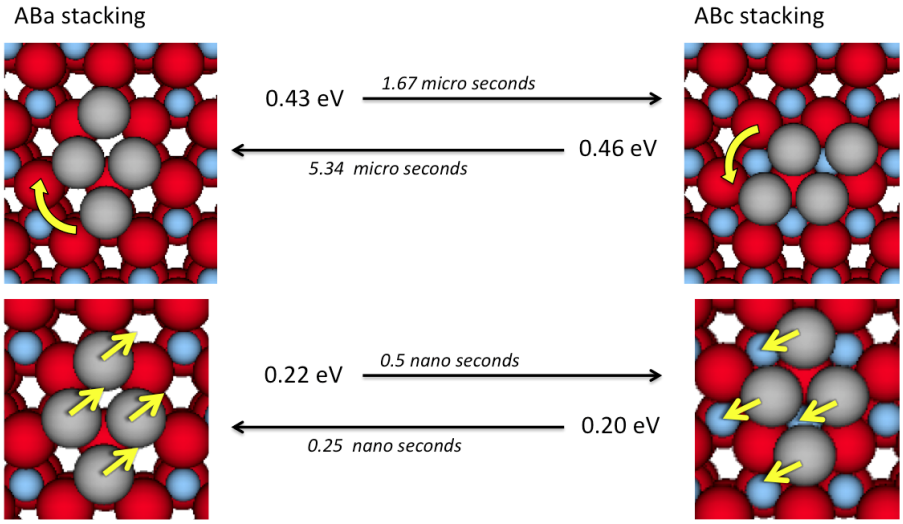

Figure 4.6 – Ag 4-mer on ZnO surface changing stacking order by rotation and hop transitions with corresponding barrier heights and calculated transition time. Yellow arrows depict direction of transition.

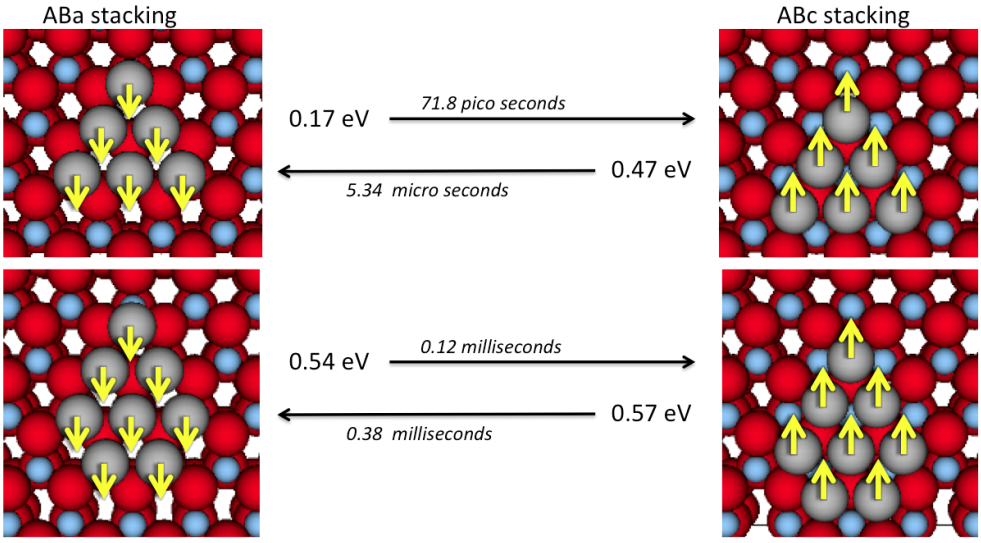

Figure 4.7 – Examples of Ag 6-mer and 8-mer transitions (changing stacking order) shown along with corresponding barrier heights and transition time. Yellow arrows depict direction of transition.

The transition examples explored show that an Ag 6-mer can still move readily across the ZnO surface (and prefers the ABc stacking order position). However, the Ag 8-mer transition example has transition times in the region of milliseconds. With the deposition rate being around once every 0.8 ms, the Ag 8-mer is used as a seed to initiate growth simulations.

4.3.1.2 Other Transitions

As well as considering cluster diffusion and rotation, how Ag atoms interact once they meet an existing cluster on the surface is investigated. Results suggest that additional Ag atoms will bond with existing Ag clusters with tiny energy barriers but de-bond from an existing cluster with high barriers (> 2 eV) that would not appear in AKMC simulation time scales (Fig. 4.8).

Another possible interaction considered is the ability of a single Ag atom to climb up or drop down from an existing cluster. A small cluster of 4 Ag atoms is first considered and results in barriers for one of the atoms to climb up a sit above a trimer of 0.82 eV. However, the reverse transition to drop down results in a barrier of 0.35 eV (Fig. 4.8). Literature suggests that Ag

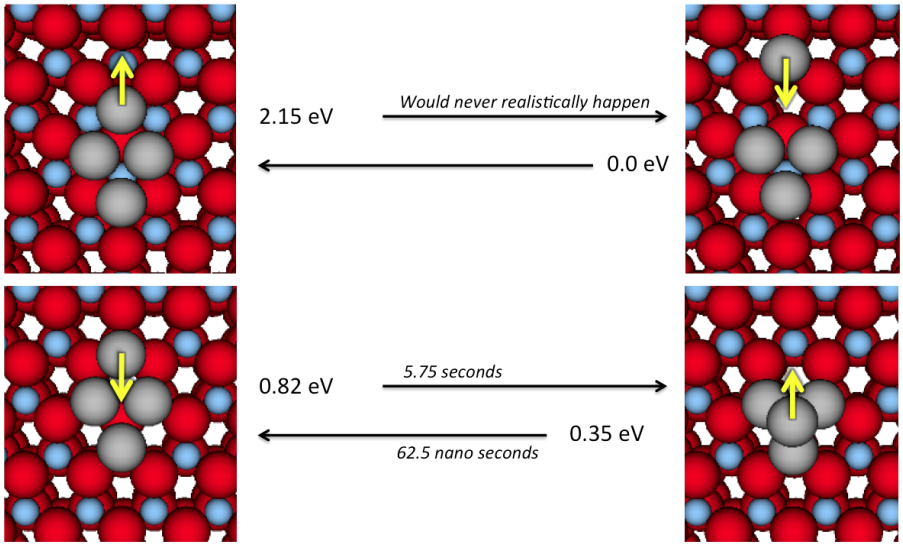

Figure 4.8 – Two transitions and transitions barrier heights are shown. The first is an example of an Ag de-bonding from an existing cluster event. The second is an example of an Ag atom climbing an existing trimer and dropping off. This climb results in further ABab stacking with the climbing Ag atom sitting directly over an oxygen atom. The drop off transition from this arrangement is reasonably high (0.35 eV) due to the Ag-O bonds in place.

has a tendency to grow on ZnO in islands rather than covering the surface in a uniform flat monolayer. A key mechanism that may influence this behaviour is a high Ehrlich-Schwoebel (E.S.) barrier. An E.S. barrier is the difference between the transition barrier height of a simple diffusion event (0.12 eV) and the height of the barrier corresponding to dropping off a step-edge transition (Fig. 4.9).

E.S. barriers were calculated with an Ag cluster positioned above an existing Ag 6-mer in different stacking orders (Fig. 4.10 and Table 4.2). The transition barriers for dropping off the clusters range from 0.38-0.67 eV. The upper value has a higher barrier height than the equivalent for a deposition event.

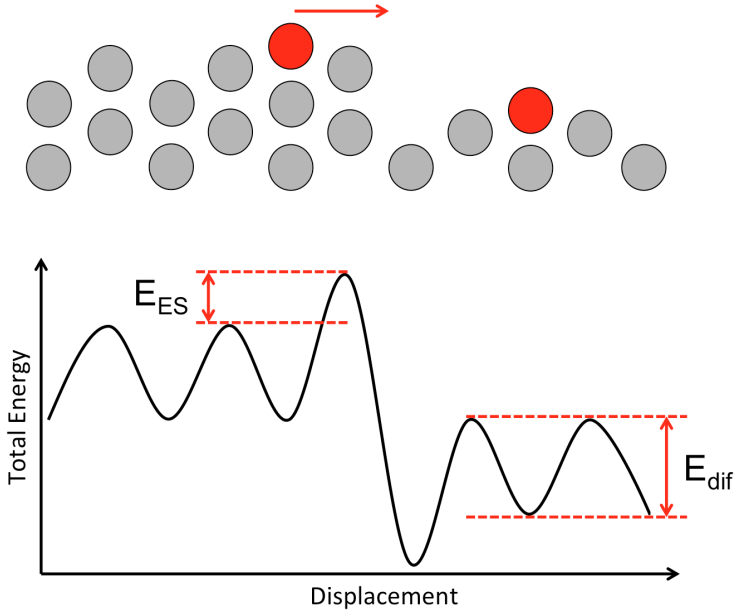

Figure 4.9 – Diagram showing the movement of an atom along a surface and the corresponding total energy graph. There is a peak when the atom drops off a step edge. The difference between the peak transition height and the normal diffusion barrier height, E_{dif}, is known as the Erhlich-Schwoebel barrier, E_{ES}.

Table 4.2 – Values corresponding to energy barrier heights, Ehrlich-Schwoebel barriers and corresponding average time for the transition to occur (at 300 K) in Fig. 4.10.

No.	Stacking Order	Barrier Height	E.S. Barrier	Trans.Time
1	ABca	0.38 eV	0.26 eV	240 ns
2	ABcb	0.53 eV	0.41 eV	80.1 μs
3	ABab	0.67 eV	0.55 eV	18 ms
4	ABac	0.40 eV	0.28 eV	0.5 μs

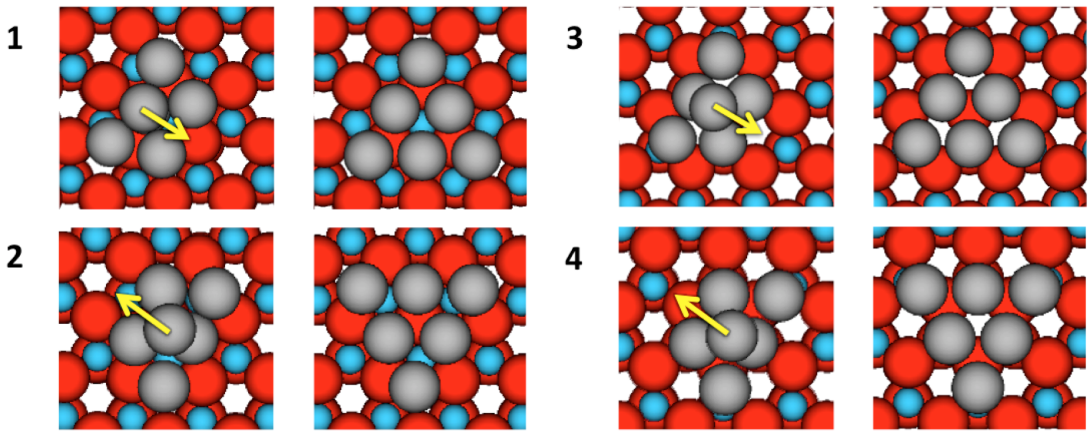

Figure 4.10 – Four cases considered when calculating Ehrlich-Schwoebel Barriers. The E.S. barriers depends on the first layer stacking order and the position of the 2nd layer Ag atom above the surface. If the second layer Ag atom is positioned above an oxygen atom in the ZnO surface layer it has a greater E.S. barrier.

4.3.2 Initial Growth

To initiate a longer simulation such as growing several monolayers of Ag on ZnO, an initial seed of 8 atoms is used in a favourable ABc stacking configuration. Initial growth results show that the Ag seed grows in size after successive deposition events to form one large cluster. However, despite starting with a cluster in ABc stacking order on the ZnO surface, different stacking orders and phase boundaries are common occurrences.

Single Ag atoms can climb onto an existing Ag layer of atoms on the ZnO surface (Fig. 4.11) or can be deposited onto with a total energy difference of < 4 eV compared to a planar cluster.

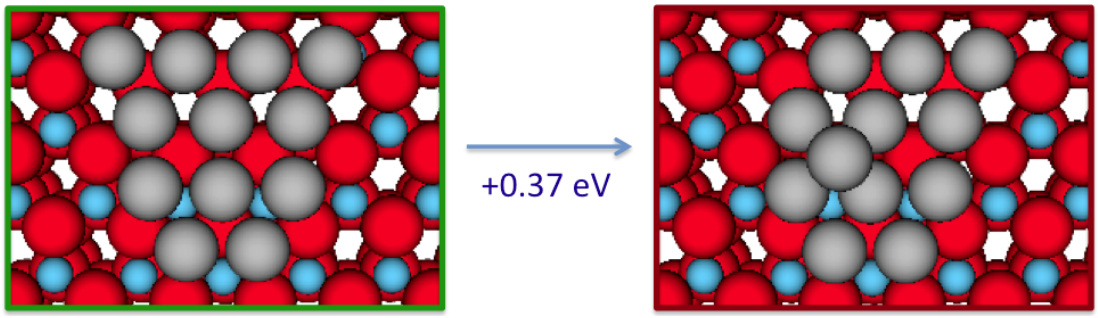

Figure 4.11 – Two formations of an Ag cluster of 12 atoms. The left hand side shows the single layer cluster with a phase boundary and two different stacking orders. The right hand side figure shows a 2 layer cluster formation with the 2 layer Ag atom in a bcc formation. The energy difference between the two cluster formations is +0.37 eV implying the flatter formation is favourable.

Once an atom is above the first layer of Ag, the drop off transition is a relatively rare event due to the large E.S. barriers mentioned in Section 4.3.1.2.

Along with deposition events at 3 eV potentially leading to penetrating atoms, Ag atoms can be pushed into the ZnO surface by surrounding atoms. Fig. 4.12 shows an occurrence of an Ag atom being forced into the ZnO surface by surrounding Ag atoms. This transition can occur in our simulations as the energy for Ag atoms to reside in the subsurface is less than that of adsorbed Ag atoms on the surface for this model. A single atom example of subsurface versus above surface configurations is investigated (Fig. 4.13) and shows a 0.75 eV preference for Ag to reside subsurface.

This result was contrary to the *ab initio* calculations performed in chapter 5 and was a major reason why more detailed calculations were not performed using the simplified model.

By continuing growth simulations it becomes clear that the Ag and ZnO interfaces are not completely separate layers. In some simulations, up to 20% of deposited Ag atoms locate subsurface. Of this 20%, around 2% of penetrating atoms are due to post deposition diffusion events and not directly from the energy transfer during deposition (as shown in Fig. 4.12).

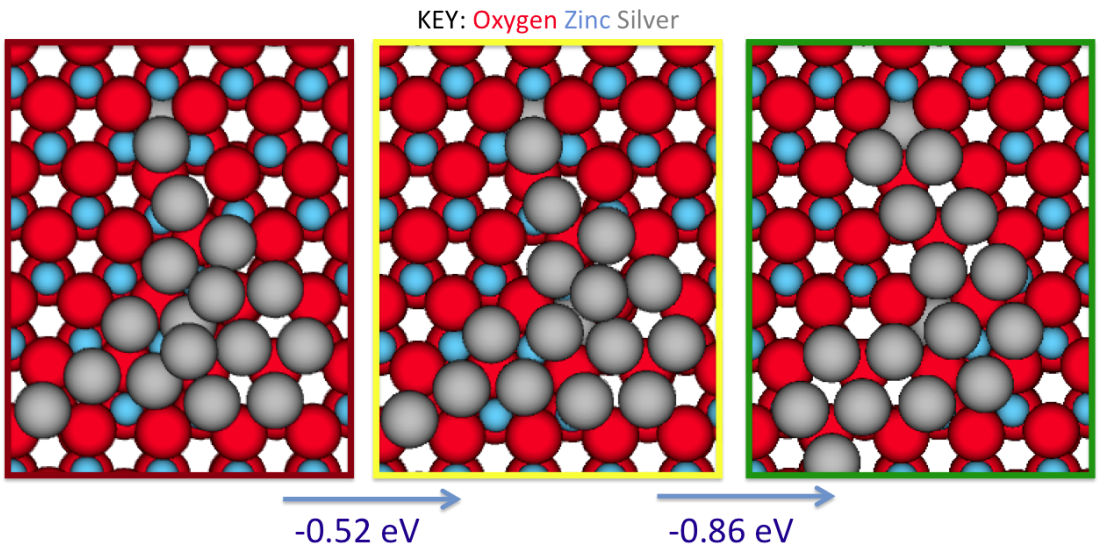

Figure 4.12 – A cluster of 15 Ag atoms on the ZnO surface shown in 3 different formations. From the left to the right, the 2 Ag atoms on the second layer push an Ag atom into the ZnO surface (this is energetically favourable by 0.52 eV) finally reordering into a mostly ABa stacking order formation.

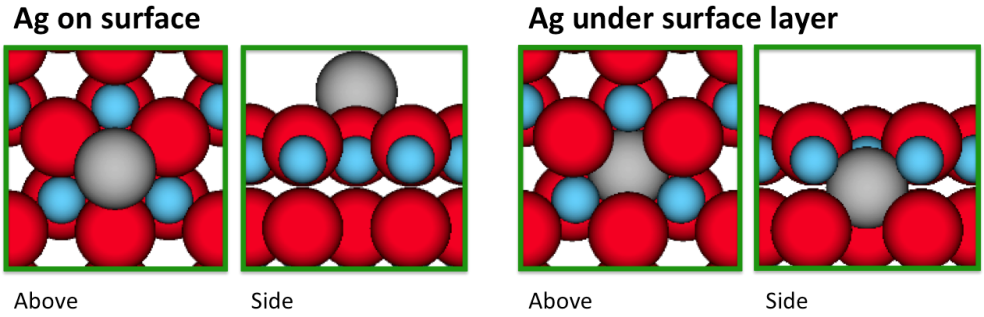

Figure 4.13 – A single Ag atom is relaxed either above the ZnO surface or under the surface layer. Here, the latter case is energetically favourable (with total energy difference between the two cases of 0.75 eV) so, along with high probability of penetration from depositions events, it would seem likely that Ag atoms will sit under or in the surface layer meaning that the Ag and ZnO layers will not be completely separate.

After 50 ms of growth simulation with deposition energies of 3 eV, around half a monolayer has been deposited onto the ZnO surface (Fig. 4.14). The majority of the deposited atoms lie on the surface and several phase boundaries are visible. The phase boundaries mean that the large cluster of Ag atoms is not sat in a single ABa or ABc stacking configuration but rather a mixture of the two. Some Ag ad-atoms are situated in directly above Zn surface atoms whilst neighbouring ad-atoms are situated above hollow sites. After around $0.1s$ of simulation time,

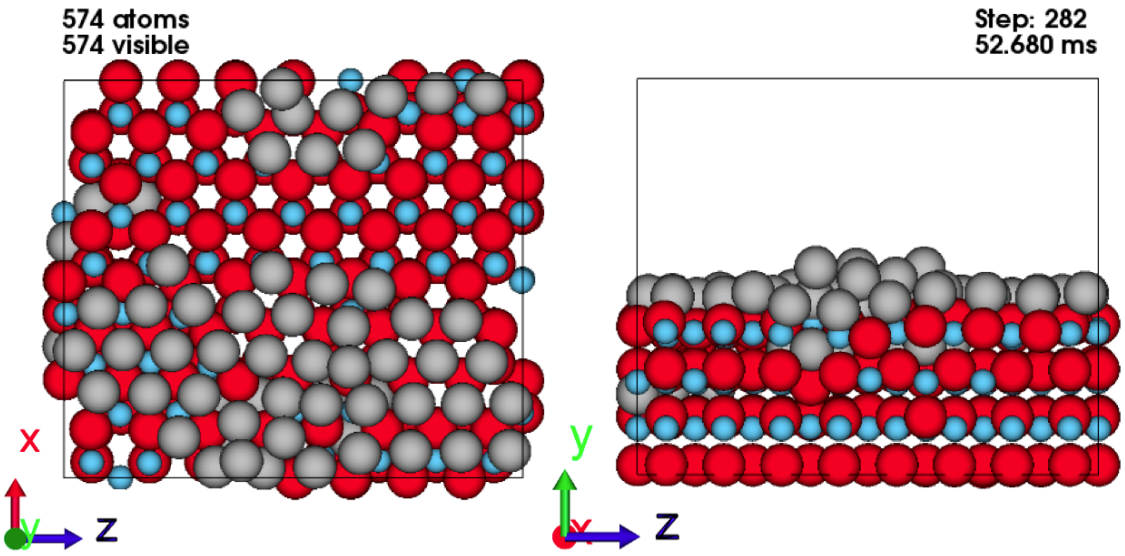

Figure 4.14 – An above and side view of 62 silver atoms (≈ 0.5 monolayer) growth on a ZnO surface. The results of simulating Ag growth with depositions energies of 3 eV and running for 52 ms simulation time.

the simulation has covered around 90% of the ZnO surface with Ag and deposited around a monolayer's worth of Ag (Fig. 4.15). The majority of Ag ad-atoms are situated in a ABa stacking formation. However, some Ag atoms are now situated above the existing Ag cluster and form a small Ag island instead of filling in the empty sites in the first Ag layer. In some places, the Ag atoms appear to be stacked up to 3 atoms high. Results from this simulation imply that the growth of an Ag thin film is not uniform. Island growth was predicted in the transition testing section after investigating high Erhlich-Schwoebel transition barriers. There is also evidence of the some initial growth of Ag growing in an ABab stacking order, i.e. continuing the ZnO structure.

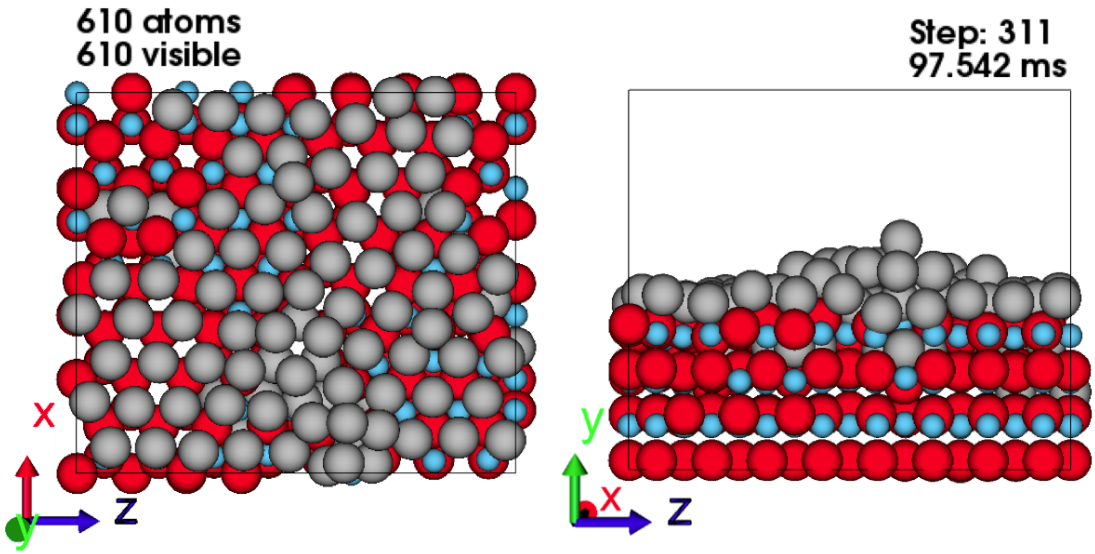

Figure 4.15 – A above and side view of 98 silver atoms growth on a ZnO surface. The results from continuing the simulation to almost a whole second of simulation time.

4.3.3 Investigation of Phase Boundaries

Phase boundaries are common in Ag growth on a ZnO surface using this model. Lin and Bristowe [4] describe that a lattice mismatch between Ag(111) and the lower ZnO(000$\bar{1}$) structure of around +11% and that a coherent (1 × 1) Ag/ZnO boundary would be difficult to produce due to high strain in the Ag layer. The affects of the lattice mismatch are investigated by taking 80 Ag atoms in a (111) formation and relaxing them on the ZnO surface.

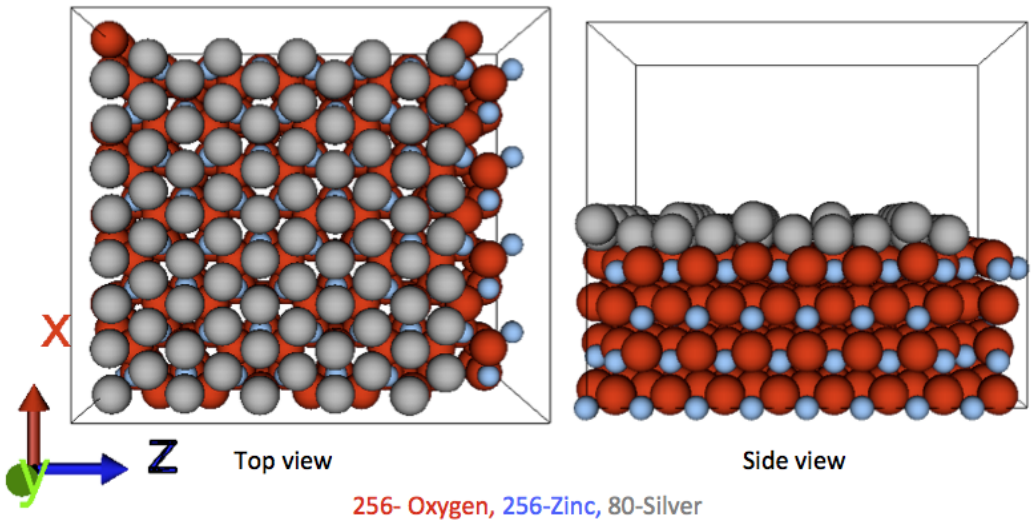

Figure 4.16 – 80 Ag atoms in (111) formation relaxed on top of the ZnO surface. From the top view, the partial Ag monolayer has retained the (111) structure however, from the side view, a rumpling effect if clearly visible.

When 80 Ag atoms in a (111) structure are relaxed on the ZnO surface, a rumpling effect in the Ag layer is produced as a mechanism to cope with the lattice mismatch (Fig. 4.16). Depending on the initial placement of the Ag monolayer on the ZnO surface, phase boundaries can also occur (Fig. 4.17). During a full growth simulation, rumpling in the first Ag layer and phase boundaries would be expected using this model. In fact, the formation of phase boundaries are visible in initial growth simulations (Fig. 4.15). The effect phase boundaries will have on further growth is yet unknown. However, the difference in energy between the systems shown in Fig. 4.16 and those in Fig. 4.17 is around 0.6 eV in favour of the latter

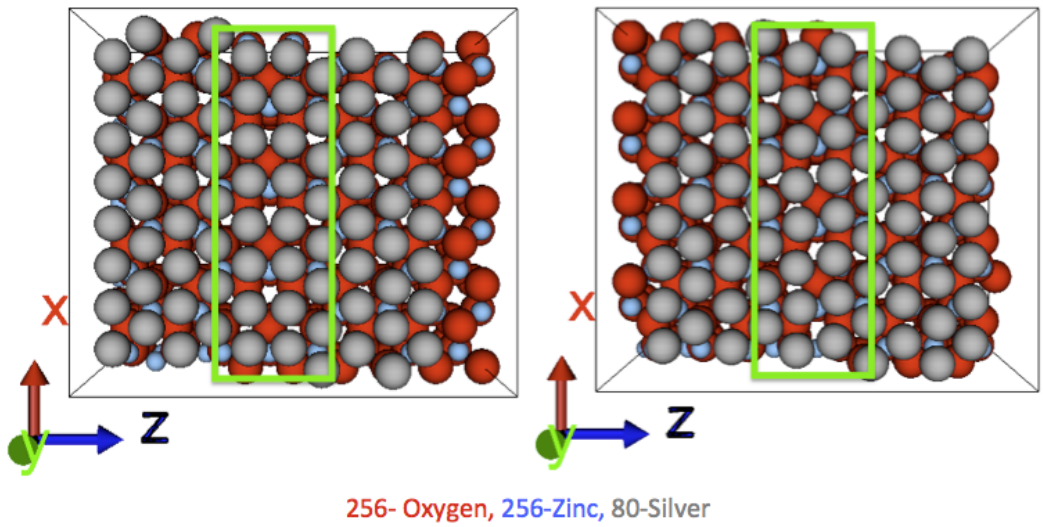

Figure 4.17 – Two different cases where 80 Ag atoms in (111) formation are relaxed on top of the ZnO surface. In these two cases, there is a rumpling effect as well as phase boundaries (highlighted in green rectangles).

suggesting that phase boundaries are an effective means of lowering the strain in the Ag layer. It may also be a growth mechanism that produces smoother surfaces.

4.4 Conclusions

MD simulations of single point deposition, using the simplified model, indicate that low energy deposition ($\leq$ 3 eV) is needed for Ag atoms to adsorb onto the polar $(000\bar{1})$ ZnO surface. Higher energy depositions result in large amounts of Ag residing subsurface. Little or no Ag was reflected off the surface even at higher energies (10 eV).

The long time scale methodology was successfully applied to investigate the initial phase of surface growth using the simplified potential model. It was shown that islands form rather than complete layers of Ag when depositing at 3 eV, typical of magnetron sputtering. However, the result that the Ag atom prefer to sit subsurface in ZnO, was in direct contrast to *ab initio*

calculations carried out using SIESTA [56] which showed the on surface site to be 1 eV more favourable. As a result, a new potential model for the Ag-O, Ag-Zn and Ag-Ag interactions was developed based on DFT results. This new model will be described in the next chapter.

Chapter 5

Development of a ReaxFF Potential for Ag/Zn/O

The model used in chapter 4 utilises existing simple pair potentials for Ag-Zn and Ag-O interactions that were fitted against works of separation values [28]. However, this model incorrectly favours interstitial Ag atoms in ZnO substrates. This results in penetrating Ag atoms at low deposition energies and diffusion transitions that push Ag ad-atoms into the ZnO surface. As the many-body potentials used for pure Ag and Zn/O interactions have successfully been used to simulate growth by Blackwell [21], a new many-body potential is considered for Ag/Zn/O interactions. Reactive force field (ReaxFF) [31] is the potential considered as it already reproduces Zn/O interactions well and consistency of potentials is favourable. Ag-O, Ag-Zn and Ag-Ag interactions are fitted to crystal and surfaces structures and included into the existing parameters set [12].

5.1 Methodology

5.1.1 Fitting ReaxFF Parameters for Ag-Zn-O Systems

Equations of state for several crystal structures and binding energies were calculated by DFT using the SIESTA program [57] with the help of our collaborators from the University of Mons, Belgium. To add Ag into the existing ZnO parameter set, Ag, Ag-Zn and Ag-O structures were examined. Cohesive energies were calculated for these lattices when undergoing uniform expansion and some selected distortions. By using both expanded and distorted lattice configurations in the fitting procedure, bond distances and valence angle energies can be determined.

First, a mixture of real and fictitious crystal structures are examined. Simple cubic (SC), body centred cubic (BCC), face centred cubic (FCC) and hexagonal closed packed (HCP) structures for Ag were considered and compared to experimental data for the real FCC structure. To fit parameters for Ag-Zn interactions, three different atomic ratios were used in simple BCC and FCC structures of which the AgZn crystal in a BCC configuration is seen experimentally. Ag_2O was considered in its natural cuprite crystal formation and is compared to other high symmetry AgO structures that are not seen in nature so as not to overestimate the stability of other oxidation states (Fig. 5.1).

Additionally, adsorption energies were calculated for Ag atoms positioned on a polar $(000\bar{1})$ and non polar $(10\bar{1}0)$ ZnO surface, see Figure 5.2. The structures considered incorporated single Ag ad-atoms as well as Ag dimers and trimers positioned in various configurations on the surface. A range of these structures were used for the ReaxFF fitting procedure to help describe diffusion across the surface and find favourable adsorption sites. Subsurface Ag atoms were also considered when fitting the ReaxFF parameters to describe better the stability of Ag interstitials.

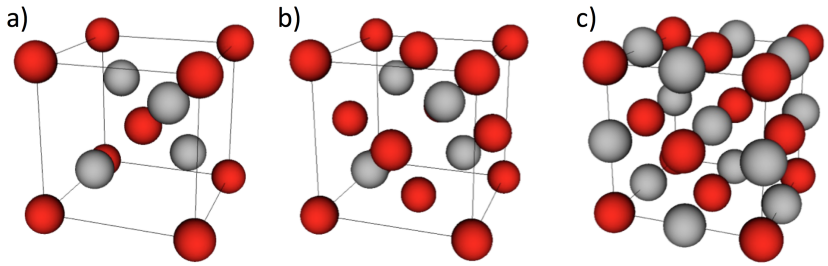

Figure 5.1 – The three crystal structures used within the fitting of Ag/O parameters: a) Ag_2O cuprite, b) AgO sphalerite and c) AgO rocksalt. Here red and grey spheres represent O and Ag atoms respectively.

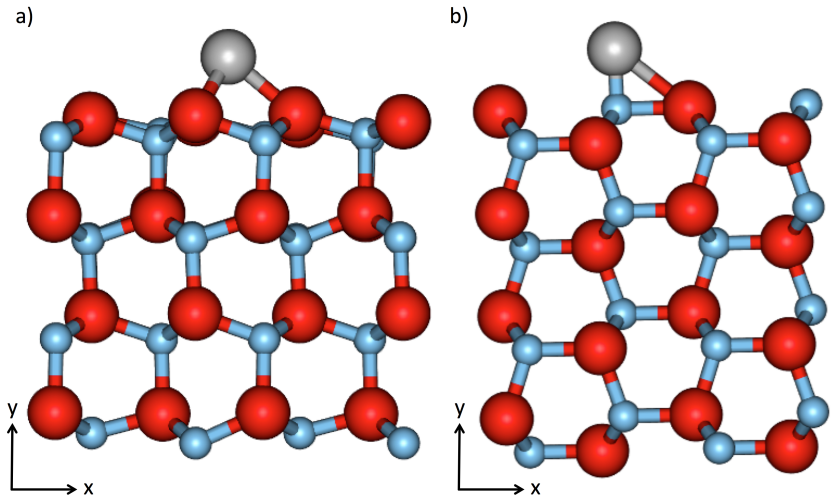

Figure 5.2 – A schematic showing a single Ag ad-atom on the (a) - polar $(000\bar{1})$ and (b) - non polar $(10\bar{1}0)$ oriented ZnO wurtzite structure. Here, grey, red and blue spheres represent Ag, O and Zn atoms respectively.

Together with fixed parameters from the existing ZnO ReaxFF potential [33], the new parameter set was fitted by minimising the error:

$$\text{Error} = \sum_{i=1}^{n} \left[\frac{x_{i,DFT} - x_{i,RxFF}}{\sigma_i} \right]^2 \tag{5.1}$$

described by van Duin *et al.* [58]. In Eq. 5.1, $x_{i,DFT}$ and $x_{i,RxFF}$ are the DFT and calculated values respectively. The parameter σ_i corresponds to the weighting of data point i. Initial parameters were taken from the ReaxFF description of Cu/O/H [59] and then optimised against the DFT data for Ag/Zn/O interactions.

5.1.2 Computational Details

The quantum-chemical calculations have been performed using Density Functional Theory [60] through the SIESTA [57] package. SIESTA is a numerical basis pseudopotential code which was the package of choice for our collaborators. The choice of settings and inputs for the code where influenced by previous work by Cornil *et al.* [61]. The treatment of exchange-correlation was done with the Perdew-Burke-Ernzerhof functional [62]. Valence electrons were described using a numerical DZP (double-zeta polarised) atomic basis set while Trouillier-Martins pseudopotentials were used for the description of the nuclei and core electrons [63]. Periodic boundary conditions were applied along the three directions of the space with dipolar corrections along the z-axis to cancel self-interaction between the cells. Equations of state for the smaller Ag and Ag-Zn crystal structures were sampled with a $12 \times 12 \times 12$ k-point sampling mesh of the Monkhorst-Pack type to compute the electronic structure in the Brillouin zone [64] with a mesh cutoff of 300 Ry. The slightly larger Ag-O crystal structures required a $8 \times 8 \times 8$ k-point sampling mesh with a larger cutoff of 600 Ry to match convergence. DFT calculations performed on the polar ZnO structure used a method of passivation of the Zn terminated face. This passivation was made by adsorption of OH on the Zn-terminated face.

For the ZnO surface, both the polar $(000\bar{1})$ and the non-polar $(10\bar{1}0)$ faces were considered with a similar surface per unit cell i.e. 9.75×11.26 Å for $(000\bar{1})$ and 10.40×9.74 Å for $(10\bar{1}0)$. Previous work has shown surface reconstruction due to the dipole moment however in our model the bottom Zn-terminated layer for the polar ZnO was passivated as in [61] and [65]. Here, a $3 \times 3 \times 1$ Monkhorst-Pack k-point grid was used with a slightly smaller, yet well converged, mesh cutoff of 250 Ry to reduce computation time. The relaxation of the silver atom and the two top ZnO layers were performed using the conjugate gradient method [66] until the forces acting on atoms were less than 0.04 eV/Å while the bottom layers were fixed in their bulk position.

The binding energy of the Ag atom on the ZnO surface was calculated using the expression:

$$E_{Bind} = [E_{Ag/ZnO} - E_{slab}^{ZnO} - n \cdot E_{bulk}^{Ag}]/n \tag{5.2}$$

where $E_{Ag/ZnO}$ is the total energy of the relaxed Ag/ZnO surface, E_{slab}^{ZnO} the total energy of the relaxed ZnO surface and E_{bulk}^{Ag} the total energy of a single silver atom in bulk FCC conditions, see Table 5.1.

5.2 Results and Discussion

The objective for this fitted parameter set is to reproduce equations of state (EoS) for a number of crystal structures and give binding energies for different surface structures with reasonable accuracy.

5.2.1 Equations of State

Uniform Crystal Expansion

For this parameter set to be successful at modelling the surface interaction and growth, DFT and ReaxFF must exhibit a good agreement for cohesive energies and lattice constants. Table 5.1 shows that the ReaxFF is fitted well to these conditions and is also in good agreement with experimental data for available structures. The largest error occurs for the AgO rocksalt polymorph with a cohesive energy difference between DFT and ReaxFF at equilibrium of 13%.

As shown in Fig 5.3, ReaxFF reproduces very well the equations of state found by DFT. Cohesive energies match for nearly all structures considered. For the pure Ag crystal structures, the energetically favourable configurations fit almost perfectly to the DFT data. The curve for the simple cubic structure is poorly matched but is very high in energy - as such, this disagreement is believed to be acceptable since it will not impact growth simulations. Note

Table 5.1 – Comparison of lattice parameters (a and c) and cohesive energies (E_{Coh}) from DFT, ReaxFF and experimental results where available for Ag/Zn/O structures. (Experimental results were taken for AgZn at room temperature, Ag_2O at 40 K and Ag FCC at room temperature and 0 K for lattice constant and cohesive energy respectively.)

Structure	Property	DFT	ReaxFF	Exp
Ag SC	a/Å	2.78	2.97	
	E_{Coh}/eV	-2.53	-2.45	
Ag FCC	a/Å	4.19	4.22	4.09 [3]
	E_{Coh}/eV	-2.91	-3.04	-2.95 [3]
Ag BCC	a/Å	3.33	3.33	
	E_{Coh}/eV	-2.90	-3.00	
Ag HCP	a/Å	2.97	3.00	
	c/Å	4.83	4.89	
	E_{Coh}/eV	-2.90	-3.04	
Ag_3Zn FCC	a/Å	4.11	4.12	
	E_{Coh}/eV	-2.63	-2.77	
AgZn BCC	a/Å	3.20	3.22	3.16 [67]
	E_{Coh}/eV	-2.36	-2.39	
$AgZn_3$ FCC	a/Å	3.98	3.96	
	E_{Coh}/eV	-2.02	-1.99	
Ag_2O Cuprite	a/Å	4.85	4.87	4.75 [68]
	E_{Coh}/eV	-3.78	-3.76	
AgO Rocksalt	a/Å	4.70	4.69	
	E_{Coh}/eV	-4.09	-4.62	
AgO Sphalerite	a/Å	5.10	5.08	
	E_{Coh}/eV	-3.88	-3.91	

that for the HCP structure, the c/a ratio was kept constant at 1.63. Cohesive energies for all three Ag-Zn alloy structures, are also consistent with the DFT data. For silver oxides, the favourable AgO rocksalt is made more stable whilst AgO sphalerite and Ag_2O cuprite remain similar when comparing the ReaxFF and DFT data. The one slight concern here is the over stability of the rocksalt polymorph and the deviation in the curve though this does not change the relative stability of the three phases. Reducing the stability of the rocksalt polymorph would be at the expense of more accurate surface results.

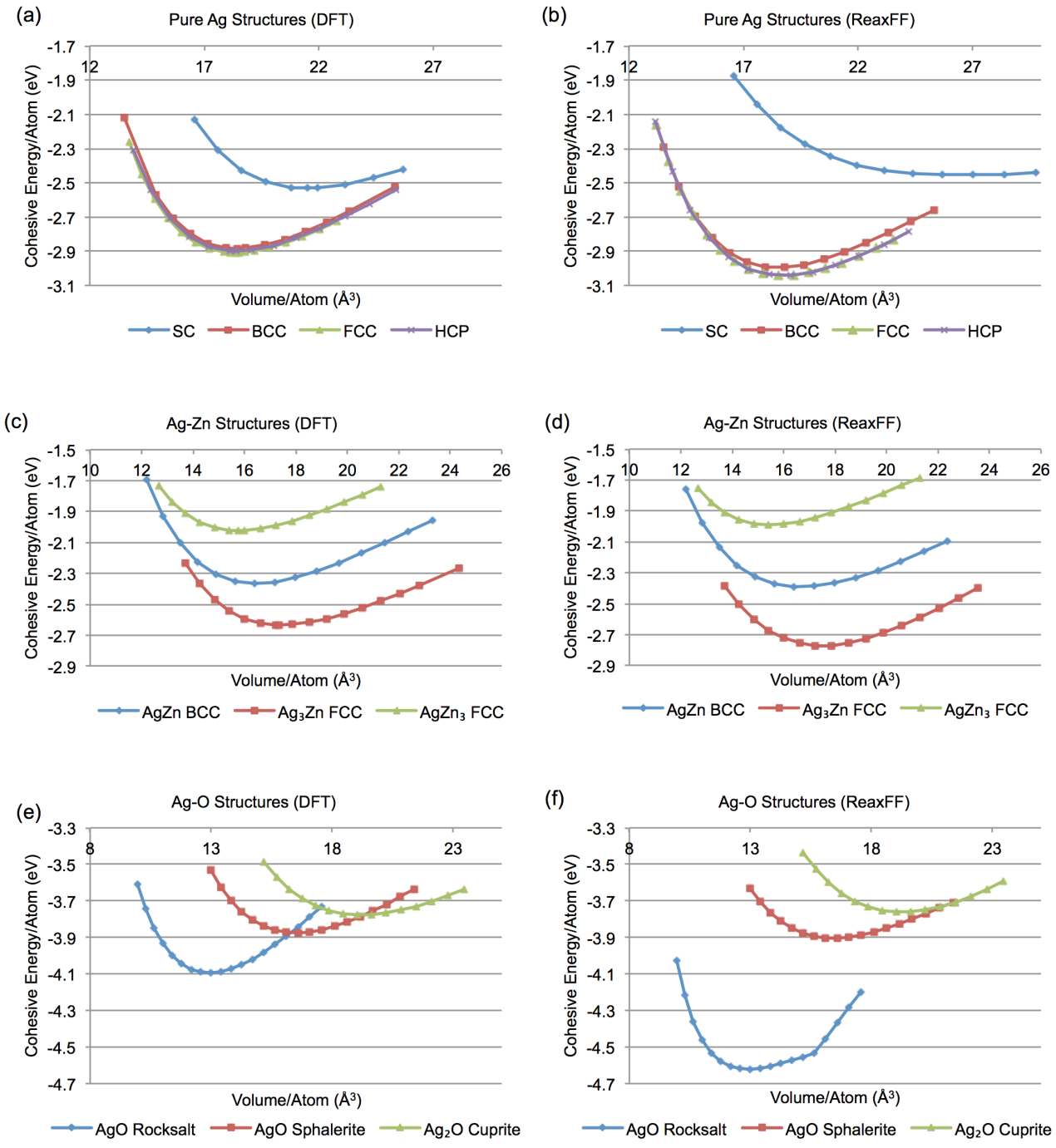

Figure 5.3 – Equations of state for silver, (a) and (b), silver-zinc, (c) and (d), and silver-oxygen, (e) and (f), crystal structures when undergoing uniform expansion. The plots (a), (c) and (e) show the equations of states as calculated via DFT. The plots (b), (d) and (f) show the equations of state as calculated via ReaxFF for comparison.

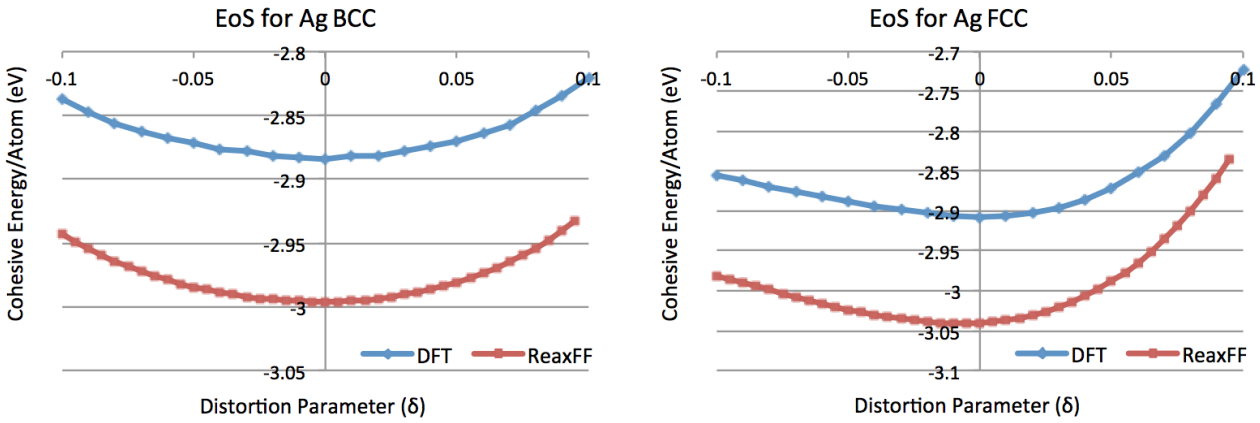

Figure 5.4 – Comparison of equations of state (EoS) via DFT and ReaxFF for pure silver crystal structures undergoing distortion.

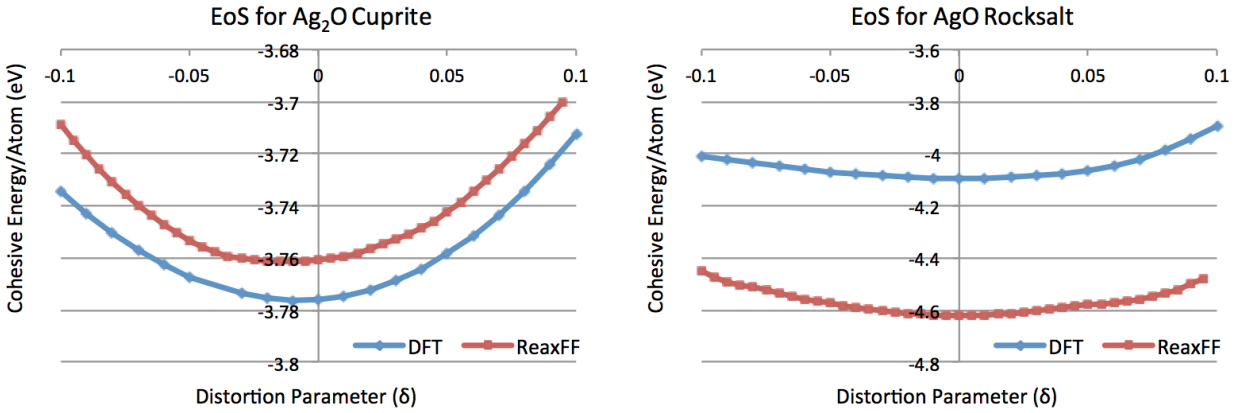

Figure 5.5 – Comparison of equations of state (EoS) via DFT and ReaxFF for Ag-O crystal structures undergoing distortion.

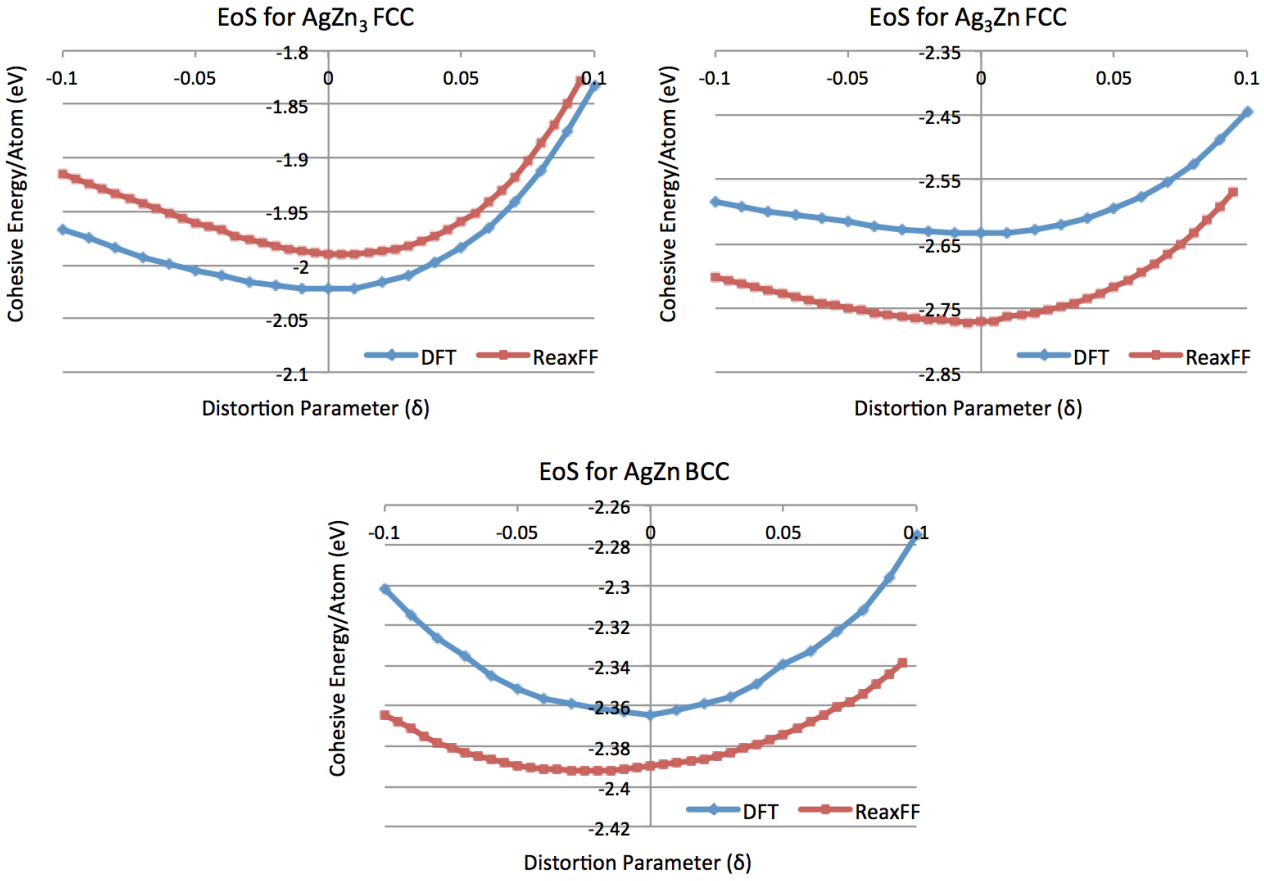

Figure 5.6 – Comparison of equations of state (EoS) via DFT and ReaxFF for Ag-Zn crystal structures undergoing distortion.

Distorted Crystal Expansion

Equations of state were also compared for a selection of distorted lattice structures, namely for pure Ag in FCC and BCC structures (Fig. 5.4), AgO in rocksalt and Ag_2O in a cuprite structure (Fig. 5.5), AgZn in BCC, Ag_3Zn and $AgZn_3$ in FCC (Fig. 5.6). The equilibrium lattice parameters found during the uniform expansion calculations were multiplied by 1-δ in 2 directions and by 1+δ in the other direction. Here, δ is the distortion parameter with values varying from -0.1 to 0.1.

The curves produced by plotting the data for distorted ReaxFF and DFT crystal structure data agree well. The shape of the curves match and the cohesive energy values agree with the exception of AgO rocksalt. As with the uniform expansion case, the stability AgO rocksalt is overestimated by 0.5 eV at the expense of improved surface binding energies.

5.2.2 Binding Energies

An important task for the ReaxFF parameter set is to recreate binding energies and bonding sites for small silver clusters on and just below the ZnO polar and non-polar surfaces. DFT results are compared to ReaxFF (Fig. 5.7) and show a relatively high binding energy for Ag on the polar ZnO surface, implying that a high proportion of Ag atoms will stick to the surface after deposition rather than reflect. However, this seems less likely for the non-polar surface in view of the lower binding energies. Thus, accurate adsorption energies are needed for reliable single point deposition statistics. After deposition events, diffusion of Ag across the surface has to then be considered. Hence, energy differences between different adsorption sites and positions for Ag atoms must be consistent with the DFT results.

In general, the ReaxFF potential reproduces the binding energies of Ag on the polar and non-polar ZnO surface calculated via DFT well. However, there is a slight tendency for the potential to underestimate the magnitude of the binding energy for the majority of the

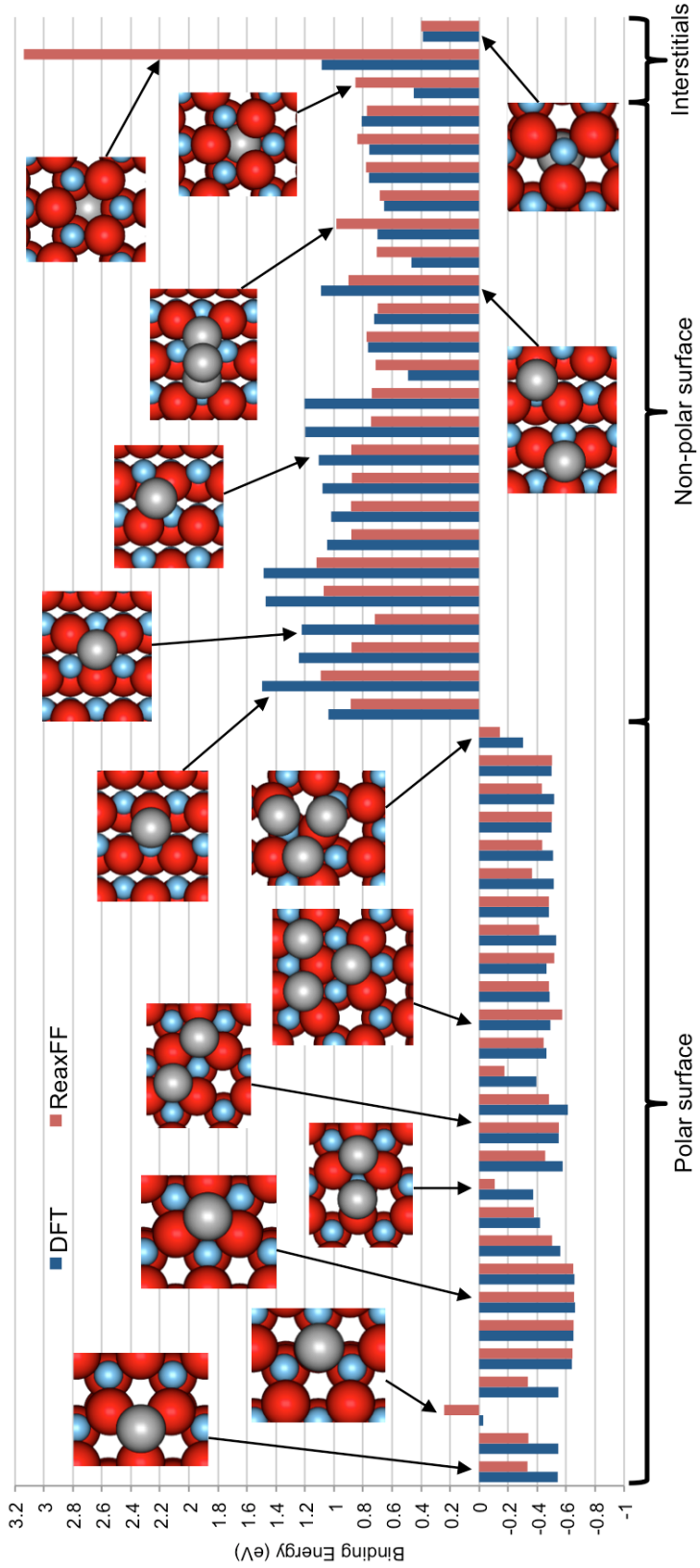

Figure 5.7 – A comparison of the binding energies calculated from DFT and ReaxFF for all structures used in the fitting procedure. Example structures are shown alongside their corresponding calculated binding energies. The fitted potential captures the trends in binding energies well.

structures with the exception of one of the interstitial structures. In Fig.5.7, structures are categorised into polar surface and non-polar surface to indicate the ZnO surface orientation and 3 structures including subsurface Ag atoms on a polar ZnO substrate are labeled as interstitials. The least favourable interstitial structure describes an Ag atom positioned ∼4 Å deep into the ZnO surface between O and Zn layers. The structure is energetically unfavourable when calculated via ReaxFF compared to other structures examined. However, this is not a concern when simulating low energy deposition simulations as this structure is highly unlikely to occur. The other two interstitial cases describe an Ag atom situated below the first O and Zn layer in a hollow site and below a Zn atom. It is also worth noting that both the DFT and ReaxFF results indicate that it is energetically favourable for Ag adatoms to be dispersed separately across the polar surface. In contrast, Ag prefers to form clusters on the non-polar surface.

5.2.3 Work of Separation

In order to test the potential further, the work of separation of the Ag-ZnO interface was calculated and compared to previous DFT calculations from the literature [4]. A coherent (1×1) Ag(111)/ZnO(000$\bar{1}$) interface was considered. To achieve the coherent interface, the Ag lattice was stretched laterally to match the lattice constant of ZnO. 6 layers of Ag (111) positioned above 4 double layers of ZnO(000$\bar{1}$) in three high symmetry adsorption sites, see Fig. 5.9, were considered with a surface area, A, of 600 Å^2. The outermost 2 layers of silver and 2 double layers of ZnO were fixed, such that the interface spacing was optimal, then atoms near the interface were relaxed (Fig. 5.8). Works of separation, W_{sep}, were then calculated via

$$W_{sep} = (E^{Ag}_{slab} + E^{ZnO}_{slab} - E_{Ag/ZnO})/A. \tag{5.3}$$

and compared to DFT values, see Table 5.2. In Eq. 5.3, $E_{Ag/ZnO}$ is the total energy of the relaxed structure whilst E^{Ag}_{slab} and E^{ZnO}_{slab} represent the energy of the isolated relaxed structures of the pure Ag and ZnO slabs respectively. Despite the ReaxFF parameter set not being fitted

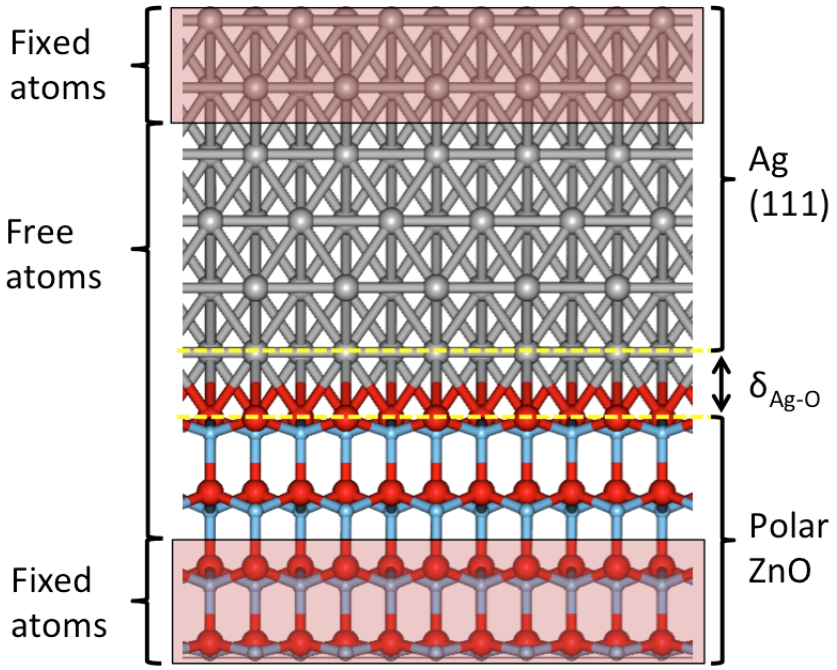

Figure 5.8 – Schematic of the structure used to calculated work of separation between a coherent (1 × 1) Ag and ZnO (000$\bar{1}$) interface. Areas highlighted in pink contain fixed atoms whilst all other atoms are free. Here δ_{Ag-O} denotes the distance between the Ag and ZnO interfaces.

to works of separation, Table 5.2 shows a very good agreement between ReaxFF and the DFT values from the literature.

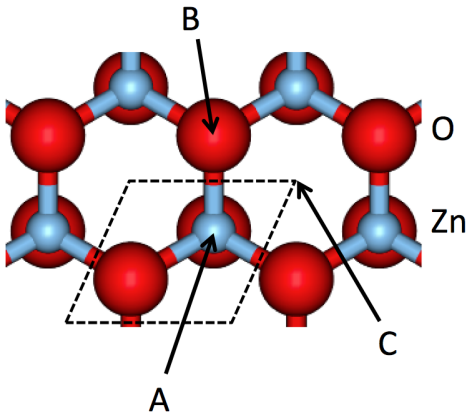

Figure 5.9 – The high symmetry adsorption sites on the (000$\bar{1}$) ZnO surface considered when calculating W_{sep}.

Table 5.2 – Works of Separation, W_{sep} and interlayer spacing (δ_{Ag-O}) calculated for the (1×1) coherent Ag/ZnO interface. The Ag slab was positioned in 3 different adsorption sites then near interface atoms were relaxed. DFT values found by Lin and Bristowe [4] are in brackets.

Adsorption site	W_{sep} (J/m^2)	δ_{Ag-O} (Å)
A	0.68 (0.74)	2.41 (2.31)
B	1.44 (1.40)	2.30 (2.30)
C	0.67 (0.83)	2.40 (2.14)

5.3 Application: Single Point Depositions

As a precursor to considering how Ag grows on the ZnO surface, the interaction of Ag atoms and Ag_2 dimers with a ZnO surface was investigated. A study into how Ag deposits onto a ZnO substrate at different depositions energies (ranging from 0.1 to 30 eV) has been carried out via MD simulations. The simulation cells used for the polar and non-polar ZnO surfaces were of similar volume, namely 22.80 × 26.33 × 30 Å (with 512 atoms) for ZnO $(000\bar{1})$ and 26.51 × 26.33 × 30 Å (with 640 atoms) for ZnO $(10\bar{1}0)$. Ag atoms were deposited normal to the surface over the regions shown in Fig. 5.10. Each Ag atom is initially placed over 10 Å above the surface outside of the ReaxFF cutoff. Here, a sample of 400 separate simulations have been run for each of the 5 deposition energies with the initial atom or dimer placed above the surface. For Ag_2 dimer deposition, the dimer is randomly orientated before deposition is undertaken. In a typical Ag deposition event, a single Ag atom gains a charge of 0.6 $|e|$ as it approaches the polar ZnO surface. This charge transfer promotes Ag-O bonding on the polar surface.

The results shown in Tables 5.3, 5.4, 5.5 and 5.6 have been categorised into 3 different outcomes: namely adsorb, penetrate and reflect (Fig. 4.3). These labels are sufficient to describe low energy impacts of Ag onto the ZnO. The term split in tables 5.4 and 5.6 refers to the case when the incoming Ag_2 dimer breaks apart on impact. However, for higher energy deposition simulations (> 30 eV), more categories may be needed to describe surface damage caused by

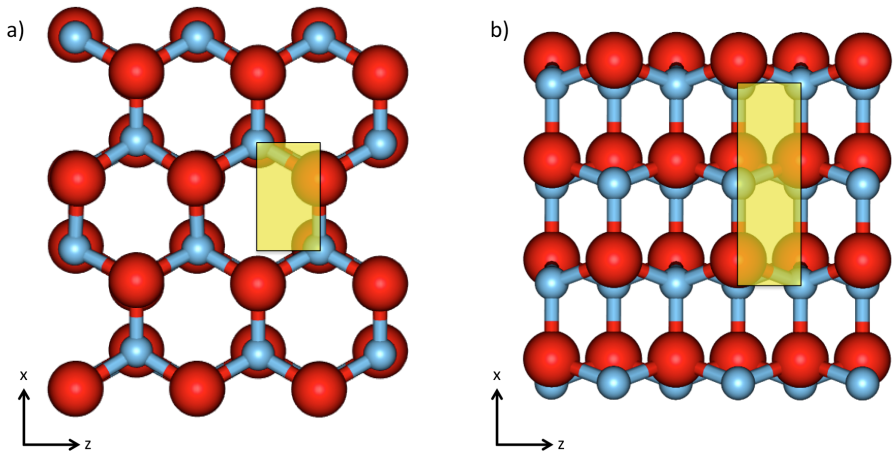

Figure 5.10 – Schematic of the irreducible symmetric zone considered for deposition of Ag on the (a) - polar and (b) - non polar ZnO surface.

Ag collisions.

5.3.1 Ag on ZnO $(000\bar{1})$

The previous calculations indicate that the polar ZnO surface is energetically favourable for Ag adsorption. For Ag monomer depositions on the polar surface, atoms penetrate only once the deposition energy reaches 30 eV. Deposition events with an energy of $\leq$ 10 eV always result in adsorption onto the surface and around 70% adsorb at energies around 30 eV (while 30% penetrate). Similar results were seen for Ag dimer depositions. It is not until deposition energies increase to around 30 eV that there were penetrating Ag atoms (in this case 92.5% of deposited atoms still adsorb to the surface). For all energies in the range considered, around one third of all dimers deposited split into 2 Ag monomers during the deposition event. Note also, no Ag atoms reflect during these deposition simulations. Fig. 5.11 shows the final resting place of the Ag atoms after impact for energies of 0.1 and 10 eV.

Table 5.3 – Single Ag deposition on ZnO $(000\bar{1})$

	Deposition Energy (eV)				
Outcome	0.1	1	3	10	30
Adsorb (%)	100	100	100	100	70
Penetrate (%)	0	0	0	0	30

Table 5.4 – Ag dimer deposition on ZnO $(000\bar{1})$

	Deposition Energy (eV)				
Outcome	0.1	1	3	10	30
Adsorb (%)	100	100	100	100	92.5
Penetrate (%)	0	0	0	0	7.5
Split (%)	32	32.5	29.5	45.5	38

5.3.2 Ag on ZnO $(10\bar{1}0)$

The other surface considered is the non-polar $(10\bar{1}0)$ orientation of ZnO. In general, the Ag binding energies on this surface are weaker than on the polar surface. Results are tabulated in Tables 5.5 and 5.6.

Table 5.5 – Single Ag deposition on ZnO $(10\bar{1}0)$

	Deposition Energy (eV)				
Outcome	0.1	1	3	10	30
Adsorb (%)	100	100	100	99.25	69.25
Penetrate (%)	0	0	0	0.25	30.75
Reflect (%)	0	0	0	0.5	0

Ag atoms start to penetrate the target surface with deposition energies of 10 eV (lower than for the polar surface). On the non-polar surface, Ag monomer and dimer depositions yield very similar results with 69% of deposited atoms resulting in adsorption at 30 eV (with the majority of other atoms penetrating the surface). For deposition energies of less than 10 eV however,

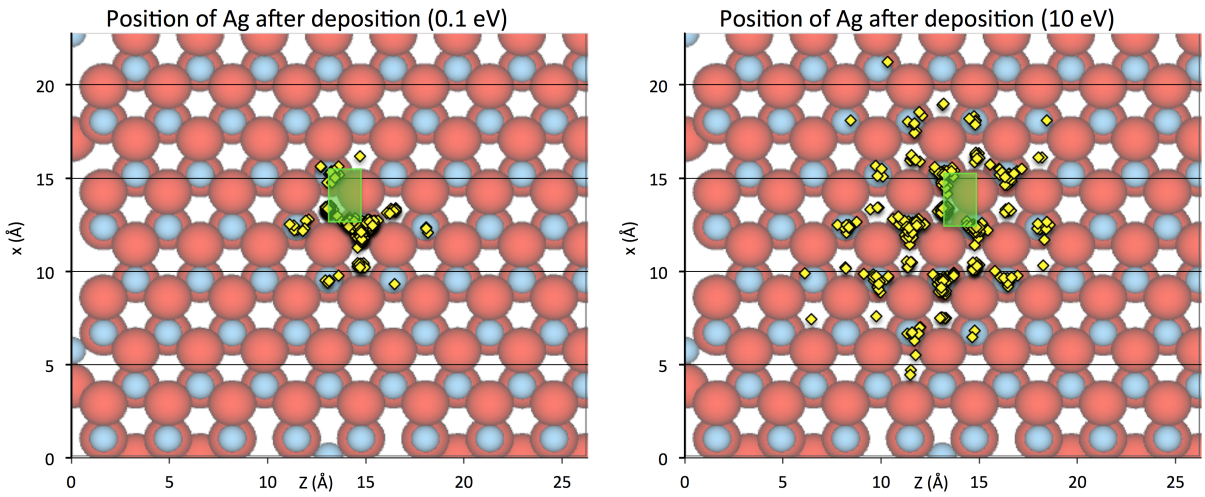

Figure 5.11 – Plots showing final positions of single Ag atoms deposited at 0.1 and 10 eV on a ZnO $(000\bar{1})$ substrate after 10 ps. Yellow diamonds indicate final position of Ag atoms and the green rectangle shows the deposition area. As one would expect, the higher the deposition energy the more the Ag atoms tend to move across the surface. Once Ag atoms are deposited, the atoms then bond to either an A (above a Zn atom) or C (hollow) adsorption site.

Table 5.6 – Ag dimer deposition on ZnO $(10\bar{1}0)$

	Deposition Energy (eV)				
Outcome	0.1	1	3	10	30
Adsorb (%)	100	100	100	99.75	89
Penetrate (%)	0	0	0	0.25	9.5
Reflect (%)	0	0	0	0	1.5
Split (%)	3.5	9	18	25.5	19

all Ag atoms adsorb. There are also cases of reflected atoms at 10 and 30 eV whereas none were reflected in the case of the polar surface. Note that the tendency for dimers to split is less marked than for the polar surface. This is due to Ag atoms in cluster formations being energetically favourable on the non-polar surface. Fig. 5.12 shows the final resting place of the Ag atoms after impact for energies of 0.1 and 10 eV.

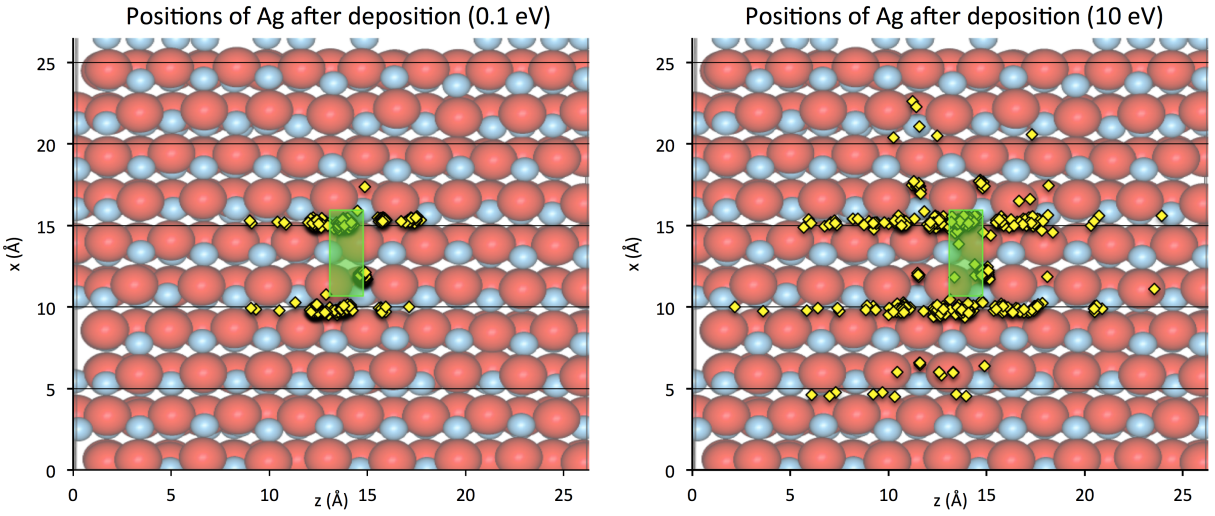

Figure 5.12 – Plots showing final positions of single Ag atoms deposited at 0.1 and 10 eV on a ZnO $(10\bar{1}0)$ substrate after 10 ps. Yellow diamonds indicate final position of Ag atoms and the green rectangle shows the deposition area. Again, the higher the deposition energy the more the Ag atoms tend to move across the surface. Ag atoms favour bonding sites away from surface Zn atoms.

5.4 Conclusions

A new potential to describe the Ag-ZnO system has been developed. The new parameters were fitted against DFT calculations with the aim of reproducing equations of state for simple crystal structures and Ag on ZnO binding energies. Overall, the fitted parameter set agrees well with the DFT data used within the fitting procedure as well as agreeing with experimental data and calculated works of separation. As a preliminary phase to undertaking growth simulations [69], single point depositions onto a perfect ZnO surface were also carried out. All low energy depositions (below 30 eV) of Ag onto perfect polar ZnO resulted in adsorption. Similar results were seen when depositing on the non-polar ZnO surface. Ag atoms do not penetrate the surface until energies of 10 eV or more are used. No reflection was seen on the polar surface in contrast to the non-polar case, where a small fraction of reflected atoms is predicted. This indicates that in magnetron sputtering deposition it may be better to use lower deposition energies if a sharp interface between the Ag film and the ZnO substrate is to be maintained.

The results from the newly developed ReaxFF potential differ largely from the single point

deposition results in chapter 4 using the simplified model. ReaxFF indicates a larger tendency for deposited Ag atoms to adsorb to the polar ZnO surface and no Ag atoms penetrate at energies of 10 eV or less. Penetrating Ag atoms were common, even at low energies, for deposition simulation using the simplified model due to the model over estimating the stability of interstitial Ag atoms.

The new potential better describes the interaction between Ag and the ZnO surface compared to the simplified potentials used in chapter 4. It correctly reproduces various properties of Ag/Zn/O interactions such as Ag interstitials and surface binding energies. Because of this, the ReaxFF potential developed for Ag/Zn/O surface interactions is used to conduct growth simulations via AKMC methods in the next chapter.

In practice, foreign adsorbents (including H and water molecules) may be found on the surface during the deposition process but are not considered in this potential. It could be possible to include some contaminates in the ReaxFF potential but this would affect efficiency.

Chapter 6

Growth Modelled Using an Improved ReaxFF Potential

With the creation of a new potential to model Ag interactions with ZnO surfaces, thin film growth simulations are again considered. The newly developed Ag/Zn/O ReaxFF potential discussed in chapter 5 is used to explore Ag growth on perfect and defective ZnO surfaces. As polar surfaces are more energetically favourable for Ag to grow on, the polar O-terminated ZnO $(000\bar{1})$ surface is used for growth simulations. Besides the perfect surface, growth is also modelled when the surface contains O-vacancies or step-edges, both of which are likely to be common occurrences during ZnO thin film growth [21].

6.1 Methodology

As with the previous model exploring Ag growth on ZnO, AKMC is used along with the RAT and NEB methods to find transitions and MD is used to simulate deposition events. The system is modelled at 300 K with Ag deposition occurring at an average 12 ml/s normal to the ZnO surface. The deposition energy used remains constant throughout the growth simulation at 3 eV. For the deposition events the bottom ZnO layer is fixed and the next two layers are attached to a Berendsen thermostat (Fig. 4.1) to keep the system at 300 K after deposition events. The

ZnO substrate considered had dimensions 22.8 × 8.1 × 26.3 Å with a surface containing 64 O and 64 Zn atoms. The methodology differs from that in chapter 4 in how defects are defined as well as the potential functions used. Two methods of defining defects (introduced in chapter 3) are compared in this chapter for growth on various ZnO surfaces.

6.2 Growth on Perfect ZnO Surfaces

The perfect $(000\bar{1})$ surface is considered first. Before full growth simulations are conducted, simple Ag ad-atom transitions are investigated using the NEB method. Initial and final states are found manually and minimised locally via a CG method. It was seen during single point depositions (Fig. 5.11) that Ag atoms adsorb on highly symmetric lattice sites - either directly above a hollow site (ABc stacking) or a Zn atom (ABa stacking). Two example transitions are considered here: the first is a single Ag atom hop between the two favoured sites. The transition of an Ag monomer from ABa to ABc stacking has a small energy barrier of 0.16 eV whereas the reverse barrier is larger at 0.52 eV (Fig. 6.1).

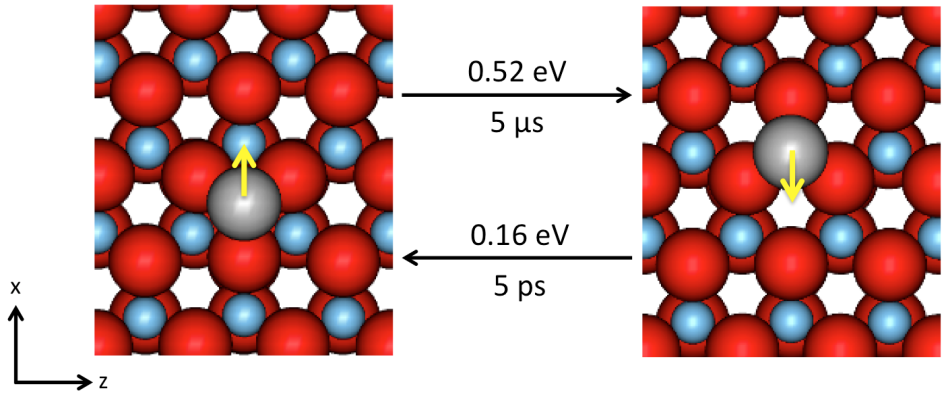

Figure 6.1 – Typical single Ag adatom transitions on a perfect ZnO $(000\bar{1})$ surface. Transition rates are calculated at 300 K. Yellow arrows indicate the direction of the transition.

Other transitions including multiple Ag atoms on the perfect surface are also investigated. It is shown here that the transition barrier height for an Ag dimer to split (0.41 eV) is smaller than it is to form (0.59 eV) - shown in Fig. 6.2. This indicates that, during initial growth simulation,

dimers are unlikely to form and stay together for any significant time. If a trimer of Ag atoms forms on the surface, the transitions barriers to split away or rotate become larger (Fig. 6.3). Clusters of 3 or more Ag atoms are stable for longer times on the perfect ZnO surface. Despite the fact that clusters become stable, the transition energy barriers for new ad-atoms to join the existing cluster are often greater than the barriers to diffuse away (Fig. 6.4) meaning that initial cluster formation could take a large amount of simulation time to occur. As a mechanism to bypass this, initial growth simulations are started with a high concentration of existing Ag ad-atoms (around 25% surface coverage) on the surface to encourage cluster formation (Fig. 6.5).

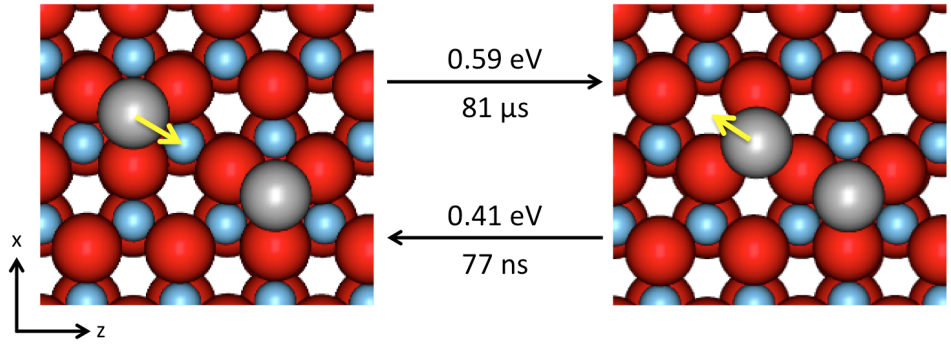

Figure 6.2 – Ag dimer forming and breaking transitions on a perfect ZnO $(000\bar{1})$ surface. Transition rates are calculated at 300 K. Yellow arrows indicate the direction of the transition.

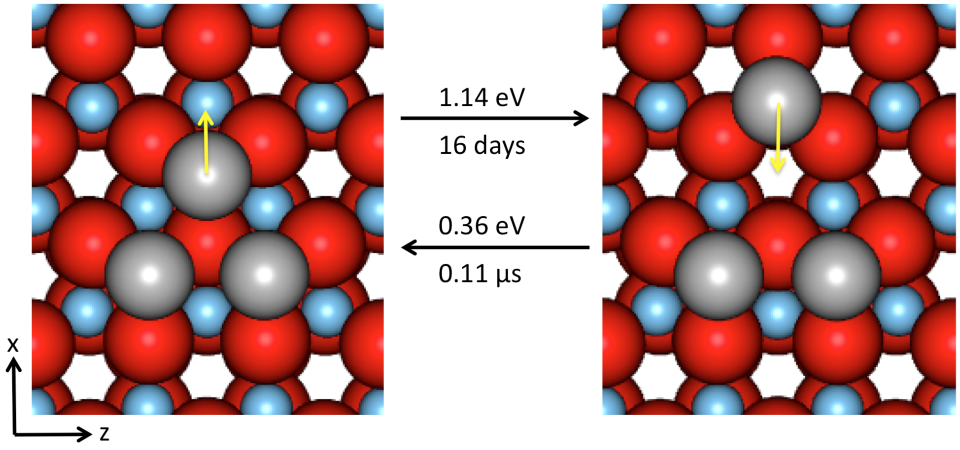

Figure 6.3 – Ag trimer forming and breaking transitions on a perfect ZnO $(000\bar{1})$ surface. Transition rates are calculated at 300 K. Yellow arrows indicate the direction of the transition.

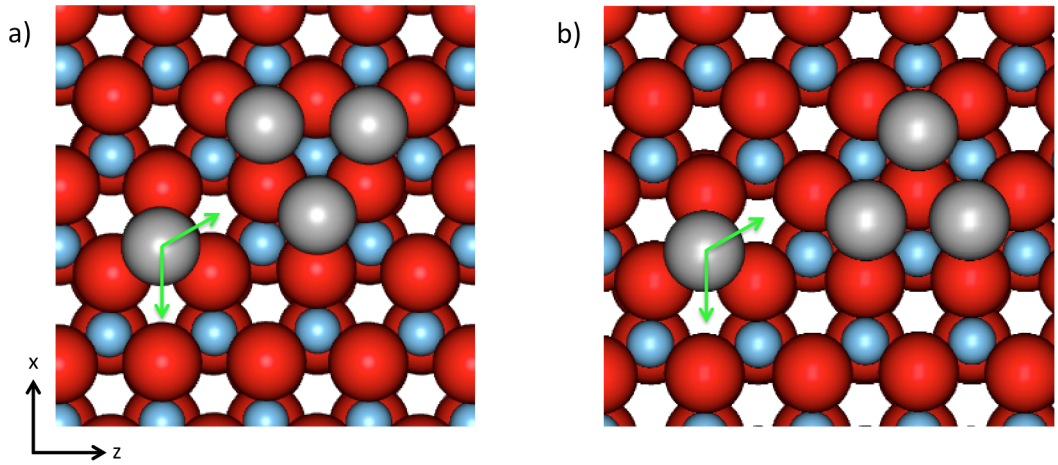

Figure 6.4 – Two examples of a single Ag ad-atom placed near an existing ABc stacked trimer. In both examples the transition barrier to join the existing cluster are larger than that to diffuse away. In the first example, a), the barrier for the single ad-atom to move towards the existing trimer is 0.3 eV and to move away is 0.16 eV. In the second example, b), the barrier to move towards the trimer is 0.23 eV and away 0.16 eV. Green arrows indicate the direction of transitions.

Once the initial lattice is setup, a growth simulation via AKMC methods is then run. With the high concentration of Ag atoms on the surface, clusters are forced to form. After clusters have formed, the stability of all the atoms means that deposition events are much more likely to occur. The simulation starts with well separated ad-atoms that then cluster together, followed by additional Ag atoms being deposited. Typically, the newly deposited atoms diffuse around the surface until they attach onto an existing cluster. This is then followed by another deposition event. The clusters that form have a strong tendency to be in the ABc stacking configuration. Growth then typically continues in this manner until a newly deposited atom joins the second layer of Ag. If an Ag atom deposits above existing Ag atoms, the transition energy barriers to diffuse on that layer are small (typically < 0.1 eV) whilst energy barriers to drop down to the first layer are far larger (> 0.7 eV). When an instance of this occurs, the small energy barrier transitions dominate the simulation with no significant net diffusion in the system. As barriers to detach from existing islands on the first layer of Ag are much larger, the KMC algorithm will almost always choose a diffusion event for the Ag atom on the second layer over other diffusion or deposition events.

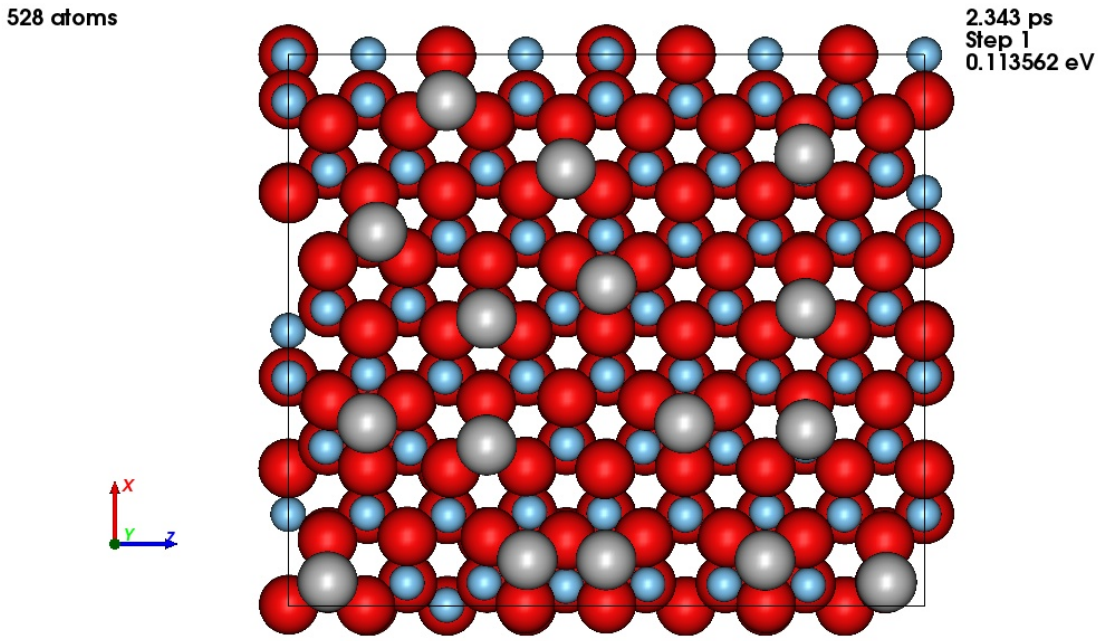

Figure 6.5 – Example initial configuration of 16 Ag ad-atoms on the ZnO surface to encourage cluster formation.

At the beginning of this work, surface growth simulations were conducted using a simple defect definition that meant any newly deposited atom was considered a defect. When using this definition, defects that were in close proximity of each other combined to create a single defect volume. However, if all ad-atoms are considered defects, once the ZnO surface was mostly covered by grown Ag, all deposited Ag atoms were then considered as one large defect volume. The KMC algorithm conducts a given number of searches per defect volume. The number of searches used per defect volume for Ag growth on ZnO is 1000 searches. This number of searches is sufficient to find a large number of possible transitions in the early stages of growth. However, once the defect volumes grow larger, the number of possible transitions increases whilst the number of searches remains unchanged. In Fig. 6.6, 102 additional Ag atoms are deposited during 930 KMC steps. Thus, the initial 16 and the additional 102 Ag atoms form one large defect volume. This then equates to 1000 searches done on 118 Ag ad-atoms, of which many are in highly stable sites and are unlikely to move. Due to the low number of searches per ad-atom, little (or no) successful transitions are found using the RAT search method.

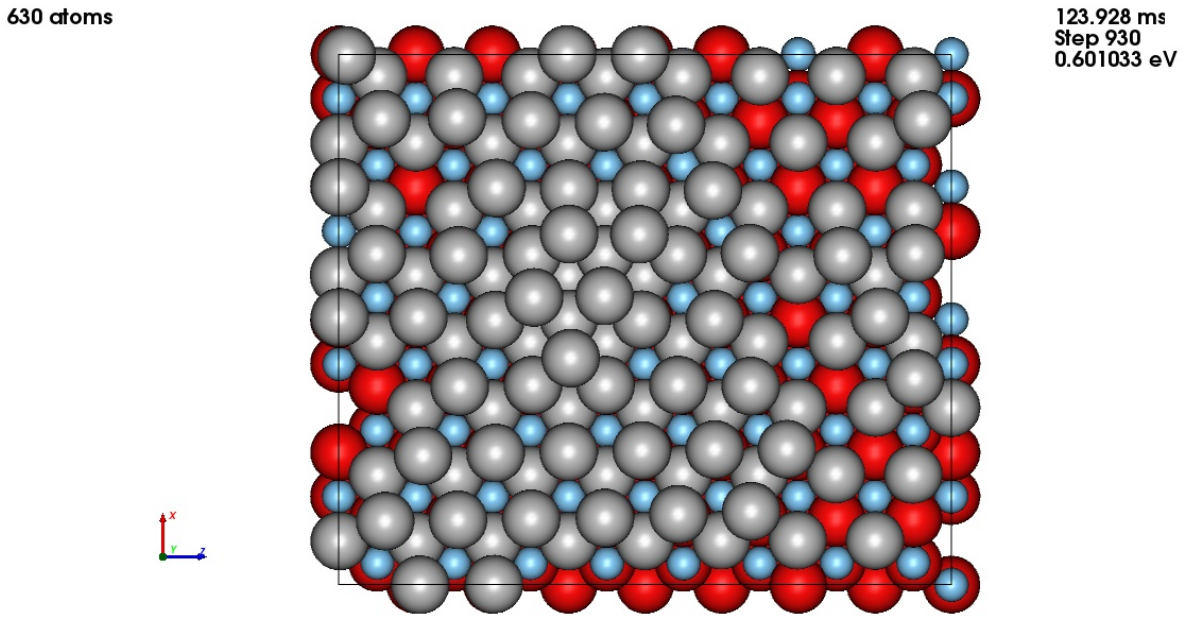

Figure 6.6 – Example of multilayer Ag growth on ZnO after 124 ms. In this simulation, defects were defined by comparing atoms positions to a perfect reference lattice.

Simulations using this method of defect definition when growing Ag on perfect ZnO surfaces result in total first layer coverage. Initially large clusters form and second layer clusters also occur whilst small pockets of the ZnO surface is left uncovered. However, after successive randomly positioned deposition, the first Ag layer becomes complete. All deposited Ag atoms in the first layer are positioned in the favourable ABc adsorption sites. Second layer Ag atoms also have a strong tendency to reside in ABcb (directly above O atoms) adsorption sites. This means that phase or twin boundaries are unlikely to occur during initial growth phases. During this simulation, the start of a third layer of Ag also forms whilst the second layer is partially complete.

To achieve a more realistic set of transitions during the later stages of growth simulation, a second method for defining defects is used. Atoms are considered defects if they are under-coordinated. Thus, atoms in stable positions in the middle of a cluster are then not included in defect lists. This also means, if a full, perfect layer of Ag is deposited, the effective surface

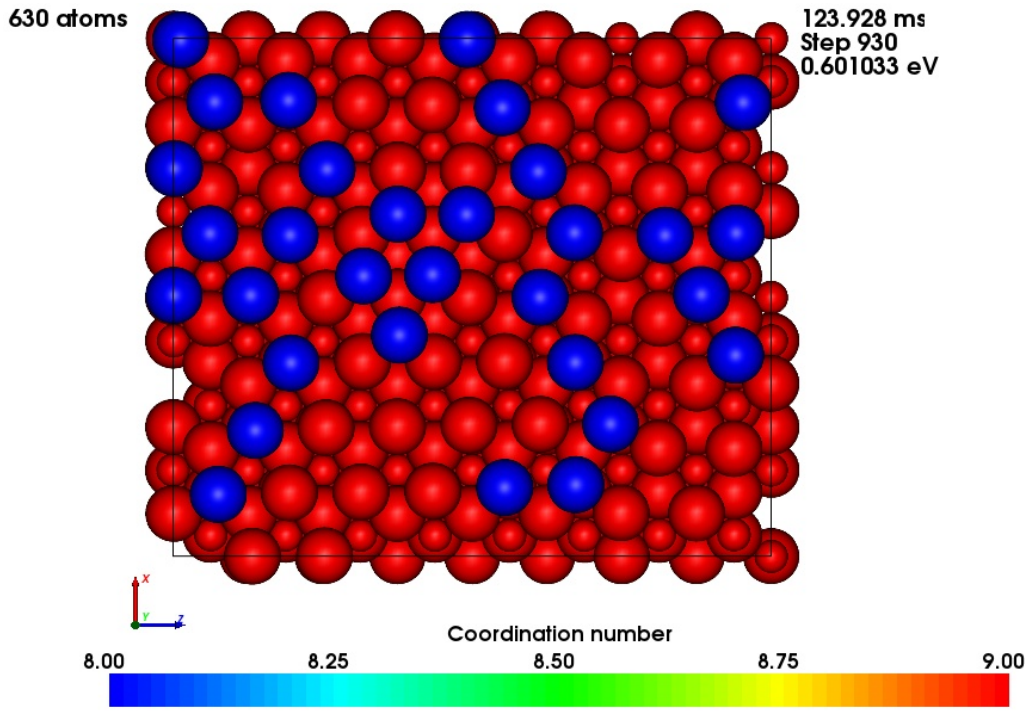

Figure 6.7 – Multilayer growth system with atoms coloured according to their coordination number. Red atoms are fully coordinated whereas blue atoms are under-coordinated Ag ad-atoms in the second and third Ag layers.

height for new searches rises and the number of atoms on which to conduct searches is then reduced. In Fig. 6.6, all 118 Ag atoms in the system are considered as defects. Defect volumes are then produced from these defects and searches are conducted on each defect volume. If only under coordinated atoms were defined as defects, only 31 of the 118 Ag ad-atoms would be considered (Fig. 6.7). The results from this defect definition can be seen during a growth simulation in Fig 6.8. Here, only 5 additional Ag ad-atoms are deposited after 1168 KMC steps. This is due to more transitions being found at each step when compared to simulations using the previous defect definition. Because the number of realistic transitions found greatly increases, this simulation more realistically models the initial growth dynamics of Ag on ZnO.

In both cases, Ag initially forms clusters on the ZnO surface until a newly deposited Ag atom is deposited above an existing Ag cluster. When this happens, the second layer Ag atom is likely to remain on the cluster throughout multiple further deposition events due to the larger

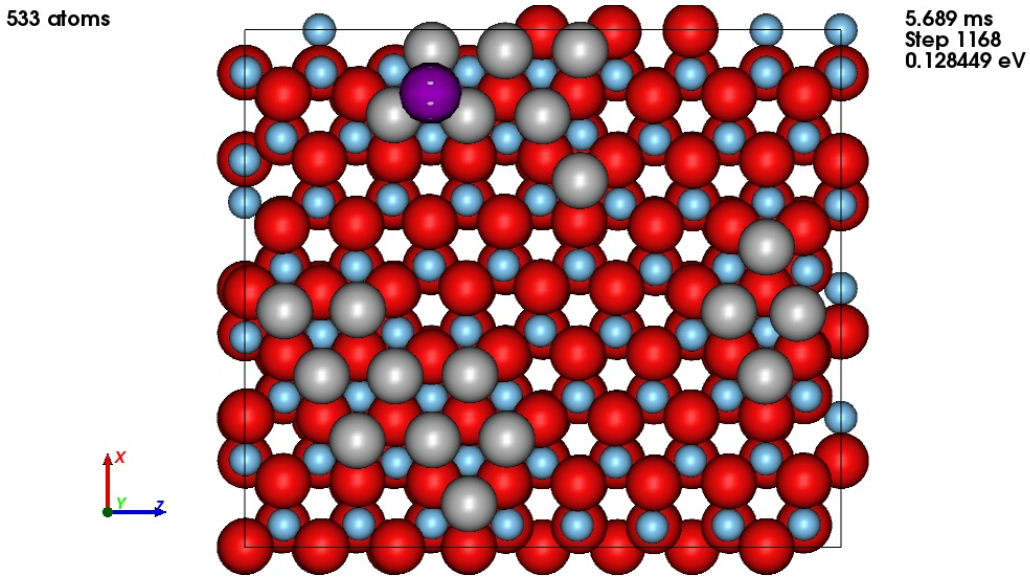

Figure 6.8 – Initial growth results after 5.7 ms of simulated growth. 5 additional atoms have deposited in this time and clusters have formed. The highlighted purple atom is an Ag atom that has deposited on top of existing Ag atoms. In this simulation, defects were defined by coordination number.

barriers to drop down a step edge (0.35–0.72 eV). Thus the second method of defining defects results in a different coverage where islands containing atoms in multiple layers can form.

6.3 Growth on Oxygen Deficient Surfaces

6.3.1 Single Oxygen Vacancy

Growth simulations of Ag on ZnO are not limited to perfect surfaces; Ag growth is also considered on surfaces which are O-deficient. Surfaces with various defects are a common occurrence when ZnO is grown [23]. A simple defective surface to consider is one that is missing a single O atom at the surface. This causes minimal distribution to the surface and only leaves a single vacancy in its place.

How Ag ad-atoms behave around surface O vacancies is investigated by calculating the relative energies of a single Ag ad-atom positioned in various sites on a surface containing a single

Table 6.1 – Relative energies of structures seen in Fig. 6.9 compared to a ZnO surface with a single O vacancy and no Ag ad-atoms.

Structure	a)	b)	c)	d)
Relative Energy (eV)	-2.43	-3.17	-3.30	-2.65

O vacancy (Fig. 6.9). The relative energies are given in Table 6.1. Results suggest that Ag ad-atoms prefer to reside in sites away from surface O vacancies with the most energetically favourable structure being the one with a single Ag ad-atom, in a hollow site, far away from the surface defect.

In addition to single energy calculations, initial growth simulations are considered on a perfect surface with a single O vacancy. If the original defect definition is used, growth appears to occur in very similar way to that of Ag on a completely perfect ZnO surface. The O vacancy initially repels Ag ad-atoms during the first few milliseconds of growth. However, once more and more Ag deposits onto the surface, the O vacancy has little affect on Ag cluster formations and initial growth (Fig. 6.10).

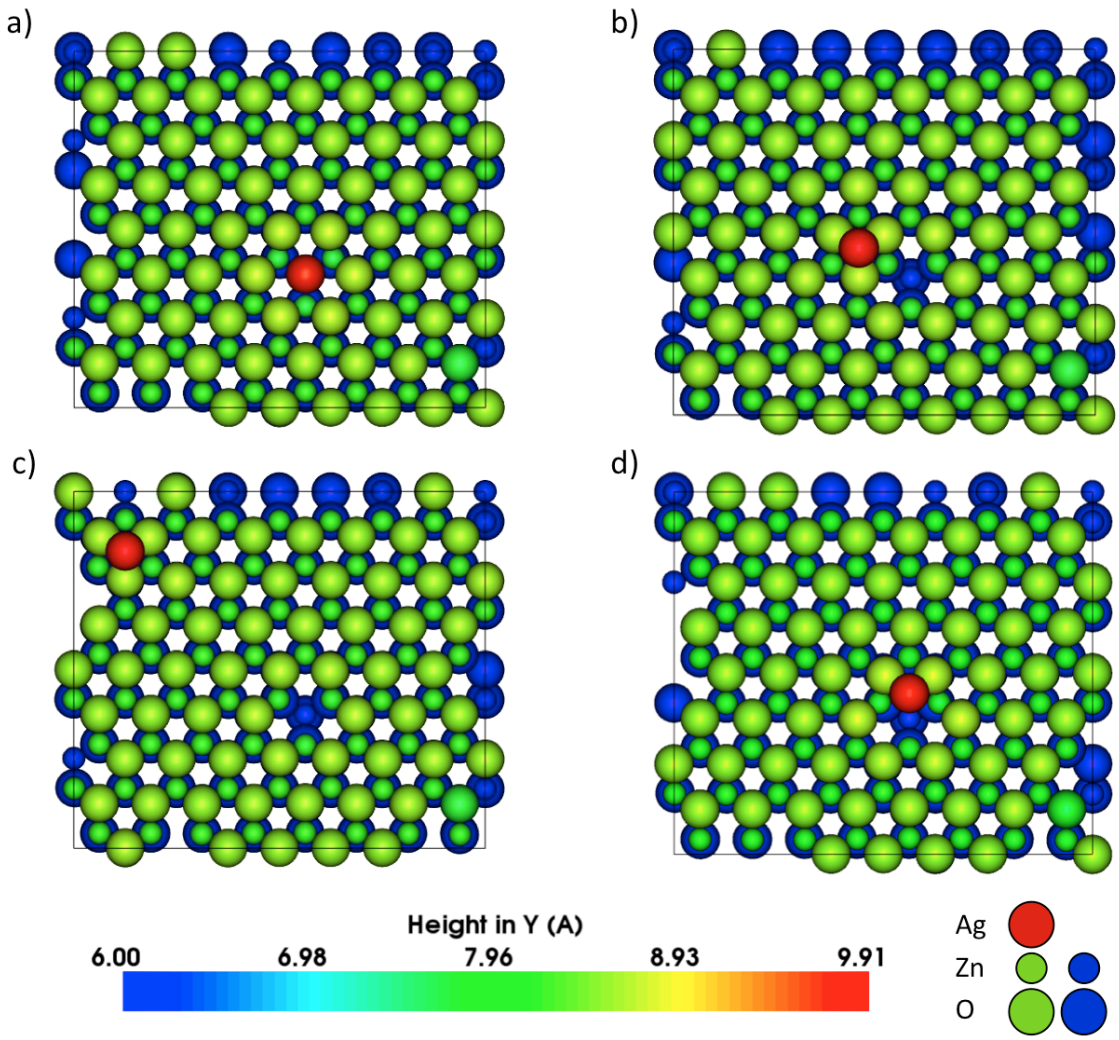

Figure 6.9 – A ZnO $(000\bar{1})$ surface with a single O vacancy and an Ag ad-atom in four positions: a) directly above the vacancy, b) in a hollow site outside of the vacancy, c) in a hollow site far away from the vacancy and d) in a site directly beside the vacancy. Atoms are coloured by height (Å) in the y direction. Here smaller green and blue spheres represent Zn, larger green and blue spheres present O and the red spheres denote the Ag ad-atom.

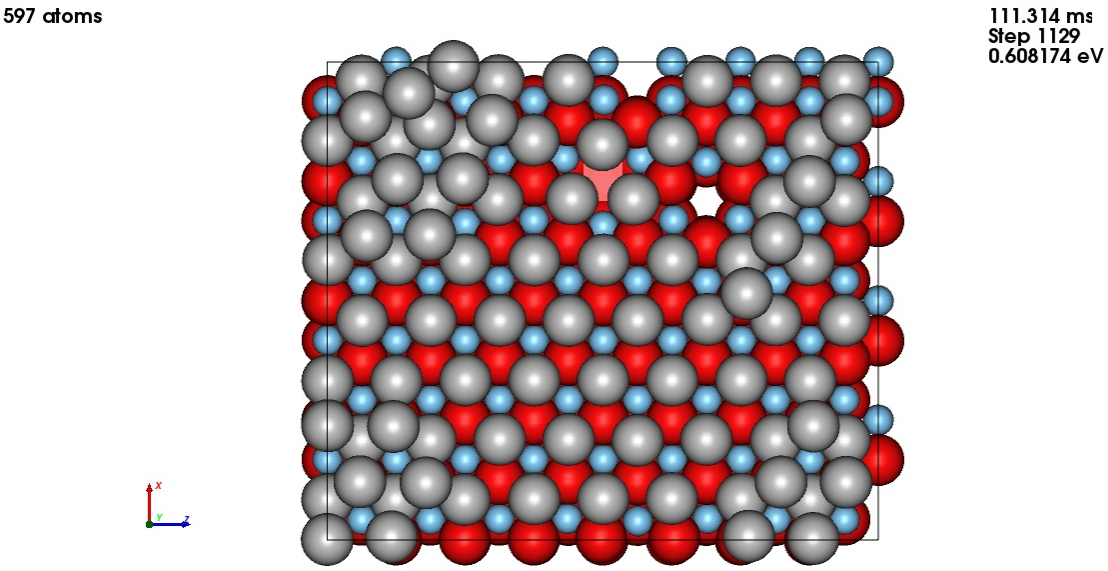

Figure 6.10 – Growth of 85 Ag atoms on a ZnO surface including one O vacancy. The simulation time is up to 111 ms. Initial Ag growth appears to be unaffected by the O vacancy in the surface as Ag atoms clusters to form a near perfect first layer. In this simulation, defects were defined by comparing to a perfect lattice. The pink cube (top middle) denotes the missing O in the ZnO surface.

6.3.2 Multiple Oxygen Vacancies

To investigate further O deficient surfaces, surfaces with multiple O vacancies in the surface are considered. There are two types of multiple O surface vacancies that will be studied. First will be the case where multiple single O vacancies occur on a surface separated from each other. The second is where O vacancies occur together. This causes a shift of other O atoms to reduce the instability of the surface created (Fig. 6.12). Vacancy clusters have been shown to occur during growth simulation by Blackwell [23].

Initial growth results for 3 separate O vacancies on the ZnO surfaces show that individual defects do not affect the formation of Ag clusters. In this simulation, only Ag atoms and vacancies were considered as defects. Oxygen and zinc atoms surrounding surface defects are very stable. Thus, successful transition searches, with higher rates than the deposition rate

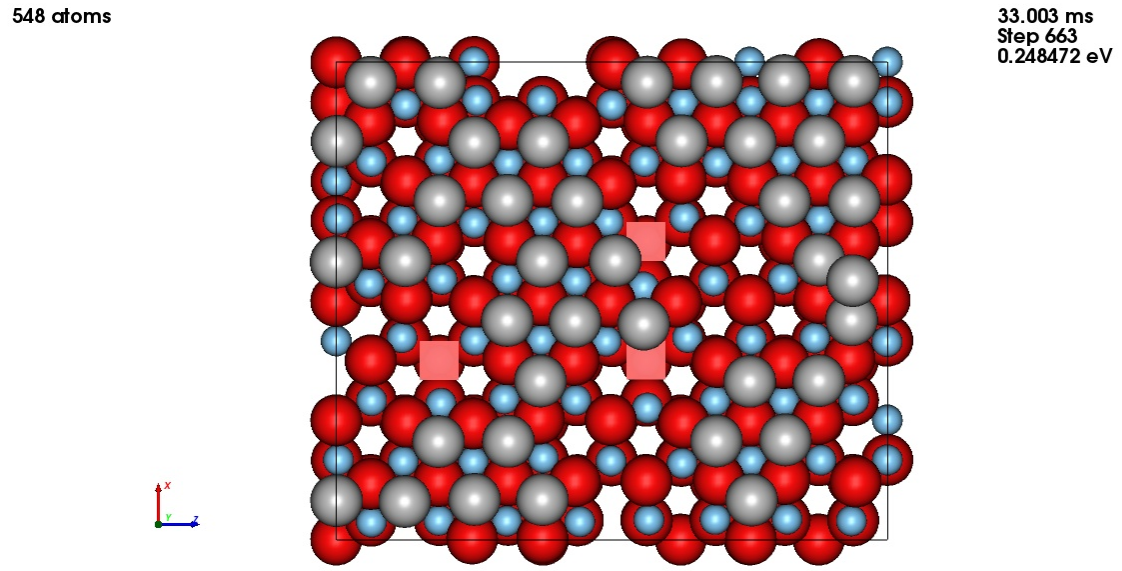

Figure 6.11 – Example simulation of Ag growth on a ZnO surface including three randomly placed O vacancies. A total of 36 Ag atoms have deposited on the ZnO substrate in 33 ms. In this simulation, defects were defined by comparing to a perfect lattice. The missing O atoms are marked by the pink cubes.

considered, are confined to Ag ad-atoms.

For the case where multiple O vacancies are placed together and the surface reconstructs to a more relaxed structure, a triangular region surrounding the defects is produced. This triangular region appears to have a bigger affect on Ag growth than individual vacancies. Throughout initial growth results on this surface, single Ag atoms avoid the triangular structure and form clusters around it. The occasional Ag atom that might diffuse into this region, rapidly leaves and joins the defect free part of the surface again, see Fig. 6.12.

6.4 Growth on Surfaces with Step Edges

The next surfaces considered are ones that include step edges. During the growth of ZnO thin films, it is likely that imperfect surfaces form that consist of steps and O vacancies [21]. An example surface is considered with an additional 48 Zn and O atoms placed in a strip along the surface (Fig. 6.14). This surface then contains two straight step edges along the x-direction.

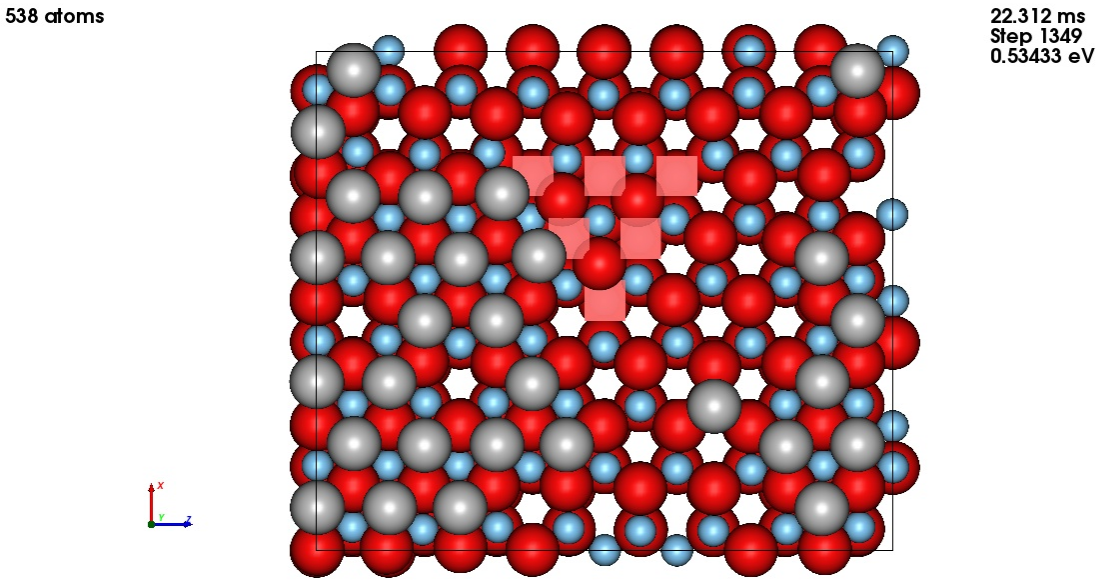

Figure 6.12 – An example ZnO surface where three O atoms are removed, forming vacancies, and the surrounding surface reconstructs to a more stable state. A total of 26 Ag atoms are then deposited after 22 ms of simulated time. In initial growth simulations, Ag ad-atoms are repelled from the surface defects. In this simulation, defects were defined by coordination number

Example transitions of a single Ag atom dropping off the step edge to join the lower surface or and climbing up the step edge are considered (Fig. 6.13). Both transition barrier heights are large (0.87 eV and 1.01 eV) and are unlikely to occur in AKMC time scales.

Growth simulations are conducted on this substrate where initially 16 Ag ad-atoms are placed on both the upper and lower levels of the created ZnO surface (Fig. 6.14). For simulations on this structure, the coordination number defect definition is used. This considers O and Zn atoms on the edges of the steps as defect as well as the Ag ad-atoms.

The AKMC simulation results in Ag atoms diffusing towards the ZnO step edges and bonding to under-coordinated O atoms (Fig. 6.15). The Ag atoms from the lower and upper surfaces congregate along the step edges and form Ag-O clusters. Once these clusters form, oxygen atoms along the step edge can separate from neighbouring zinc atoms and then rejoin with transition barriers around 0.2 eV. These low energy transitions then dominate the AKMC

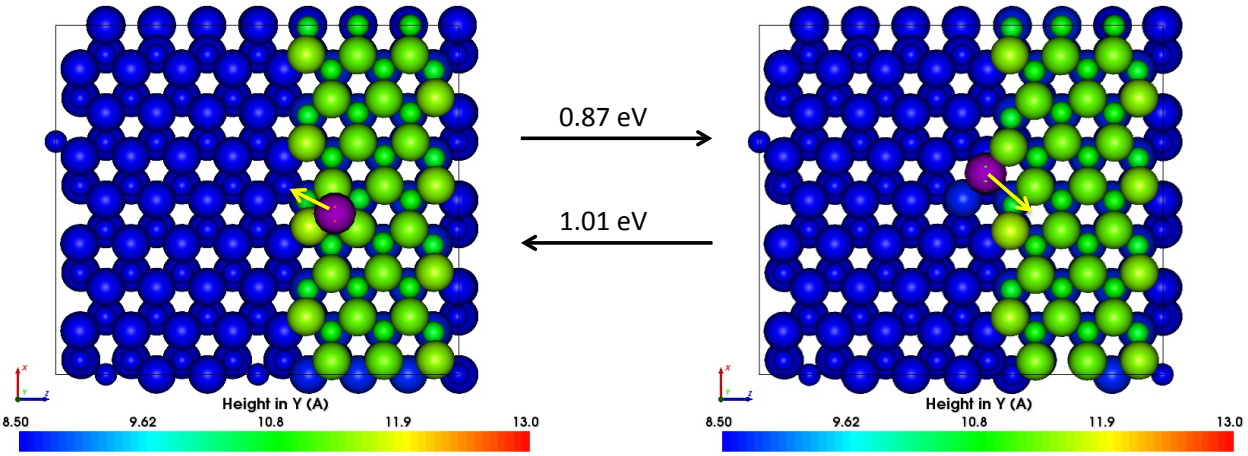

Figure 6.13 – Example transitions of an Ag atom dropping down or climbing a ZnO step edge. Here atoms are coloured by height: green spheres represent the upper ZnO layer whilst the blue spheres represent the lower ZnO substrate. Small spheres indicate zinc atoms, large represent oxygen atoms whilst the purple sphere represents the Ag atom.

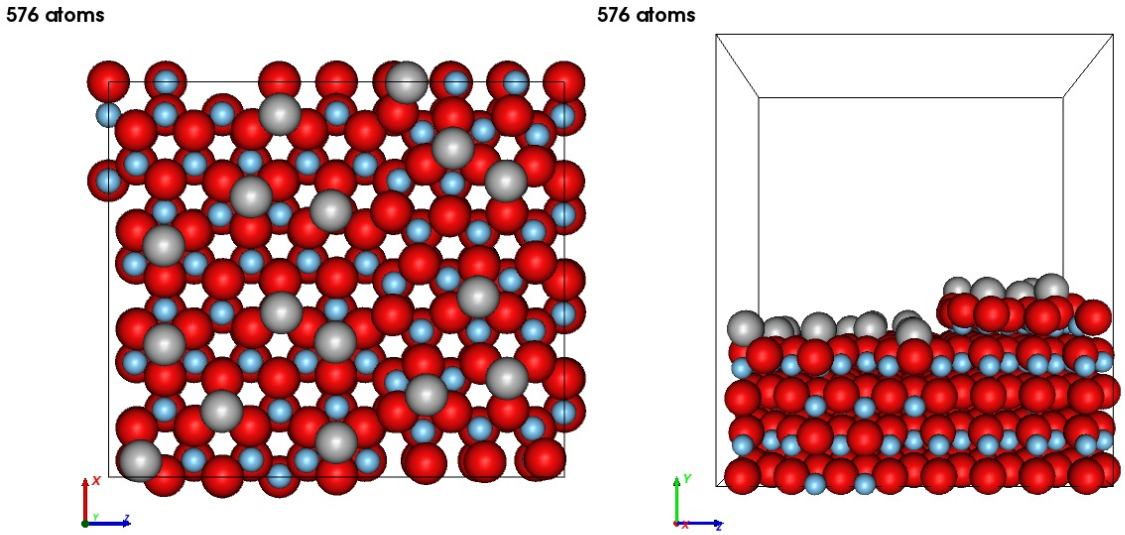

Figure 6.14 – The starting configuration for an AKMC simulation on a perfect ZnO surface with the inclusion of a step. 16 Ag ad-atoms are initial well separated.

simulation with no further net diffusion seen after 700 steps. Some Ag ad-atoms do not join the step edge but instead form a single Ag cluster of 3 atoms after 39 μs on the lower surface. Overall, the step edges attract Ag ad-atoms from the lower and higher parts of the surface. The relative energy difference between a single Ag on the lower surface away from the step edge and an Ag atom attached to the step edge is around 0.2 eV in favour of the step edge site.

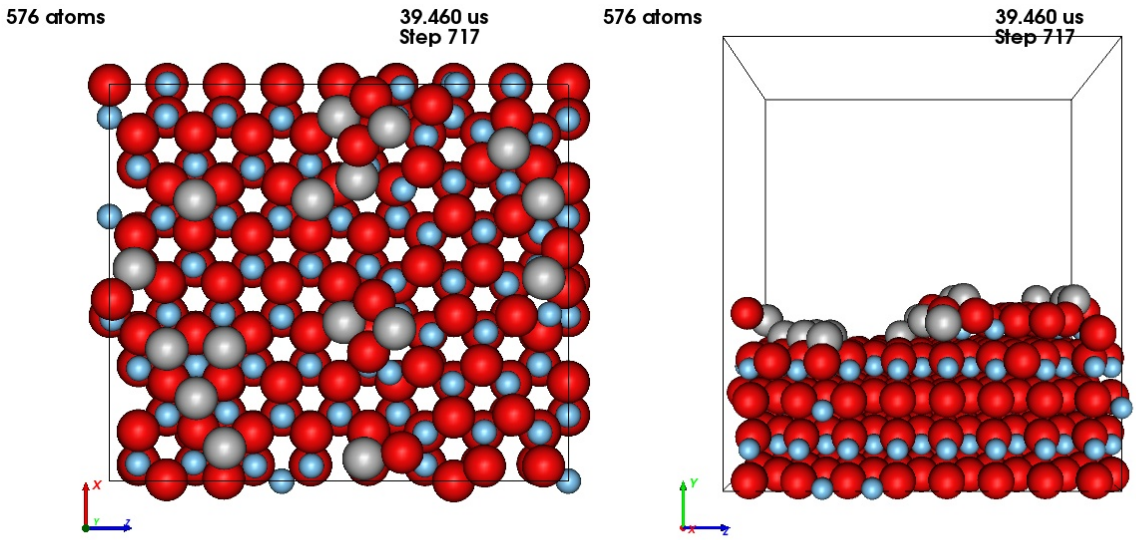

Figure 6.15 – The system after 717 KMC steps (39 μs). No additional Ag atoms are deposited in this time.

6.5 Conclusions

Initial growth results on a perfect ZnO surface indicate that clusters do form on the surfaces. However, when additional ad-atoms are deposited above existing Ag atoms, small energy barriers dominate the simulation and thousands of KMC steps can occur before the Ag ad-atom drops off to join the first Ag layer or another deposition event is chosen. Each KMC step is computationally expensive in these simulations. Each transition search can takes minutes to compute and in turn results in years of CPU time for 1000 AKMC steps to be completed.

Depending on the defect definition used, 1000 AKMC steps either result in little growth (less than 10 additional atoms) or multilayer growth due to insufficient low energy transitions being found. If defects are defined by comparing against a reference lattice, less transitions are found and so deposition is more likely to occur at each step. In contrast, if defects are defined locally by the coordination number, more transitions are found and thus deposition is less likely to occur at each step resulting in less growth in the same number of AKMC steps. To run further growth simulations whilst maintaining a high number of possible transitions, a new, more efficient method is needed. Whilst the implementation of the basin method would

accelerate simulations, only around 2-3 thousand AKMC steps would be possible (on current computer resources) to be completed due to the computationally expensive ReaxFF potential and search methods used. Thus in the following chapter, a lattice based AKMC method is used as a method to accelerate simulations to multilayer growth whilst including a large number of possible transitions at each step.

Chapter 7

Growth Modelled via Lattice AKMC Simulation

7.1 Methodology

During off-lattice KMC simulations, it is seen that Ag ad-atoms most commonly sit in highly symmetric sites on the perfect polar ZnO $(000\bar{1})$ surface (Fig. 7.1). This is also the case when Ag diffuses on top of an existing first layer of Ag on the ZnO surface. Due to this behaviour of deposited Ag atoms, a lattice based system might be assumed and used with KMC simulation to increase the efficiency of reusing previously found transitions and eliminate the need to use single ended search methods to find final transition positions. The method can also handle larger systems than considered in the previous chapter.

For LatAKMC, all possible initial and final positions are assumed to be on a lattice. For the ZnO $(000\bar{1})$ surface, a hexagonal lattice is considered. The first layer ad-atom can move in three different directions in the surface plane and possibly also jump up to the second layer. A second layer ad-atom can move in 3 directions on the Ag plane with the possibility to jump down or up a layer if appropriately sited. To calculate barriers between states, the initial and final states

Table 7.1 – Possible transitions of first layer Ag ad-atom on the perfect ZnO surface. Adsorption site labels refer to those in Fig. 7.1. Note that 'B' adsorption sites are unstable. E_B denotes barrier height and corresponding rates are calculated at 300 K.

Initial	Final	E_B (eV)	Rate (s^{-1})
A	C	0.16	2.05×10^{10}
C	A	0.52	1.84×10^{4}

are first minimised using a conjugate gradient minimiser [66], then the nudged elastic band (NEB) [42] method is used. To calculate the rate of transition, the Arrhenius equation is used. All energy and force calculations performed are done using the ReaxFF potential developed for Ag on ZnO surfaces [12]. Transitions are stored on objects (with a given hash key) that identify local initial and final states such that the atoms outside of a certain local radius have a negligible effect (< 0.01 eV) on barrier heights. For this system, the radius is taken to be 5.9 Å. Calculated barrier heights and corresponding rates for single ad-atom diffusions on the perfect ZnO surface are given in Table 7.1.

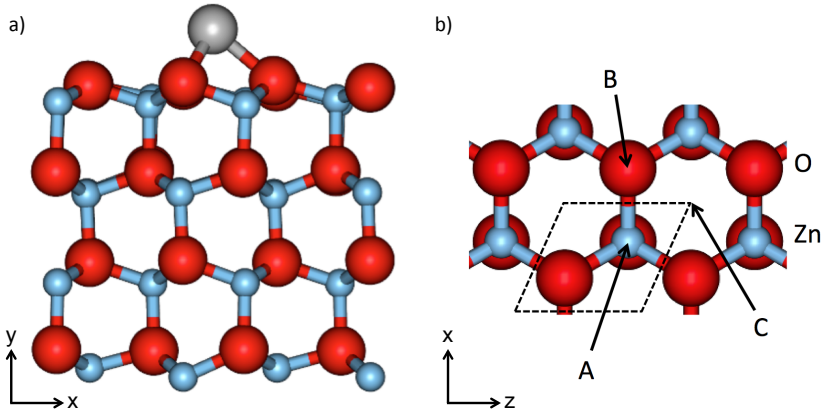

Figure 7.1 – Schematic structures of the O-terminated polar ZnO $(000\bar{1})$ surface with (a) - an Ag ad-atom and (b) - potential adsorption sites for deposited Ag atoms labelled A, B and C. Red, blue and grey spheres represent O, Zn and Ag atoms respectively. When the first layer of Ag forms, only sites A and C are stable but when an Ag ad-atom is deposited in the second layer, on top of Ag, it can sit above the A, B or C sites in the ZnO layer. The transition barriers for ad-atom diffusion between A and C sites are given in Table 7.1.

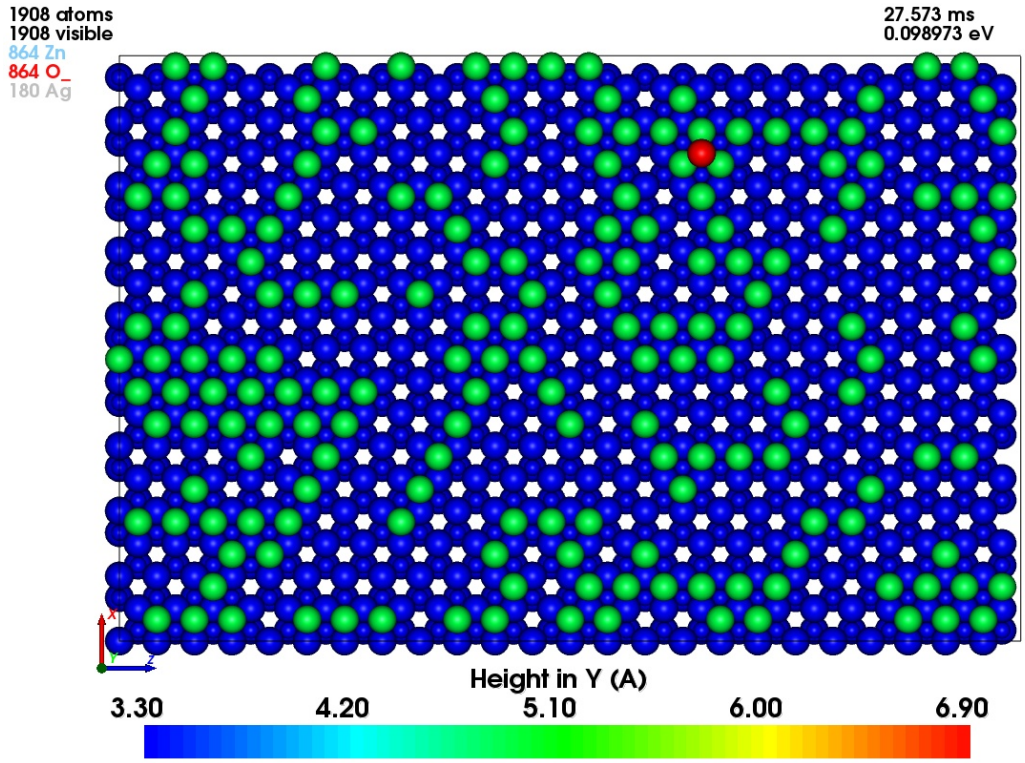

Figure 7.2 – Example growth structure after 27.6 ms of simulation. The ZnO surface consists of 432 Zn and 432 O atoms and 180 additional Ag ad-atoms are deposited at an average rate of 12 ml/s. Atoms are coloured by height in the y direction (Å). Large blue spheres represent O and small blue Zn surface atoms whereas green and red denote first and second layer Ag atoms respectively.

In LatAKMC either a diffusion event or a deposition event occurs as in off-lattice KMC [15]. The previous chapter used a combined MD-AKMC approach to deposit new atoms. Here, the MD part is replaced by randomly placing an atom on stable lattice sites. During initial growth, single ad-atoms diffuse readily across the surface. Ag dimers can form and split at similar rates (with transition barriers typically between 0.4-0.6 eV). Once clusters of three or more Ag ad-atoms start to form, the energy barriers to escape the cluster become larger and so 3 atom clusters act as nucleation sites on the surface. Many small clusters form initially and can then join together via single atoms strings (Fig. 7.2). Once atoms begin to deposit on existing Ag clusters, small energy barrier transitions can dominate the simulation. As before, this can result in vast amounts of computational time being used without any significant evolution within the system. Fig. 7.3 shows a second layer Ag atom above an existing first layer cluster. The lowest

Table 7.2 – Two possible in plane transitions and the two step down (escaping the island) transitions with corresponding barrier heights and calculated rates on a first layer ABc stacked island. E_B denotes barrier height and corresponding rates are calculated at 300 K.

Initial	Final	E_B (eV)	Rate (s^{-1})
Above Zn	Above O	0.17	1.56×10^{10}
Above O	Above Zn	0.30	8.77×10^{7}
Above Zn	Escape	0.35	1.32×10^{7}
Above O	Escape	0.72	8.02

energy barriers for diffusion on the current layer are 0.17 eV and 0.3 eV. These are lower than the relative barriers to escape (drop down to the first layer - see Table 7.2) or the equivalent barrier for deposition (0.59 eV for a 100 atom surface).

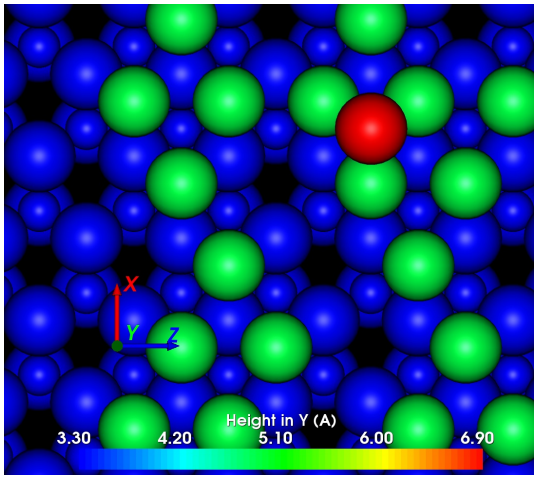

Figure 7.3 – Example configuration of a second layer Ag atom that will flip between adsorption sites above first layer Ag atoms with the relative transition rates shown in Table 7.2. Atoms are coloured by height in the y direction (Å). Large blue spheres represent O and small blue Zn surface atoms whereas green and red denote first and second layer Ag atoms respectively.

Table 7.3 – Two possible in plane transitions and two step down (escaping the island) transitions with corresponding barrier heights and calculated rates on a second layer ABcb stacked island. E_B denotes barrier height and corresponding rates are calculated at 300 K.

Initial	Final	E_B (eV)	Rate (s^{-1})
Above Ag	Above Zn	0.01	6.79×10^{12}
Above Zn	Above Ag	0.06	9.82×10^{11}
Above Ag	Escape	0.75	2.51
Above Zn	Escape	0.89	1.12×10^{-2}

As islands are seen experimentally when growing Ag on ZnO, it is interesting to see if the simulations can also predict this, and if so what size they would grow to. To investigate island formation and interaction, we must first know how large Ag islands are expected to be on the surface and then use LatAKMC to model a system large enough to incorporate multiple islands of this size. Having determined transitions on the first (Table 7.1) and second layers (Table 7.2), third layer transitions were also investigated. The results of these are shown in Table 7.3. Some of the barriers for diffusion in the third layer are even lower than those barriers in the second layer whilst escape (in this case jump down to second layer) barriers are very high. Including these small barriers in a traditional KMC approach is even more expensive computationally than including the second layer events. As a result, the mean rate method is used in this section to overcome the low energy barrier problem as well as approximating critical island sizes.

7.2 Critical Island Size

The formation of islands during Ag thin film growth on ZnO has been witnessed experimentally [22] and investigated via *ab initio* methods [4]. Further investigation is conducted by using a lattice based adaptive kinetic Monte Carlo (LatAKMC) model to simulate initial growth phases of Ag on a perfect O-terminated ZnO $(000\bar{1})$ surface. A mean rate method approach is used for predicting island size on a perfect ZnO surface and a single Ag layer applied to a perfect ZnO surface.

The question of finding the critical size of islands in growth simulations has been asked for many systems [70, 71, 72]. A new approach to answering this question is presented. An atom above an island is considered in a "super-basin" as long as it stays on the island. It is considered as having exited the "super-basin" once it drops off and joins the layer below. This means that a mean rate method (MRM) approach can be used to find the mean residence time of an atom on an island. This residence time can be compared to the mean time between new deposition events on the island to find a critical island size. Any island larger than the critical island size would suggest a new atom is more likely to be deposited on the island than an existing atom is to drop off and thus more likely to continue island growth.

7.2.1 Results

For the case of a single layer Ag island - in the energetically preferable ABc (FCC) stacking - on the ZnO surface, we assume that there are 2 different types of basin states (directly above an O atom or Zn atom) and that a basin state of one type can only move to a basin state of the other type or escape the basin. The rates to move between states are calculated by using NEB to find the barrier height and the Arrhenius equation to convert the barrier height to a rate depending on system temperature (Table 7.2). Islands are assumed to be in regular hexagonal shapes on the surface for simplicity.

The mean time to escape a first layer Ag island on the perfect ZnO surface is compared against the average time between subsequent depositions (see Fig. 7.4). The results indicate that small changes in system temperature can hugely affect the critical island size. For a deposition rate of 12 monolayers per second (ml/s), at temperatures below room temperature (293K), the critical island size is less than 350 Ag atoms, whereas for higher temperatures, critical island sizes can be in excess of 500 atoms. As well as temperature, deposition rate also has a significant effect

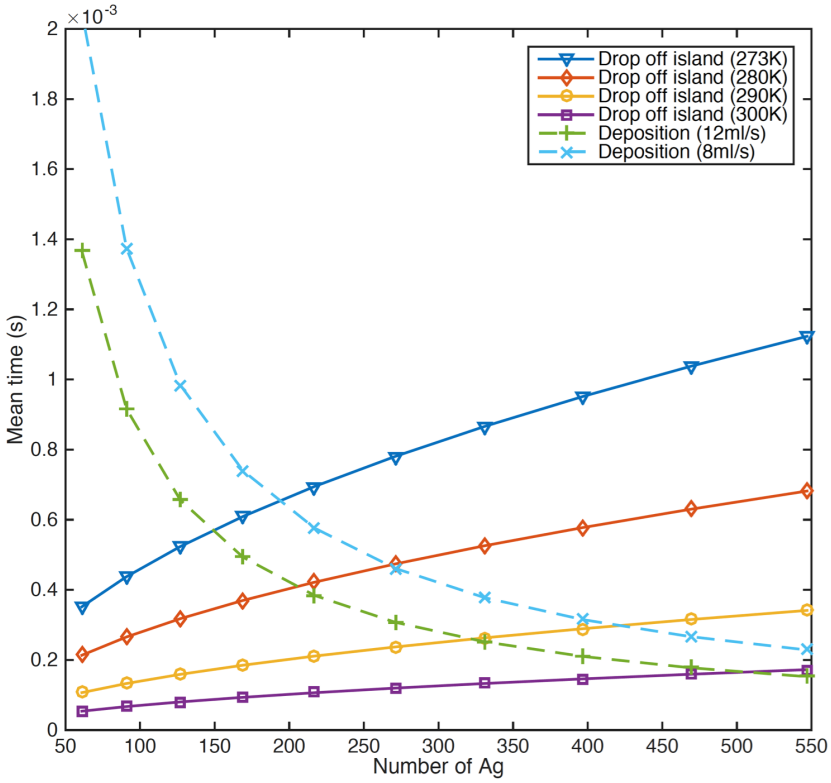

Figure 7.4 – A graph comparing the mean time for ad-atoms to drop off a first layer hexagonal Ag island (in favourable ABc stacking) at various temperatures and the time of new atoms being deposited on the island.

on critical island sizes.

For second layer islands (Table 7.3) in a favourable ABcb (first layer FCC and second layer HCP) stacking configuration, transition rates between states within the island are 2-3 orders of magnitude larger than in first layer islands. In addition, transition rates to escape the island are smaller and thus result in critical island sizes of less than 7 atoms when considering a deposition rate of 12 ml/s. For our system setup (temperature at 300 K and a deposition rate around 12 ml/s), we would expect large or no islands forming on the first layer of growth but many small islands forming on subsequent layers of Ag growth. This would result in a layer plus island (Stranski-Krastanov) type growth of Ag on perfect ZnO surfaces.

7.2.2 Summary

Critical island analysis on perfect ZnO surfaces predicts a layer by island growth model at initial growth phases (less than 2 layers high). However, island sizes may differ on defective ZnO surfaces. For our model, in order to simulate a system that may include multiple initial islands, we would have to either consider a system with a surface of at least a few thousand atoms, decrease our deposition rate or increase our system temperature. Despite this, an investigation of further island formation on subsequent layers of grown Ag could be conducted on a smaller surface with typical system temperatures and deposition rates.

Experimental results show a large quantity of small islands forming after 8 monolayers of Ag growth [22] but island formation on the first layer is unclear. Our critical island analysis agrees that small islands are likely to form after an initial layer of Ag growth. This approximation considers only isolated perfect hexagonal clusters whereas different island shapes and multiple clusters would affect the drop off time.

7.3 Growth on Perfect ZnO Surfaces

The lattice based AKMC method is used to reduce computational time and achieve growth results on larger systems. Longer time scales are also an advantage of the method. Two systems are considered in this chapter: one with a surface size of 100 O atoms and one with a surface size of 432 atoms. The smaller surface is considered to compare against off-lattice AKMC methods and to reach maximum simulation times, whereas the larger system is used to investigate Ag island formation and island interactions on the surface.

With the efficiency of LatAKMC and the use of the basin method, a growth simulation can be initiated with a single deposition event rather than using a seed or initial high concentrations of Ag on the ZnO surface. This means that all cluster formation is produced directly from

the model, although, as with the previous growth simulations, the deposition rate is kept at 12 ml/s and the system temperature used to calculate the rates of transition events is 300 K. Periodic boundaries are implemented in the x and z directions with growth occurring in the y direction.

7.3.1 100 Atom Surface

First, a small, perfectly crystalline surface of 100 O atoms was investigated using the LatAKMC simulation method. The results of initial growth agree with the off-lattice AKMC simulation results with small clusters forming once a high concentration of Ag has been deposited on the surface. These clusters then link up via single atom strings on the surface to create one large cluster. Initially, single Ag atoms that deposit above existing Ag clusters will drop down to join the first layer of Ag. However, once $> 50\%$ of the surface is covered and Ag clusters join to create one large cluster across periodic boundaries and second layer Ag atoms begin to cluster (Fig. 7.5).

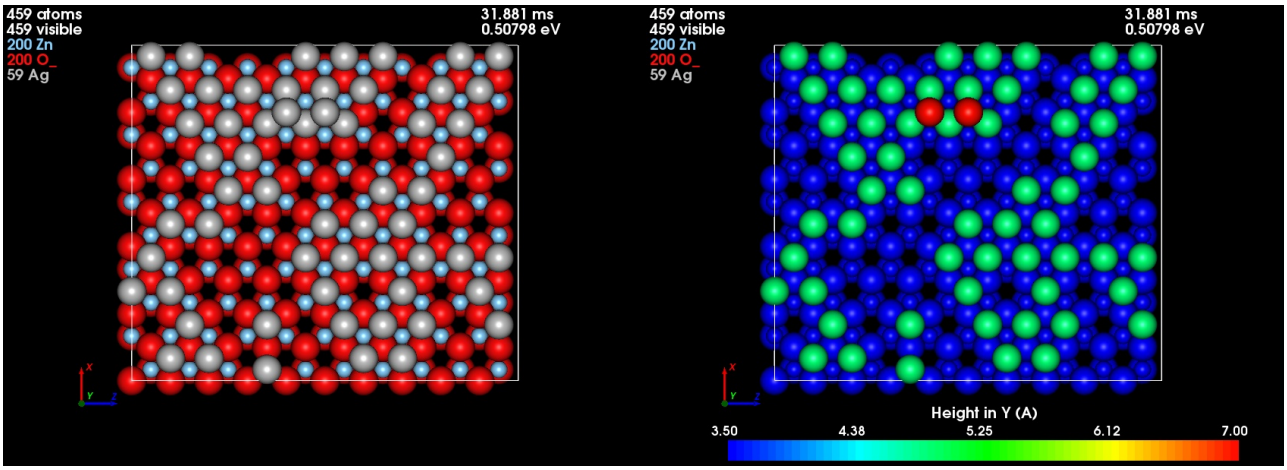

Figure 7.5 – Two images of the same system. The left is coloured by elemental species (red is oxygen, blue is zinc and grey is silver). The right is coloured by height (blue is the ZnO substrate, green are first layer Ag atoms and red are second layer Ag atoms). These structures represent results from a LatAKMC simulation of Ag growth on a ZnO surface containing 100 O atoms. After 31 ms of simulation time and 59 Ag atoms are deposited, the first layer of Ag growth is almost complete whilst a large group of second layer atoms have formed.

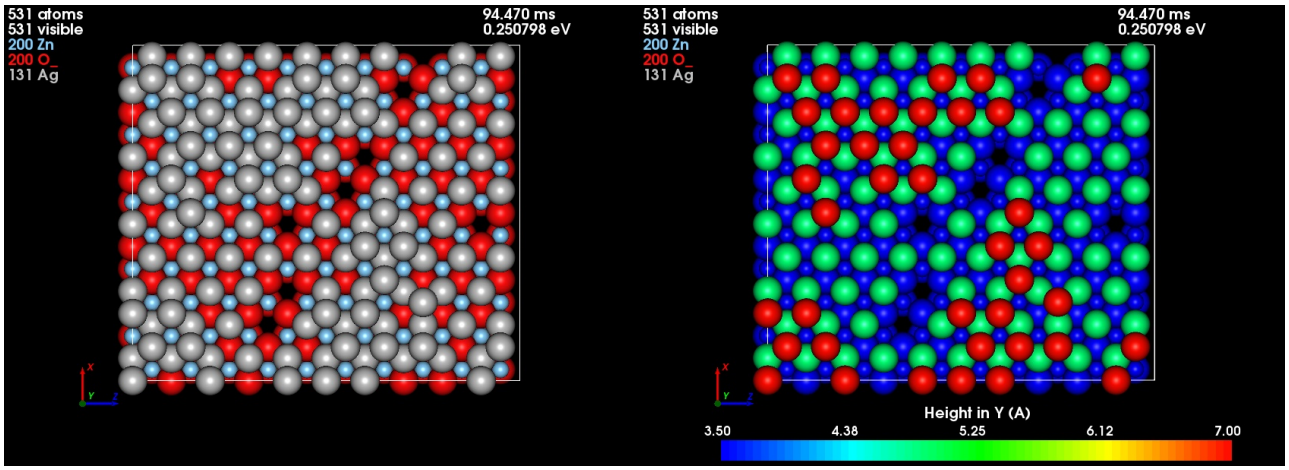

Figure 7.6 – Two images of the same system. The left is coloured by elemental species. The right is coloured by height. After 94 ms of simulation time and 131 Ag atoms are deposited and a second layer of Ag begins to form.

As the simulation time increases, further depositions occur and the second layer clusters increase in size. Some Ag atoms drop down to join the first layer and some deposited atoms fill in gaps in the first layer. However, after 95 ms, around 40% of the second layer is covered in Ag atoms whilst the first layer is not fully complete (93% coverage) - see Fig. 7.6. Once large second layer clusters of Ag form, the probability of atoms dropping down to join the first layer becomes small. Gaps in the first layer of growth only then fill by random depositions and not by diffusion mechanisms. This agrees with island growth results that were predicted using critical island analysis and results from experiments [22].

7.3.2 432 Atom Surface

As with the 100 atom surface case, growth is considered on larger surfaces containing 432 surface O atoms. The initial growth results replicate results seen for the smaller surface case. First, small clusters of Ag form on the surface. These clusters expand and join together to form a single cluster whilst leaving sections of the ZnO surface uncovered. Some atoms deposit onto the ZnO surface and eventually attach to existing clusters whilst other atoms deposit above the first layer Ag atoms (Fig. 7.7) and step off to join the first layer of Ag.

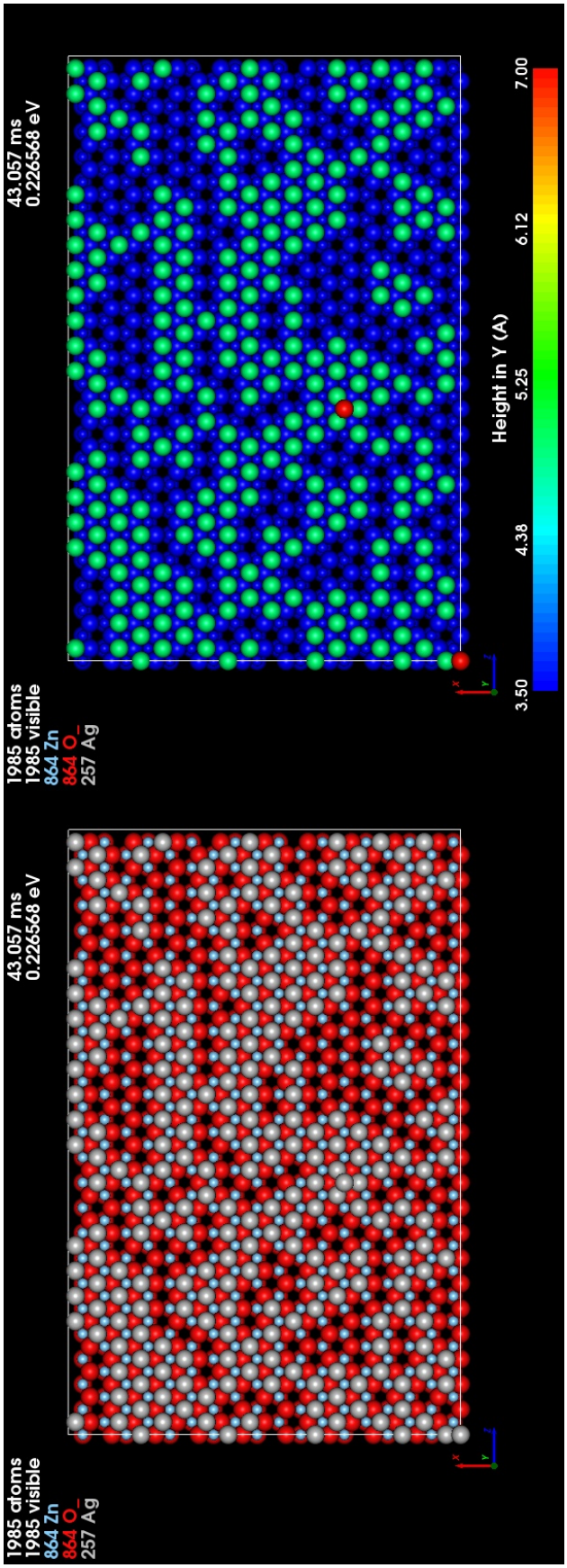

Figure 7.7 – Two images of the same system. The left is coloured by elemental species. The right is coloured by height. After 43 ms of simulation time and 257 Ag atoms are deposited, two Ag atoms are above the first layer of Ag.

After significant deposition of Ag (> 50% coverage of the initial surface), second layer Ag atoms start to form clusters which prevent them from joining the first layer. Two growth simulation are shown after second layer growth has occurred in Fig. 7.8 and Fig. 7.10. These simulations are then continued for a further 10 ms and growth developments are shown in Fig. 7.9 and Fig. 7.11. The two simulations present similar results after 50 ms of simulated growth. At this stage of growth, some deposited Ag atoms still join the first layer of Ag unless they are deposited on the second layer and have clear diffusion pathways towards existing second layer clusters. The first simulation (Fig. 7.8) shows 3 main clusters forming on the second layer of Ag whilst the second simulation (Fig. 7.10) shows one main cluster forming, other than a single dimer and trimer. However, the number of atoms deposited compared to the number of atoms in the second layer of Ag are similar in both simulations. Coverage of the surface is also comparable with 62.5% and 68.5% of the ZnO surface covered with Ag respectively after 50 ms.

After an additional 10 ms (total simulation time > 60 ms), initial clusters that form on the second Ag layer grow in size (Fig. 7.9 and Fig. 7.11). In this time, between 45 and 60 new Ag atoms deposit and a large proportion adsorb above the first layer of Ag. The two example simulations suggest that after 60 ms of simulation time, between 70 and 75% of the ZnO surface is covered (increasing an additional 7-8% from 50 ms simulations). However, large parts of the ZnO surface are left uncovered as large and stable second layer clusters form.

Growth simulations on the larger surface agree well with simulations on the smaller surface. It is clear that for initial growth, Ag will not grow in smooth layers but rather grow in islands. In agreement with the critical island size analysis, second layer clusters start to form once the majority of the ZnO surface is covered.

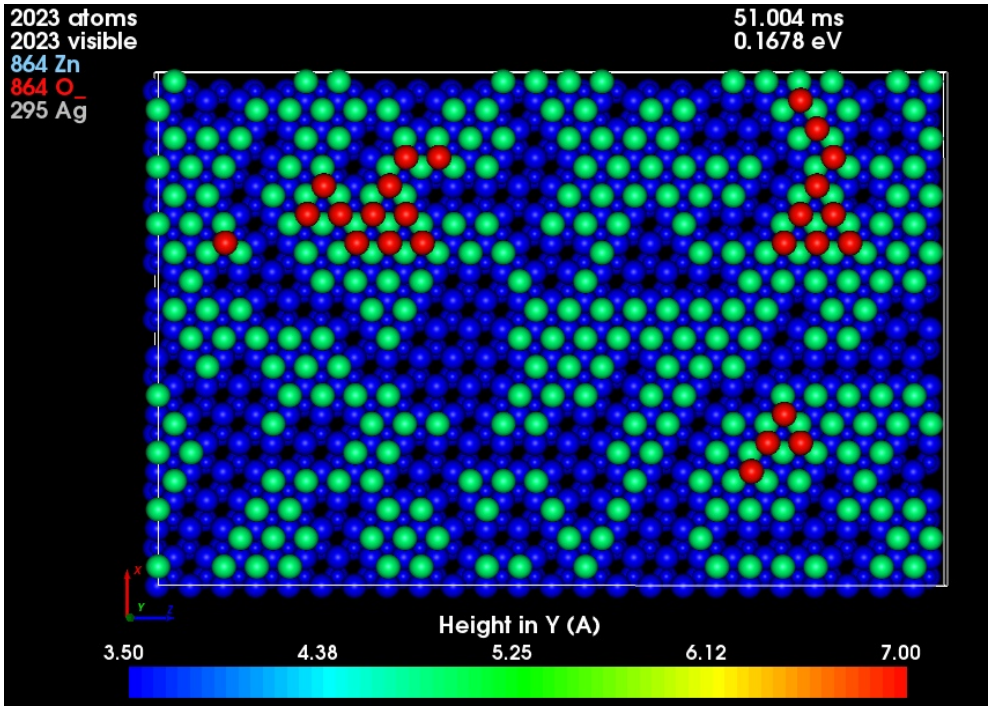

Figure 7.8 – An example growth simulation after 51 ms of simulation time and 295 Ag atoms are deposited; 25 Ag atoms are above the first layer of Ag in 3 main clusters. Atoms are coloured by height. Blue spheres depict ZnO atoms (small spheres are Zn and large spheres are O); green spheres indicate first layer Ag and red spheres indicate second layer Ag.

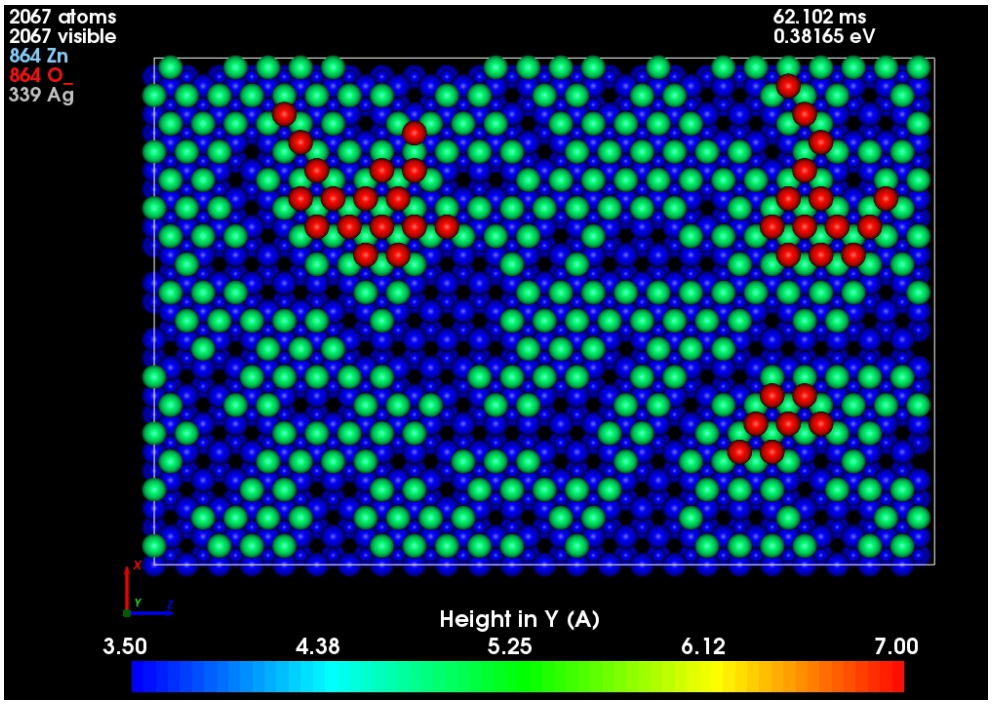

Figure 7.9 – The example growth simulation in Fig. 7.8 after 62 ms of simulation time and 339 Ag atoms are deposited; 38 Ag atoms are above the first layer of Ag in 3 main clusters.

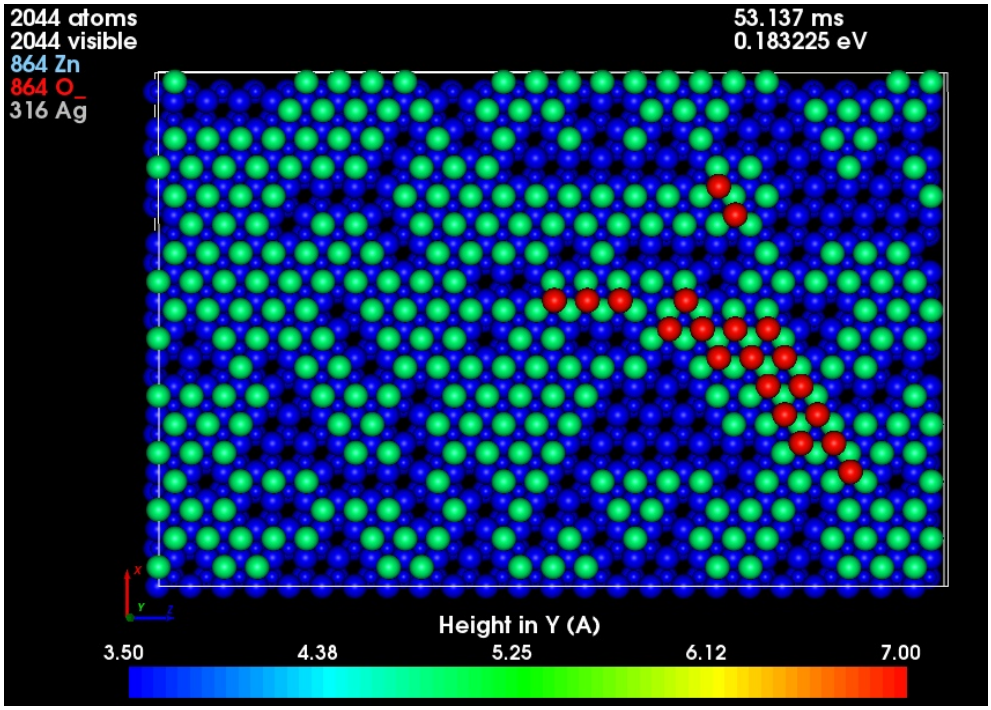

Figure 7.10 – An example growth simulation after 53 ms of simulation time and 316 Ag atoms are deposited; 20 Ag atoms are above the first layer of Ag in one main cluster. Atoms are coloured by height. Blue spheres depict ZnO atoms (small spheres are Zn and large spheres are O); green spheres indicate first layer Ag and red spheres indicate second layer Ag.

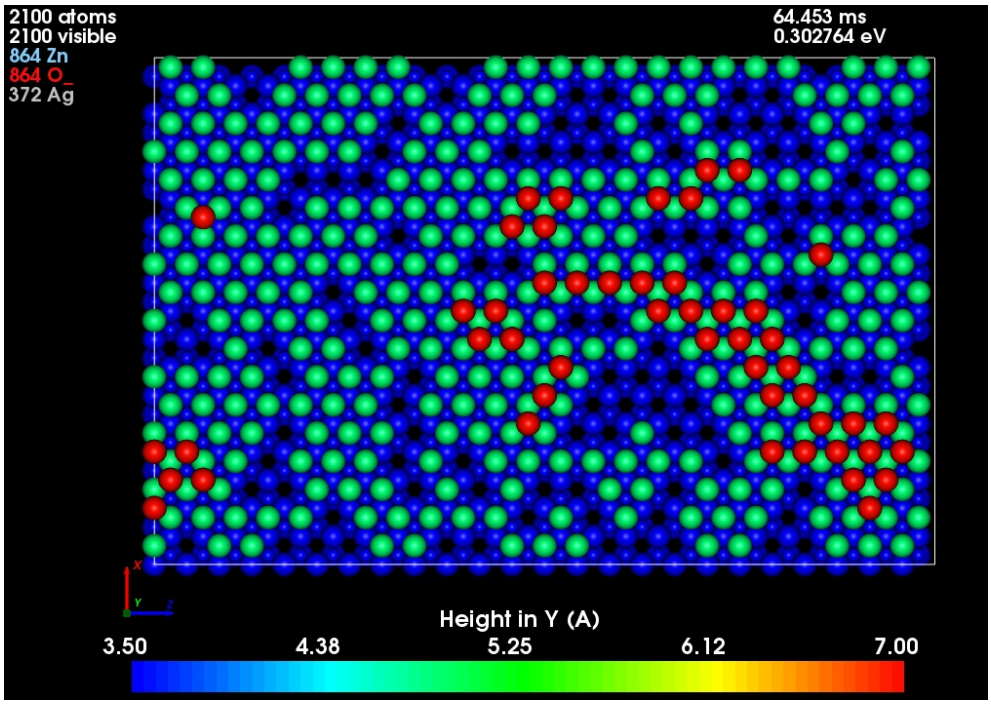

Figure 7.11 – The example growth simulation in Fig. 7.10 after 65 ms of simulation time and 372 Ag atoms are deposited; 49 Ag atoms are above the first layer of Ag with one main cluster.

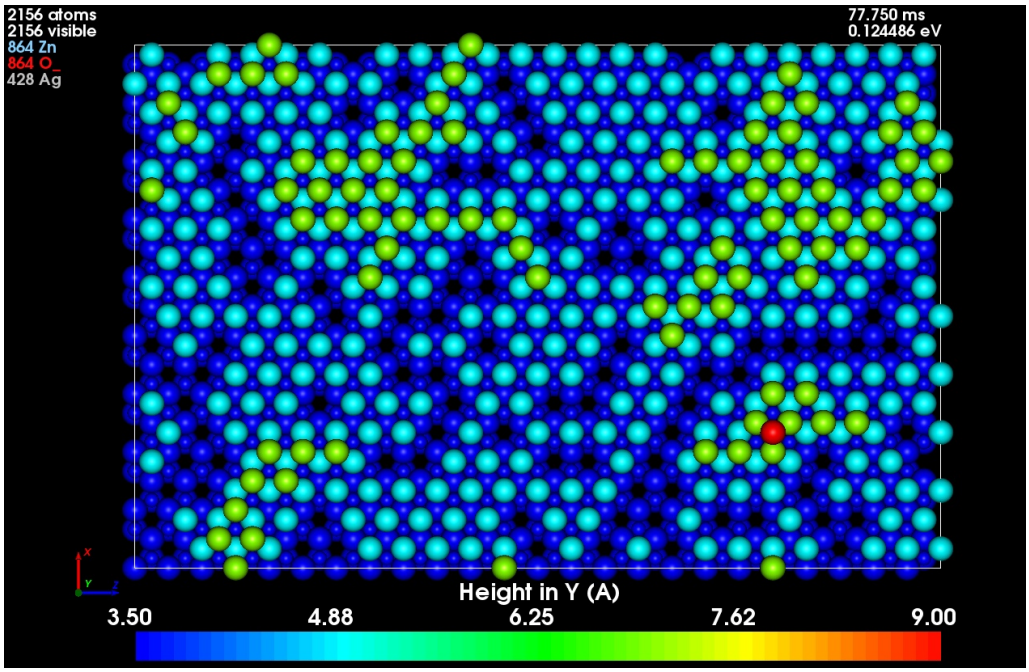

Figure 7.12 – The example growth simulation in Fig. 7.8 after 77 ms of simulation time and 428 Ag atoms are deposited; 87 Ag atoms are in the second layer of Ag with a single Ag atom in the third layer. Here dark blue spheres depict the ZnO substrate (small spheres are Zn and large spheres are O), light blue spheres are the first layer Ag atoms, green spheres second layer Ag atoms and the red sphere is a third layer Ag atom.

Further growth can be seen in Fig. 7.12. After 77 ms of growth, 428 Ag ad-atoms have deposited resulting in the ZnO substrate with 78% coverage. Here, the three main clusters seen earlier in the simulation have grown in size with the addition of some small clusters forming in other areas of the surface. At this stage of growth, a single Ag ad-atom has deposited above second layer Ag atoms. From the critical island analysis, this Ag is not expected to join the second layer through diffusion events. As with all the example simulations, Ag atoms predominately reside in an ABcb stacked configuration. During the LatAKMC growth simulation in Fig. 7.12, diffusion of clusters resulting in the changing of stacking order from ABca to the favourable ABcb stacked configuration occur.

Throughout lattice AKMC simulations, Ag atoms predominately reside in favourable ABc (for first layer growth) or ABcb (for second layer growth) stacking configurations. However, occasionally ad-atoms sit in unfavourable stacking sites and small clusters of them can form.

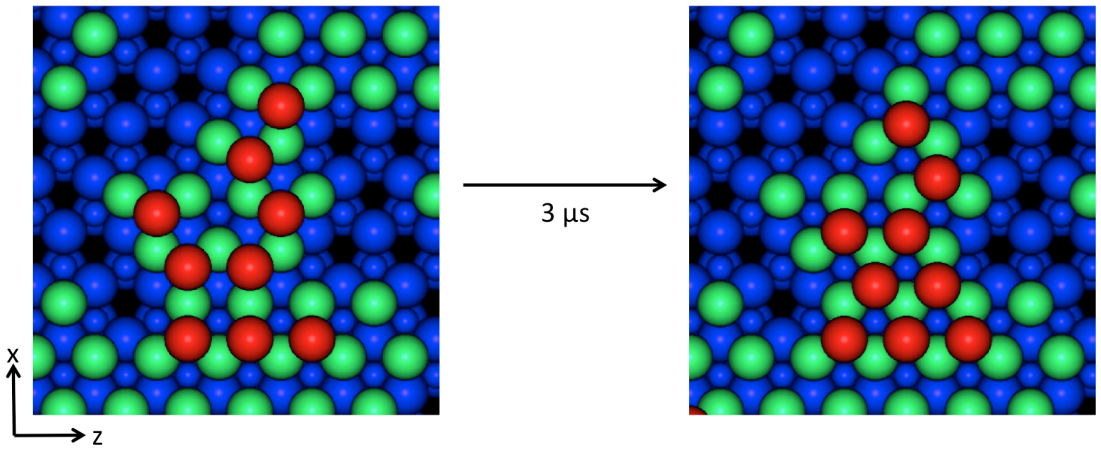

Figure 7.13 – Example of 6 second layer Ag atoms shifting from ABca to ABcb stacking sites during a simulation. The total process takes around 3 μs to complete - equivalent to a single transition barrier of 0.45 eV.

Despite the limitations of the current methodology only allowing single atoms moves, stacking of ad-atoms clusters can change within short frames during a LatAKMC simulation. During a LatAKMC simulation, a group of 6 attached Ag ad-atoms undergo single atom transitions that result in a favourably stacked cluster (see Fig. 7.13) - a combination of transitions that take 3 μs to complete once the first transition is chosen. This timescale is equivalent to a single transition barrier of 0.45 eV.

7.3.3 Island growth mechanisms

By considering all possible adsorption sites on an existing Ag island on the ZnO surface as a single superbasin, island growth mechanisms are explored. The probability of an ad-atom being located at any single site in the basin before escaping and joining the layer below, i.e. growing in the surface plane direction, is calculated by normalising the mean residence time in each site with respect to the total residence time within the basin. When considering symmetric (hexagonal) islands, results suggest that for more than 98% of the time in the island basin, the Ag is situated directly above an O atom. Preferable sites are also located towards the edges of the island with the most favourable sites located at the corner and above O atoms (see Fig. 7.14).

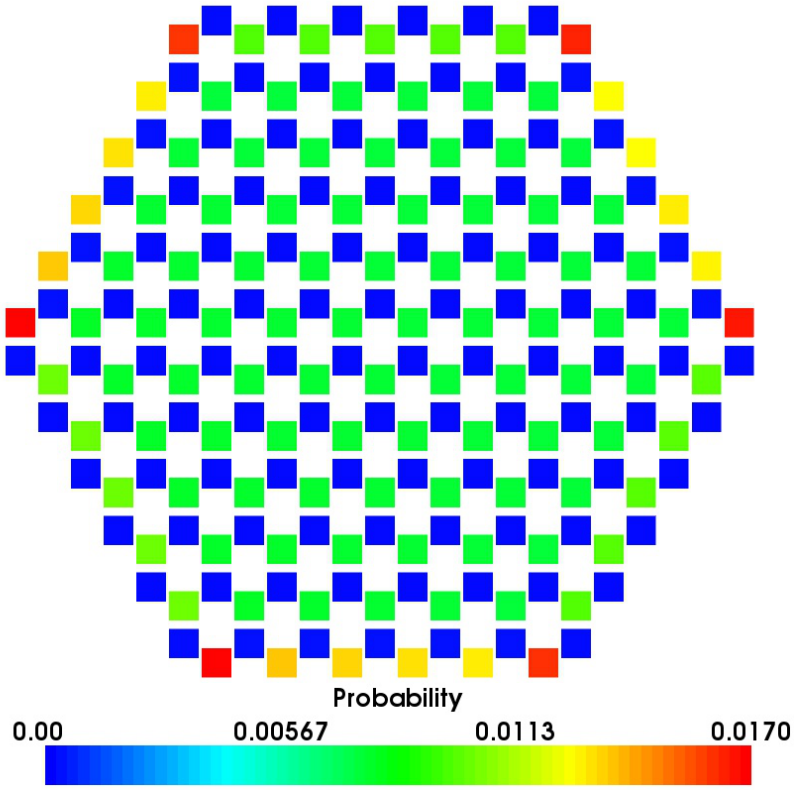

Figure 7.14 – Probability heat map of a single Ag ad-atom being in each site above a hexagonal island before dropping off and joining the layer below. The island consists of 127 Ag atoms on a perfect ZnO $(000\bar{1})$ surface in a favourable ABc stacked configuration. Each square denotes a lattice site considered within the island superbasin. Blue sites correspond to adsorption sites directly above surface Zn atoms whilst the favourable green, yellow and red sites are directly above surface O atoms.

The probability for atoms to drop off the island in certain directions are considered. The rates for Ag atoms to escape the island superbasin when situated above Zn and O edges sites are 1.32×10^7 and 8.02 times per second respectively. By combining these rates with the residence probabilities shown in Fig. 7.14, it suggests that Ag atoms are $\approx 10^4$ times more likely to escape the island basin in directions that have adsorption sites directly above Zn surface atoms at the edges. This implies that Ag islands would not grow in regular hexagonal or circular shapes but rather in long chains seen in theLatAKMC growth simulations (Fig. 7.7).

7.4 Conclusions

The lattice based AKMC method increases the efficiency of the simulation of Ag growth on ZnO surfaces and allows larger systems to be considered. Initial growth results for LatAKMC agree with off-lattice AKMC results using the ReaxFF potential. At first, Ag forms small clusters and leave gaps in the first layer of Ag growth before the second layer begins to form. Using the basin method, transitions where Ag atoms drop down a layer are commonly seen for the first 50 ms of growth. This method is over 2 orders of magnitude more efficient than the off-lattice model. On a single processor, the LatAKMC model can perform 100,000's of steps (for a 100 atom ZnO surface) in a few days making it an extremely useful tool for systems that can be modelled by a lattice based method.

LatAKMC is efficient at simulating growth of Ag on ZnO but is not without its flaws. For simplicity, the method currently only considers single atom moves and low energy deposition events that result in no surface deformation. However, small clusters are shown to be an important growth mechanism for producing defect boundaries for Ag on Ag growth as well as higher deposition energies for producing smoother surfaces [21]. The results in this chapter show that crystalline and coherent Ag/ZnO interfaces are likely to be seen without twin or phase boundaries occurring during initial growth. The introduction of small cluster moves and an implementation of higher energy deposition events are key features to further the methodology.

The speed of the method itself could be improved further with the implementation of parallelisation and improved efficiency within search methods. An ability to gather transitions from a large list of atoms in parallel would be something that could be simply implemented as well as running NEB search methods. Other ways to parallelise the code could be by splitting the system into regions and performing simulations on each region separately whilst neighbouring regions communicated atom positions near each of the boundaries.

Chapter 8

Conclusions and Future Work

8.1 Conclusions

The main aim of this project was to investigate Low-E window coatings at the atomistic scale. The Ag/ZnO interface was the main focus due to its importance in creating a good Low-E product. As such, the dynamics of initial growth processes of Ag on ZnO surfaces was investigated. This research has considered a range of different timescale techniques to simulate initial Ag growth at various stages. Simulation techniques used include Molecular Dynamics (MD) for deposition modelling, Density Functional Theory (DFT) to assist in the development of a new potential, adaptive KMC (AKMC) to simulate initial diffusion of Ag atoms on ZnO surfaces and lattice based AKMC (LatAKMC) to extend Ag growth simulations to longer time and length scales. Initial growth processes were simulated using two different sets of potential functions.

For MD and AKMC simulations, the potential function considered is key for accurate simulation results. A potential function is fitted with certain properties in mind. It is important that the potential function reproduces the key properties for that system well. It is seen that a simplified potential (fitted to surface works of separation) does not accurately reproduce all

surface interactions. The Morse and ZBL potentials used by Gheewala [28] were explored for initial Ag thin film growth on ZnO. Results from this investigation imply that a mixed Ag-ZnO interface would be present using low energy deposition methods as Ag atom can penetrate the ZnO surface during both deposition and diffusion events. However, the simplified model overestimated the stability of Ag interstitials in the ZnO substrate when compared to DFT calculations.

Due to the importance of having an accurate potential function for a given system, a new ReaxFF potential was developed for Ag and ZnO surface interactions. This potential accurately reproduces DFT and experimental properties including the energy for Ag interstitials in the ZnO substrate. With the new potential, single point depositions and growth simulations were conducted.

During further AKMC simulations, two methods of defining defect volumes within a system were considered. One relies on comparing the current system to a reference lattice whilst the other relies on coordination numbers of each atom in the current state. The second method is shown to help produce more successful transition searches. This means that more diffusion events were seen within a simulation than an AKMC simulation using the first method. Because of this, less Ag atoms deposit and thus less Ag is grown on the ZnO surfaces after the same number of KMC steps. The consequence of finding more transitions is that the simulations do not reach full multilayer growth in a computationally feasible number of simulation steps.

In an attempt to increase the time and length scales seen in the off-lattice AKMC simulations, an on-lattice method was created. Using a lattice based model, a large number of transitions are guaranteed to be included but the computational resources needed to conduct a single KMC step is far less than for off-lattice models. One advantage of on-lattice models is the ability to reuse transitions that have been found earlier in the simulation or from previous simulations

occurs more often. The results from latAKMC suggest that Ag does in fact grow in islands on a perfect ZnO surface.

A common problem that plagues AKMC simulations is that of low energy barrier transitions dominating whilst no net diffusion occurs. This is a persistent problem seen within our AKMC simulations. Once a single Ag atom deposits above existing Ag atoms, the transition barrier heights become small and thus these transitions dominate the simulation. A solution to this problem can be implemented with the use of "super-basin'" methods. Yu [24] explores the advantages of using a basin method when considering surface growth of CdTe .

However, results of the basin method implementation are only given for the on-lattice AKMC model in this work. This method accelerates a simulation through low energy barrier basins and allows us to simulate multilayer Ag growth. With further advances in computational power and advances in acceleration methods, many layers of Ag growth could be accurately simulated.

This work explores various causes of defective thin film growth. Large surface defects are shown to affect the initial growth phases by either attracting Ag ad-atoms or effectively repelling them. However, even perfect ZnO surfaces are shown to produce incomplete initial Ag layers. This work also explores ideal deposition energies for Ag on the ZnO surface. It is shown that low energy deposition (< 10 eV) results in minimal Ag penetration and reflection but maximum adsorption.

One of the main aims was to suggest methods to improve the quality of the Ag thin film grown on ZnO from the simulation results. A practical production method for optimal Ag growth on ZnO may include a two stage deposition technique. Initial growth could be conducted using low deposition energies (< 10 eV) to avoid Ag mixing with the ZnO and help produce a sharp interface. A second stage in the thin film application process, once initial layers of Ag have

grown, could see higher deposition energies being used (30-40 eV) to encourage Ag diffusion and smoother layers being produced. In previous work by Blackwell [21], smoother Ag thin films were grown on Ag substrates when higher deposition energies were considered.

8.2 Future work

Although the project has considered the growth of Ag on ZnO using a number of different atomistic techniques, there are inevitably many aspects of the work that could form the basis of further investigation, both in terms of methodology and application.

8.2.1 Methodology

The off-lattice AKMC approach is a research tool that is in a state of continuous development. There are a number of different areas for improvement and where the methodology could be made more robust. During the course of the work a different way of identifying defects was implemented which gave rise to a more complete set of potential transitions compared to previous work, such as that carried out by Blackwell [21]. Although this was an improvement in the methodology it also meant that the simulations were more time consuming. It is still not completely clear what constitutes a good set of transitions and when transition searches should be terminated. A theoretical study of this problem would make the methodology more robust.

A related issue is that of using the most efficient method to search for saddle points that surround a local minimum in n-dimensional space. It should ideally be one that does not use the Hessian matrix since that is expensive to compute. The currently implemented search algorithms, which are the RAT, ART, Dimer and Dimer plus Lanczos [73] methods sometimes fail to find a transition. A theoretical understanding of why these transition searches fail and how to control the step size in the numerical search process for a given accuracy in the transition

barrier height would also be of benefit.

When transition search methods fail to converge to a saddle point, it does not mean that a saddle does not exist in that direction. If this is the case, the assumption that all transitions are found within a AKMC simulation is not true. This influences the time step used to advance the system and the legitimacy of any results obtained by these methods. Poor convergence can be caused by noisy energy landscapes due to complicated potential functions or non-optimal parameters within the search method itself. The use of new adaptive search methods that adjust step sizes/convergence criteria on-the-fly or the combination of multiple saddle search methods could reduce the probability of missing possible transitions.

The basin method was implemented in the LatAKMC code but requires more work to be done to be fully implemented into the off-lattice AKMC code. In addition it is not clear what is the correct statistical distribution of barriers that arises from the basin method and which should be used for the mean rate calculations.

Other improvements to the AKMC code include a better methodology for reusing previously found transitions and spatial decomposition for parallelisation.

The LatAKMC method was newly developed and, because of this, it is not without its flaws. The strict lattice based model means that atoms are forced onto lattice sites that may be far away from their local minimum causing large movements during aggressive minimisation techniques used to calculate transition barrier heights. In addition, only single atoms are allowed to move during all transitions in the current method and so small cluster diffusions are not all accounted for. Key improvements to the lattice based AKMC method would include the introduction of small cluster transitions in the x-z plane, the ability to model defective surfaces and parallelisation of the search methods. The inclusion of small cluster transitions would

better predict initial growth mechanisms and the formation of defect boundaries. The ability to model defective surfaces could accelerate growth simulations when imperfect surfaces are considered (O-deficient surfaces). By including a parallelisation to the code, efficiency would increase and larger systems could be simulated.

Other long timescale simulation techniques could be used as a comparison to AKMC simulation results. Accelerated MD methods that efficiently run in parallel, such as parallel trajectory splicing [74] or speculatively parallel TAD [75], may help shed further light on diffusion of Ag on existing Ag islands and the affect of surface defects on Ag growth. These methods cannot yet reach the timescales produced from AKMC techniques but can obtain accurate transition rates without approximating the escape frequency via the Arrhenius equation and eliminate the need for numerical search algorithms.

8.2.2 Applications

The model so far has only investigated the initial stages of growth of Ag on ZnO at a deposition energy of 3 eV in the case of the AKMC model. To optimise the film growth, a range of deposition energies should be considered. This could also include an approach whereby the first few layers of Ag are grown at a low energy to avoid penetration into the ZnO followed by a higher energy to improve the film smoothness and therefore prevent island growth. Annealing at various temperatures could also be investigated.

In addition, other sputter techniques could be compared such as high-power impulse magnetron sputtering (HIPIMS) or pulsed magnetron sputtering rather than the continuous deposition process, which has been the focus of the work here. Growth on surfaces with a wider range of intrinsic defects could also be investigated.

The technique can also be applied to many other complex coatings where reactive magnetron sputtering is used. If suitable potential functions do not exist for the particular systems under study the reactive potential formalism, together with *ab initio* methods, can be used in the same way as described here. For window glass, such systems might include TiO_2, pure Ti or other reflective materials such as Al and Au.

Besides thin film growth, there are many other applications of the methodology. The long time evolution of defects is an issue in nuclear energy applications both in structural components of a reactor and also when the nuclear waste has been encapsulated. Since such encapsulation is over time scales that cannot be accessed experimentally, the methodology has potential to be of considerable use for these problems. Since encapsulation materials are often materials with short range order such as glasses, this would open up a new field of study.

Other applications of AKMC methods include modelling protein folding to help prevent incorrect folding - an occurrence that can cause allergies, discovering optimum zeolite structures for molecular sieves or catalysts and understanding growth processes of carbon nanotubes [76]. All together, the variety of applications for the methodology is huge and could be used within a large number of scientific fields and industries including nuclear and biomedical. With the addition of further acceleration techniques, the span of potential applications could only increase.

Bibliography

[1] R. E. Hummel, K. H. Guenther, Handbook of optical properties: thin films for optical coatings, Vol. 1, CRC Press, 1995.

[2] H. Glaser, History of the development and industrial production of low thermal emissivity coatings for high heat insulating glass units, Appl. Opt. 47 (13) (2008) c193–c199.

[3] C. Kittel, Introduction to Solid State Physics, 8th Edition, Wiley, 2004.

[4] Z. Lin, P. D. Bristowe, Microsopic characteristics of Ag(111)/ZnO(0001) interface present in optical coatings, Phys. Rev. B 75 (2007) 205423.

[5] Z. Wang, Zinc oxide nanostructures: growth, properties and applications, J. Phys. Condens. Matter 16 (2004) R829–R858.

[6] Structure types [cited October 2016].
URL `https://en.wikipedia.org/wiki/User:Benjah-bmm27/Structure_types`

[7] Z. Lin, P. D. Bristowe, A first principles study of the properties of Al: ZnO and its adhesion to Ag in an optical coating, J. Appl. Phys. 106 (1) (2009) 013520.

[8] K. K. Schuegraf, Handbook of thin-film deposition processes and techniques: principles, methods, equipment, and applications, Noyes Data Corporation/Noyes Publications, 1988.

[9] P. Kelly, R. Arnell, Magnetron sputtering: a review of recent developments and applications, Vacuum 56 (3) (2000) 159–172.

[10] N. Marechal, E. Quesnel, Y. Pauleau, Silver thin films deposited by magnetron sputtering, Thin Solid Films 241 (1-2) (1994) 34–38.

[11] R. A. Friesner, Ab initio quantum chemistry: methodology and applications, Proc. Natl. Acad. Sci. U.S.A. 102 (19) (2005) 6648–6653.

[12] A. Lloyd, D. Cornil, A. van Duin, D. van Duin, R. Smith, S. D. Kenny, J. Cornil, D. Beljonne, Development of a ReaxFF potential for Ag/Zn/O and application to Ag deposition on ZnO, Surf. Sci. 645 (2016) 67–73.

[13] M. Yu, S. D. Kenny, Using atomistic simulations to model cadmium telluride thin film growth, J. Phys. Condens. Matter 28 (10) (2016) 105002.

[14] T. Lazauskas, S. D. Kenny, R. Smith, G. Nagra, M. Dholakia, M. Valsakumar, Simulating radiation damage in a BCC Fe system with embedded yttria nanoparticles, Journal of Nuclear Materials 437 (1) (2013) 317–325.

[15] S. Blackwell, R. Smith, S. D. Kenny, J. Walls, Modeling evaporation, ion-beam assist, and magnetron sputtering of thin metal films over realistic time scales, Phys. Rev. B 86 (3) (2012) 035416.

[16] S. C. Glotzer, W. Paul, Molecular and mesoscale simulation methods for polymer materials, Annu. Rev. Mater. Res. 32 (1) (2002) 401–436.

[17] M. R. So, A. F. Voter, Temperature-accelerated dynamics for simulation of infrequent events, J. Chem. Phys. 112 (21) (2000) 9599–9606.

[18] A. F. Voter, Parallel replica method for dynamics of infrequent events, Phys. Rev. B 57 (22) (1998) R13985.

[19] A. Chatterjee, D. G. Vlachos, An overview of spatial microscopic and accelerated kinetic monte carlo methods, J. Comput. Aided Mat. Des. 14 (2) (2007) 253–308.

[20] G. Henkelman, H. Jónsson, Long time scale kinetic monte carlo simulations without lattice approximation and predefined event table, J. Chem. Phys. 115 (21) (2001) 9657–9666.

[21] S. Blackwell, Modelling thin film growth over realistic time scales, Ph.D. thesis, © Sabrina Blackwell (2012).

[22] E. Duriau, S. Agouram, C. Morhain, T. Seldrum, R. Sporken, J. Dumont, Growth of Ag thin films on ZnO (000-1) investigated by AES and STM, Appl. Surf. Sci 253 (2) (2006) 549–554.

[23] S. Blackwell, R. Smith, S. Kenny, J. Walls, C. Sanz-Navarro, Modelling the growth of ZnO thin films by PVD methods and the effects of post-annealing, J. Phys. Condens 25 (13) (2013) 135002.

[24] M. Yu, Modelling CdTe thin film growth over realistic time scales, Ph.D. thesis, © Miao Yu (2015).

[25] R. Smith, M. Jakas, D. Ashworth, B. Oven, M. Bowyer, I. Chakarov, R. Webb, Atomic and ion collisions in solids and at surfaces: Theory, Simulation and Applications, Cambridge University, Cambridge, UK.

[26] L. Verlet, Computer "experiments" on classical fluids. I. Thermodynamical properties of Lennard-Jones molecules, Phys. Rev. 159 (1967) 98–103.

[27] P. M. Morse, Diatomic molecules according to the wave mechanics. II. vibrational levels, Phys. Rev. 34 (1) (1929) 57.

[28] I. Gheewala, S. Kenny, R. Smith, Atomistic-scale modelling of nano indentation into optical coatings, Philos. Mag. 89 (34-36) (2009) 3499–3510.

[29] J. Ziegler, J. Biersack, U. Littmark, The stopping power and range of ions in solids, Pergamon Press, New York 4 (1985) 40–47.

[30] G. Ackland, G. Tichy, V. Vitek, M. Finnis, Simple n-body potentials for the noble metals and nickel, Philos. Mag. A 56 (6) (1987) 735–756.

[31] A. van Duin, S. Dasgupta, F. Lorant, W.A. Goddard III, ReaxFF: a reactive force field for hydrocarbons, J. Phys. Chem. A, 105 (41) (2001) 9396–9409.

[32] W. Mortier, S. Ghosh, S. Shankar, Electronegativity equalization method for the calculation of atomic charges in molecules, J. Am. Chem. Soc. 108 (1986) 4315–4320.

[33] D. Raymand, A. C. van Duin, D. Spångberg, W. A. Goddard, K. Hermansson, Water adsorption on stepped ZnO surfaces from md simulation, Surf. Sci. 604 (9) (2010) 741–752.

[34] H. Berendsen, J. Postma, W. van Gunsteren, A. DiNola, J. Haak, Molecular dynamics with coupling to an external bath, J. Chem. Phys. 81 (8) (1984) 3684–3690.

[35] W. G. Hoover, Canonical dynamics: equilibrium phase-space distributions, Phys. Rev. A 31 (3) (1985) 1695.

[36] S. Nosé, A molecular dynamics method for simulations in the canonical ensemble, Mol. Phys. 52 (2) (1984) 255–268.

[37] J. Nocedal, S. Wright, Numerical optimization, Springer Science & Business Media, 2006.

[38] W. H. Press, Numerical recipes 3rd edition: The art of scientific computing, Cambridge university press, 2007.

[39] E. Polak, G. Ribiere, Note sur la convergence de méthodes de directions conjuguées, Rev. Fr. Inf. Rech. Oper., série rouge 3 (1) (1969) 35–43.

[40] C. D. J. Scott, Atoman [cited October 2016].
URL `https://github.com/chrisdjscott/Atoman`

[41] E. Weinan, W. Ren, E. Vanden-Eijnden, Simplified and improved string method for computing the minimum energy paths in barrier-crossing events, J. Chem. Phys. 126 (16) (2007) 164103.

[42] G. Henkelman, H. Jónsson, Improved tangent estimate in the nudged elastic band method for finding minimum energy paths and saddle points, J. Chem. Phys. 113 (22) (2000) 9978–9985.

[43] G. Henkelman, H. Jónsson, A dimer method for finding saddle points on high dimensional potential surfaces using only first derivatives, J. Chem. Phys. 111 (15) (1999) 7010–7022.

[44] N. Mousseau, G. Barkema, Traveling through potential energy landscapes of disordered materials: The activation-relaxation technique, Phys. Rev. E 57 (2) (1998) 2419.

[45] L. J. Vernon, Modelling growth of rutile TiO_2, Ph.D. thesis, © Louis J. Vernon (2010).

[46] D. Sheppard, R. Terrell, G. Henkelman, Optimization methods for finding minimum energy paths, J. Chem. Phys. 128 (13) (2008) 134106.

[47] S. Smidstrup, A. Pedersen, K. Stokbro, H. Jónsson, Improved initial guess for minimum energy path calculations, J. Chem. Phys. 140 (21) (2014) 214106.

[48] B. D. McKay, A. Piperno, Practical graph isomorphism, II, J. Symb. Comput. 60 (2014) 94–112.

[49] L. Bai, D. Breen, Calculating center of mass in an unbounded 2D environment, J. Graph. Tools 13 (4) (2008) 53–60.

[50] G. H. Vineyard, Frequency factors and isotope effects in solid state rate processes, J. Phys. Chem. Solids 3 (1-2) (1957) 121–127.

[51] K. A. Fichthorn, W. H. Weinberg, Theoretical foundations of dynamical monte carlo simulations, The Journal of Chemical Physics 95 (2) (1991) 1090–1096.

[52] M. Chugh, M. Ranganathan, Kinetic monte carlo simulations of epitaxial growth of wurtzite GaN (0001), Phys. Status Solidi C 12 (4-5) (2015) 408–412.

[53] G. Hu, G. Orkoulas, P. D. Christofides, Regulation of film thickness, surface roughness and porosity in thin film growth using deposition rate, Chem. Eng. Sci. 64 (17) (2009) 3903–3913.

[54] B. Puchala, M. L. Falk, K. Garikipati, An energy basin finding algorithm for kinetic Monte Carlo acceleration, J. Chem. Phys. 132 (13) (2010) 134104.

[55] D. Raymand, A. van Duin, M. Baudin, K. Hermansson, A reactive force field (ReaxFF) for zinc oxide, Surf. Sci. 602 (2008) 1020–1031.

[56] D. Cornil, "private communication" (October 2015).

[57] J. Soler, E. Artacho, J. Gale, A. García, J. Junquera, P. Ordejón, D. Sánchez-Portal, The SIESTA method for ab initio order-N materials simulation, J. Phys. Condens. Matter 14 (2002) 2745–2779.

[58] A. van Duin, J. Baas, B. van de Graaf, Delft molecular mechanics:a new approach to hydrocarbon force fields, J. Chem. Soc. Faraday Trans. 90 (19) (1994) 2881–2895.

[59] A. van Duin, V. Bryantsev, M. Diallo, W. Goddard, O. Rahaman, D. Doren, D. Raymand, K. Hermansson, Development and validation of a ReaxFF reactive force field for Cu cation/water interactions and copper metal/metal oxide/metal hydroxide condensed phases, J. Phys. Chem. A 114 (35) (2010) 9507–9514.

[60] W. Koch, M. C. Holthausen, A chemist's guide to density functional theory, John Wiley & Sons, 2015.

[61] D. Cornil, T. van Regemorter, D. Beljonne, J. Cornil, Work function shifts of a zinc oxide surface upon deposition of self-assembled monolayers: a theoretical insight, Phys. Chem. Chem. Phys. 16 (2014) 20887–20899.

[62] J. Perdew, K. Burke, M. Ernzerhof, Generalized gradient approximation made simple, Phys. Rev. Lett. 77 (18) (1997) 3865.

[63] N. Troullier, J. Martins, Efficient pseudopotentials for plane-wave calculations, Phys. Rev. B 43 (3) (1993) 1993–2006.

[64] H. Monkhorst, J. Pack, Special points for Brillouin-zone integrations, Phys. Rev. B 13 (12) (1976) 5188–5192.

[65] H. Li, L. K. Schirra, J. Shim, H. Cheun, B. Kippelen, O. L. A. Monti, J. Bredas, Zinc oxide as a model transparent conducting oxide: A theoretical and experimental study of the impact of hydroxylation, vacancies, interstitials, and extrinsic doping on the electronic properties of the polar ZnO (0002) surface, Chem. Mater. 24 (2012) 3044–3055.

[66] R. Fletcher, C. Reeves, Function minimization by conjugate gradients, Comput. J. 7 (1964) 149–154.

[67] W. Pearson, A Handbook of Lattice Spacings and Structures of Metals and Alloys, Pergamon Press, London, 1958.

[68] T. Lin, C. Li, J. Niedziela, H. Smith, D. Abernathy, G. Rossman, B. Fultz, Anharmonic lattice dynamics of Ag_2O studied by inelastic neutron scattering and first principles molecular dynamics simulations, Phys. Rev. B 89 (2014) 054306.

[69] C. Scott, S. Blackwell, L. Vernon, S. Kenny, M. Walls, R. Smith, Atomistic surface erosion and thin film growth modelled over realistic time scales, J. Chem. Phys. 135 (2011) 174706.

[70] J. Tersoff, A. D. van Der Gon, R. Tromp, Critical island size for layer-by-layer growth, Phys. Rev. Lett. 72 (2) (1994) 266.

[71] J. A. Stroscio, D. Pierce, Scaling of diffusion-mediated island growth in iron-on-iron homoepitaxy, Phys. Rev. B 49 (12) (1994) 8522.

[72] S. Parker, A. Grant, V. Bondzie, C. Campbell, Island growth kinetics during the vapor deposition of gold onto TiO_2 (110), Surf. Sci. 441 (1) (1999) 10–20.

[73] C. Lanczos, An iteration method for the solution of the eigenvalue problem of linear differential and integral operators, United States Governm. Press Office Los Angeles, CA, 1950.

[74] D. Perez, E. D. Cubuk, A. Waterland, E. Kaxiras, A. F. Voter, Long-time dynamics through parallel trajectory splicing, J. Chem. Theory Comput. 12 (1) (2015) 18–28.

[75] R. J. Zamora, B. P. Uberuaga, D. Perez, A. F. Voter, The modern temperature-accelerated dynamics approach, Annu. Rev. Chem. Biomol. Eng 7 (2016) 87–110.

[76] A. Maiti, C. Brabec, C. Roland, J. Bernholc, Theory of carbon nanotube growth, Phys. Rev. B 52 (20) (1995) 14850.